中国科学技术大学

博士学位论文

BESIII 上质子形状因子与重子对产生截面的测量

作者姓名： 周 小 蓉

学科专业： 粒子物理与核物理

导师姓名： 赵政国 教授

黄光顺 教授

完成时间： 二〇一五年五月

University of Science and Technology of China

A dissertation for doctor degree

Measurement of proton form factor and baryon pairs production in e^+e^- annihilation at BESIII

Author : Xiaorong Zhou

Speciality : Particle and Nuclear Physics

Supervisor : Prof. Zhengguo Zhao

Prof. Guangshun Huang

Finished Time : May, 2015

BESIII上质子形状因子与重子对产生截面的测量

四系

周小蓉

中国科学技术大学

中国科学技术大学学位论文原创性声明

本人声明所呈交的学位论文，是本人在导师指导下进行研究工作所取得的成果。除已特别加以标注和致谢的地方外，论文中不包含任何他人已经发表或撰写过的研究成果。与我一同工作的同志对本研究所做的贡献均已在论文中作了明确的说明。

作者签名：____________　　　　签字日期：____________

中国科学技术大学学位论文授权使用声明

作为申请学位的条件之一，学位论文著作权拥有者授权中国科学技术大学拥有学位论文的部分使用权，即：学校有权按有关规定向国家有关部门或机构送交论文的复印件和电子版，允许论文被查阅和借阅，可以将学位论文编入《中国学位论文全文数据库》等有关数据库进行检索，可以采用影印、缩印或扫描等复制手段保存、汇编学位论文。本人提交的电子文档的内容和纸质论文的内容相一致。

保密的学位论文在解密后也遵守此规定。

□公开　□保密 ________ 年

作者签名：____________　　　　导师签名：____________

签字日期：____________　　　　签字日期：____________

摘　要

核子作为物质的基本组成单元，其内部结构的研究是粒子物理的重要课题之一。理论上，点状质子和中子的磁矩分别为一个核磁子（μ_N）和 0。实验上测量的核子具有反常磁矩，$\mu_p = 2.79\mu_N, \mu_n = -1.91\mu_N$, 暗示着核子具有内部结构。在电子 -质子弹性散射实验中，测量的散射微分截面与类点粒子散射公式偏离，进一步验证了核子的非点状结构，并由此引入质子形状因子的概念。质子形状因子是包含有量子色动力学（QCD）基本参数的唯象公式，它不仅可以描述质子内部电荷和电流的空间分布，也能够对基于 QCD 的微扰及非微扰理论进行严格的测试。质子形状因子的测量分为类空空间（四动量转移为负）和类时空间（四动量转移为正）测量，实验上对类时空间质子形状因子的测量可以追溯到上个世纪六十年代。虽然已有大量的实验结果，但是人们对质子形状因子随能量的分布仍存在不少疑问，例如分布谱上出现的特殊结构、阈值特殊效应、以及电磁形状因子的比值等。对于中子及其他重子的形状因子，实验结果很少并且精度均不高。因此实验上仍需要对重子的形状因子进行系统化的研究和精确测量。

北京正负电子对撞机（BEPCII）采用双储存环设计，是一台高亮度，多束团的对撞机，工作于 τ - 粲能区（2.0 - 4.6 GeV），在优化质心能量 3770 MeV 下的设计亮度为 $1.0 \times 10^{33}\mathrm{cm}^{-2}\mathrm{s}^{-1}$。北京谱仪（BESIII）是 BEPCII 上唯一的探测器。本文利用 BESIII 在连续能区取得的 14 个能量点的数据，研究了质心能量从 2232.4 MeV 至 3671.0 MeV, 正负电子对湮灭到质子反质子对的过程。质子反质子由 dE/dx 及 TOF 信息进行鉴别，通过对两条径迹的动量及夹角的限制，得到了非常纯净的信号样本，进而得到 $e^+e^- \to p\bar{p}$ 的玻恩截面。结果与之前实验结果相符，并把精度提高近 30%。假设电磁形状因子相等 $|G_E| = |G_M|$,

我们得到类时空间上质子的有效形状因子。此外，我们还利用积分亮度相对高的三个数据样本（$\sqrt{s}$ =2232.4, 2400 MeV 及联合数据样本 3050.0，3060.0 和 3080.0 MeV），通过拟合质子在质心系中的角分布，测量了电磁形状因子之比 ($|G_E/G_M|$)，测量结果均接近于 1，误差主要由统计量限制，在 25% 至 50% 之间。实验结果说明在误差范围内，电磁形状因子相等的假设在能区 2.2 - 3.0 GeV 内可以认为成立。并且通过模拟研究发现，如果能够提高统计量，$|G_E/G_M|$ 的精度将会显著提高。

除了测量质子的形状因子，我们还研究了正负电子对湮灭到 $\Lambda\overline{\Lambda}$ 的过程，并由此测量其近阈产生截面及 Λ 的有效形状因子。利用 BESIII 在高于 $\Lambda\overline{\Lambda}$ 产生阈 1 MeV（$\sqrt{s} = 2232.4$ MeV）取得的数据，我们测量了 $e^+e^- \to \Lambda\overline{\Lambda}$ 的玻恩截面。实验从两个方面进行重建 $\Lambda\overline{\Lambda}$，*i)* 重建 $\Lambda/\overline{\Lambda}$ 带电衰变（$\Lambda/\overline{\Lambda} \to p\pi^-/\bar{p}\pi^+$），由于末态粒子动量很小，pion 粒子在 MDC 内打圈，而质子反质子径迹不能够在 MDC 中重建，我们利用反质子与束流管作用出次级粒子的特性来重建信号；*ii)* 重建 $\overline{\Lambda}$ 中性衰变（$\overline{\Lambda} \to \bar{n}\pi^0$），利用反中子在 EMC 中信息，通过多变量分析研究信号与本底的区别，由于 $\overline{\Lambda}$ 几乎静止，我们最终通过拟合中性 pion 的动量谱得到信号。两种方法得出的结果一致，加权平均值为 319.5 ± 57.6 pb。这是在产生阈附近的首次测量，该实验结果与理论预言有很大的差异。在阈值附近，中性重子对相空间因子 $\beta = \sqrt{1-4m_B^2/s}$ 接近于零，因此相应的截面也应该接近于零。非零的截面说明除了相空间之外，还应该存在其他的阈值效应。另外，利用在其他能量点的数据（$\sqrt{s}$ =2400.0, 2800.0, 3080.0 MeV），我们通过重建 $\Lambda/\overline{\Lambda} \to p\pi^-/\bar{p}\pi^+$，测量了 $e^+e^- \to \Lambda\overline{\Lambda}$ 的玻恩截面及有效形状因子，结果与之前 BaBar 实验符合，截面误差范围在 20.9% 至 33.3% 之间，误差也主要受统计量限制。而且由于没有足够统计量测量 Λ 电磁形状因子之比，Λ 角动量的不确定性成为最主要的一项系统误差。

在低能区域，由于强相互作用跑动耦合常数 α_s 和夸克胶子禁闭，微扰 QCD 理论不再适用。因此，各种非微扰 QCD 理论如格点量子色动力学（LQCD），手征微扰理论（ChPT) 等对低能区的强相互作用提供一定精度的理论预言。BEPCII 工作能区介于微扰与非微扰能区之间，通过 BESIII 上积累的大量数据，可以精确测量一些基本参数与 QCD 计算比较，对各类理论模型和预言进行检验。本文中，我们利用 BESIII 上取的 225 M J/ψ 数据，首次观测到

$J/\psi \to p\bar{p}a_0(980)$，$a_0(980) \to \pi^0\eta$ 过程并测得其分支比为 $(6.8\pm1.2\pm1.3)\times10^{-5}$，信号统计显著性为 6.5σ。实验结果提供了介子 $a_0(980)$ 耦合质子反质子对在阈值产生的信息，并且对 ChPT 的理论预言进行定量的比较。ChPT 预言了 J/ψ 四体衰变过程 $J/\psi \to p\bar{p}\pi^0\eta$ 的产生振幅, $a_0(980)$ 由 $\pi^0\eta$ 的相互作用产生，通过与实验的测量结果进行比较，可以对 ChPT 计算介子 - 介子振幅的未知参数提供实验输入值。

关键词： 质子，Λ，玻恩截面，形状因子，阈值，J/ψ，分支比

ABSTRACT

Study of the internal structure of the nucleon is of high significance to particle physics. The nucleons are not point-like particles, and the most direct evidence is the observed anomalous magnetic moment of nucleons ($\mu_p = 2.79\mu_N$, $\mu_n = -1.91\mu_N$), while theoretically, the magnetic moment of point-like proton and neutron is μ_N and 0, respectively. Another evidence is from elastic scattering of electrons on nucleons. The differential cross section of the elastic scattering is different from point-like Dirac scattering, which brings the definition of nucleon form factors (FF). The FFs are semi-empirical formula in effective quantum field which help describe the spatial distributions of electric charge and current. Besides, the FFs constitute a rigorous test of QCD as well as of phenomenological models. The FFs can be measured in space-like region (four-momentum transfer $q^2 < 0$) and time-like region ($q^2 > 0$). In the last forty years, lots of experiments were performed to extract the space-like FFs, relatively few to extract time-like nucleon FFs. There are still many mysteries on the shapes of proton FFs, such as the very steep rise towards threshold, two rapid decreases of the FFs and the poor precision of electromagnetic FF ratio ($|G_E/G_M|$). Moreover, the knowledge on neutron FFs and other baryon FFs are very poor and far from being understood. Therefore, systematic study on FFs and precision measurement of FFs are mandatory.

BEPCII is a double-ring e^+e^- collider running in 2.0 - 4.6 GeV center-of-mass energies. The designed luminosity is 1.0×10^{33} cm^{-2}s^{-1} at the optimized c.m. energy, $\sqrt{s}$=3770 MeV. BESIII is the only detector operating at BEPCII. In this thesis, by using data samples collected in continuum region with the BESIII detector, we measured the Born cross section of $e^+e^- \to p\bar{p}$ at 14 c.m. energies from 2232.4 to 3671.0 MeV.

Identification of proton/antiproton has been achieved mostly by means of the combined information of dE/dx and TOF, and after the requirements on momentum and back-to-back angle, the signal is selected with large signal-to-noise ratio. The measured cross sections are in agreement with recent results from BaBar, improving the overall uncertainty by about 30%. The corresponding effective electromagnetic FF of the proton is deduced by assuming (as it is the definition of effective FF) the electric and magnetic FFs to be equal ($|G_E| = |G_M|$). Moreover, the ratio of electric to magnetic FFs, $|G_E/G_M|$, and $|G_M|$ are extracted by fitting the distribution of the polar angle of the proton for the data samples with larger statistics, namely at $\sqrt{s} = 2232.4$ and 2400.0 MeV and a combined sample at $\sqrt{s}$ = 3050.0, 3060.0 and 3080.0 MeV, respectively. For these energies the $|G_E/G_M|$ ratios are close to unity and consistent with BaBar results at the same q^2 region. The precision of $|G_E/G_M|$ is limited by statistics, being between 25% and 50%. Therefore the data at these energies are consistent with the assumption that $|G_E| = |G_M|$, within the aforementioned uncertainties.

In addition to the proton FF, we also studied the process of electron positron annihilation into $\Lambda\overline{\Lambda}$ pair and measured its production cross section as well as the effective FF of Λ. With the data collected at 2232.4 MeV with the BESIII, that is only 1.0 MeV above the $\Lambda\overline{\Lambda}$ threshold, we measured the Born cross section of $e^+e^- \to \Lambda\overline{\Lambda}$ by two methods, namely *i)* reconstructing charged decay channel of $\Lambda/\overline{\Lambda}$ ($\Lambda/\overline{\Lambda} \to p\pi^-/\bar{p}\pi^+$). Since the momentum of the final states are less than 200 MeV, the pions are circling in MDC, and the track of proton/antiproton can not be reconstructed in MDC. Therefore, the signals are extracted by fitting the vertex of secondary particles produced from interactions between antiproton and beampipe. *ii)* by reconstructing neutral decay channel of $\overline{\Lambda}$ ($\overline{\Lambda} \to \bar{n}\pi^0$). Good events are identified through multiple variable analysis since antineutron leaves information in EMC, and the extraction of the signal is achieved by fitting the momentum of the neutral pion, since $\overline{\Lambda}$ is almost at rest. The measured Born cross section of this two methods are consistent, and the combined result is 319.5 ± 57.6 pb. It is the first measurement of $e^+e^- \to \Lambda\overline{\Lambda}$ near threshold. It contradicts the standard theoretical prejudice, which is that the cross section should vanish at 2232.4 MeV, since the phase space factor $\beta = \sqrt{1 - 4m_B^2/s}$ is close to 0. This result strongly suggests

that something more is at play here beyond the expected phase space behavior. Besides, with the data collected at 2400.0, 2800.0, 3080.0 MeV, we measured the cross section of $e^+e^- \to \Lambda\overline{\Lambda}$ and extracted the corresponding effective FF. The precision is between 22% and 33%, limited by statistics. Moreover, since the $|G_E/G_m|$ ratio of Λ was not measured due to the statistics limitation, the uncertainty from the Λ angular distribution becomes an important source in the systematic error.

At low energy region, because of the growing of the running QCD coupling constant and the associated confinement of quarks and gluons, it is meaningless to apply perturbative QCD. BEPCII is a machine operating in the energy region connecting non-pQCD to pQCD, The experimental results at BESIII is an important input for various QCD-based theoretical models.

In this thesis, by using 2.25×10^8 J/ψ events collected with BESIII, we for the first time observed the process $J/\psi \to p\bar{p}a_0(980)$, $a_0(980) \to \pi^0\eta$, with a significance of 6.5σ (3.2σ including systematic uncertainties). The product branching fraction of $J/\psi \to p\bar{p}a_0(980) \to p\bar{p}\pi^0\eta$ is measured to be $(6.8 \pm 1.2 \pm 1.3) \times 10^{-5}$. This measurement provides information on the a_0 production near threshold coupling to $p\bar{p}$ and improves the understanding of the dynamics of J/ψ decays to four body processes. The effective field theory, Chiral Perturbation Theory (ChPT) predicts the amplitude of $J/\psi \to p\bar{p}\pi^0\eta$ with $a_0(980)$ meson generated through final state interaction with some free coefficients. The experimental result will provide a quantitative comparison with the chiral unitary approach and helps settle these coefficients.

Keywords: proton, Λ, Born cross section, form factor, threshold, J/ψ, branch fraction

目　录

List of Tables

List of Figures

Chapter 1

Introduction

1.1 Standard Model and Quantum Chromodynamics

1.1.1 Standard Model

The Standard Model (SM) of particle physics, which was formulated in the 1970s, describes the universe in terms of fundamental particles and the electromagnetic, weak and strong interactions. It had successfully explained the existence of quarks and predicted more particles which had turned out to be discovered, such as the W/Z bosons (1983), top quark (1995), tau neutrino (2000), and recently, the Higgs boson (2013). Figure 1.1 shows the framework of SM, where 17 fundamental particles are presented and they can be classified into three categories.

a. Quarks. In the present SM, there are three generations of quarks, which are all confirmed from experiments. They are all fermions of spin $1/2$ and should obey the Pauli exclusion principle. There are six kinds of flavor: up (u), down (d), strange (s), charm (c), bottom (b), and top (t); their antiparticles, called antiquarks, are expressed as $\bar{u}$, $\bar{d}$, $\bar{s}$, $\bar{c}$, $\bar{b}$ and $\bar{t}$. They can form into mesons and baryons. The most fundamental baryons are the proton and neutron, which are each constructed from ”up” and ”down” quarks. Quarks are observed only in combinations of two quarks (mesons), three quarks (baryons). Apart from the conventional quark combinations, the exotic quark combinations, which are not forbidden by quantum chromodynamics (QCD), is barely observed in experimental particle physics. However, recently experiments at BESIII and Belle show some hints of particles contain four quarks (tetraquark) [1, 2], $c\bar{c}u\bar{d}$, but more data are called to confirm it. The electric charges, color charges and masses of the six flavor quarks are shown in Fig. 1.1. To make baryons with integer charges, the quarks need to be assigned fractional electric charge: $+2/3$ for u, c, t, and $-1/3$ for d, s, b. The "color" of quarks is proposed to reconcile the baryon spectrum with the spin-statistics theorem by Nambu, Greenberg, and Gell-Mann. If the quark wavefunctions are symmetric in spin and flavor, they are totally antisymmetric with color quantum numbers, in agreement with Fermi-Dirac statistics. Besides, the model of color could assign quark to the fundamental representation of a new global symmetry, the QCD, which will be introduced in detail in section 1.1.2. The masses of quarks are only rough estimations, since the confinement of quarks implies that we cannot isolate the quarks and measure their masses precisely. The important property of quarks and QCD is asymptotic freedom, which means that in very high momentum transfer, the force between two quarks are very small and the quarks behave like free particles. Quarks have color charge, electric charge and weak charge and are involved in strong interactions, electromagnetic interactions and weak interactions.

b. Leptons. There are six types of leptons, again in three generations, which are electron, muon, tau and their neutrino partners. They are fermions of spin $1/2$ and obey Pauli exclusion principle. The electron has the lowest mass of all the charged leptons and is stable. It is the very first fundamental particle, observed by J. J. Thomson through the explorations on the properties of cathode rays in 1987. The muon were discovered by Carl D. Anderson in 1937, while studying cosmic radiation. It is an unstable subatomic particle with a mean lifetime $T_0 = 2.2\ \mu s$. It can decay to an electron or positron, via $\mu^- \rightarrow e^- + \bar{\nu}_e + \nu_\mu$. The fact that this decay is a three-particle one is due to the conservation of lepton number. In relativistic mechanics, when the muon has a momentum of 1 GeV/c, the decay length is over 6000 m, calculated by $L = \gamma T_0 \times v$, where $\gamma = \frac{1}{\sqrt{1-v^2/c^2}}$. The tau is the most massive lepton and it is the only lepton that can decay into hadrons through the weak interaction. The electron, muon and tau have both electric and weak charge. They are involved in electromagnetic and weak interactions. Neutrinos have very little mass and interact so weakly with the rest of the particles,

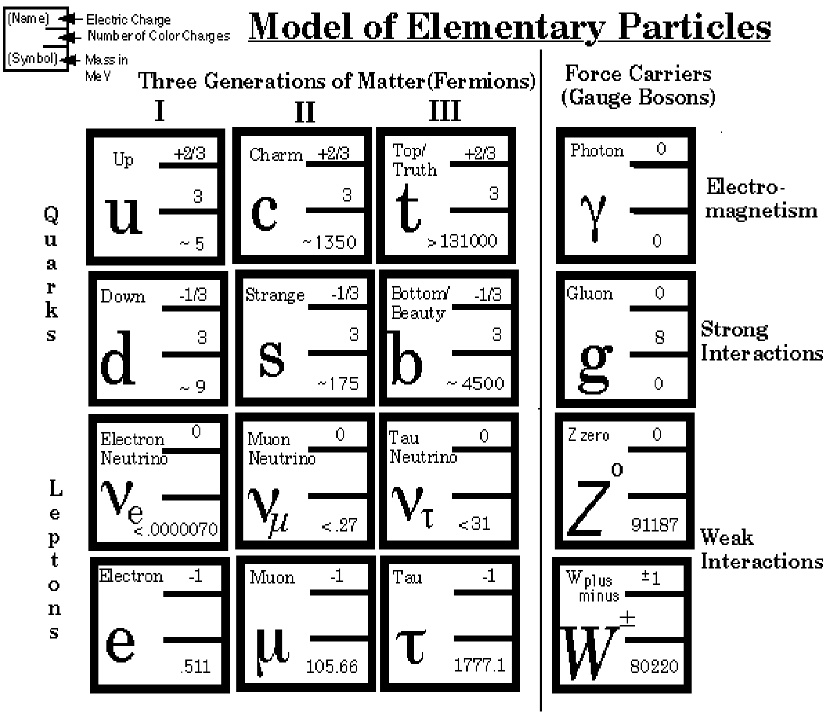

Figure 1.1 The framework of the Standard Model

which make it particularly difficult to detect them. Since the neutrinos only have weak charge, they can only be involved in weak interactions.

c. Gauge bosons. Gauge bosons mediate the interactions (forces) between elementary particles. Different vector bosons are for different types of interactions: photons for electromagnetic force, described by quantum electrodynamics (QED); gluons for the strong force, described by QCD; $W^{\pm}$ and Z for the weak force, which is well understood by unified electro-weak theory (EWT). Gluons and photons are found to be massless, and W and Z bosons have large masses, which is the main reason that weak interactions are much "weaker" than electromagnetic interactions. The strong interactions bound quarks together in clusters to make other subatomic particles. The OZI (Okubo-Zweig-Izuka) rule determines which strong processes are preferred under the circumstance they are allowed by G parity conservation and other required conservations. It can be summarized saying that decays that correspond to disconnected quark diagrams are very strongly suppressed. For example, the ϕ meson decays into strange

$K\bar{K}$ is preferred (49.1%) than decays into $\pi^+\pi^-\pi^0$ (2.5%). The Feynman diagrams of the two strong interactions can be found in Fig. 1.2. The weak interaction is caused by emission or absorption of massive $W^{\pm}$ or Z bosons. It is the only process in which a lepton can change into another lepton, or a quark into another quark, as named charged-current weak interaction. The fundamental interaction vertexes are $\nu_l \rightarrow W^+ + l^-$ for leptons, and $u \rightarrow W^+ + d$ for quarks. The lepton number must be conserved in the lepton exchange. When the quark flavor changes, a three-by three matrix, named CKM matrix, gives the probability of each kind of flavor changes by connecting the weak eigenstates and the mass eigenstates. The CKM matrix indicates that the flavor changing in different generations of quarks is suppressed. The neutral interaction is via exchanging Z boson, but it is rarely observed because it competes with the much stronger electromagnetic interaction. There is no flavor-change neutral current in weak interaction, such as $d \rightarrow s + Z \rightarrow s + \nu_l + \bar{\nu}_l$, which was not observed experimentally.

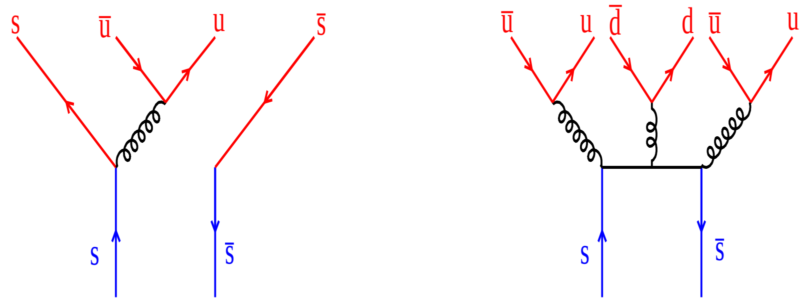

Figure 1.2 Feynman diagram of OZI favored process $\phi \rightarrow K^+K^-$ (a) and OZI suppressed process $\phi \rightarrow \pi^+\pi^-\pi^0$ (b).

In the SM, the fundamental particles shown in Fig. 1.1 are initially massless. The masses are generated through interactions with a scalar field, the Higgs field, without violating the gauge theory. The SM model predicts that at least one Higgs particle relevant within the possible Higgs fields exists. In July, 2012, the ATLAS and CMS experiments at CERN's Large Hadron Collider, both observed a neutral boson in the mass region around 126 GeV [4, 5], and the decay to two photons indicates that the new particle is a boson with spin different from one. The results is consistent with the expectations from the SM Higgs boson, within uncertainties. The discovery of the

Higgs candidate provides rigorous test for the validity of the SM, but more data are needed to access the nature of Higgs boson and investigate the physics beyond the SM.

1.1.2 Quantum Chromodynamics

The quantum chromodynamics is a model of strong interactions which is a renormalizable non-Abelian gauge theory with gauge group SU(3). It describes the quarks which are bound together by exchanging gluons to form color-singlet hadrons. Such dynamics are described by the QCD Lagrangian:

$$\mathcal{L}_{QCD} = \bar{\psi}^i_q (i\gamma^\mu)(\mathcal{D}_\mu)_{ij}\psi^j_q - m_q\bar{\psi}^i_q\psi_{qi} - \frac{1}{4}F^a_{\mu\nu}F^{a\mu\nu}, \tag{1.1}$$

where the field strength tensor for a gluon with color index a is

$$F^a_{\mu\nu}F^{a\mu\nu} = \partial_\mu A^a_\nu - \partial_\nu A^a_\mu - g_s f^{akl} A^\mu_k A^\nu_l, \tag{1.2}$$

the local gauge covariant derivative

$$(\mathcal{D}^\mu)_{ij} = \delta_{ij}\partial_\mu - ig_s t^a_{ij} A^a_\mu, \tag{1.3}$$

ψ^i_q denotes a quark field with color index i, g_s is the strong coupling constant, f^{abc} are the structure constants of the SU(3) group and $A^a_\mu(x)$ are the gluon fields with color index a.

An example of the application of the SU(3) group theory to QCD is that it can examine which states we can obtain by combinations of quarks and gluons. Due to the confinement property of QCD (supposed, but not proven yet), no free quark or color can be observed. Therefore, combination of quarks into a particle should be color-singlet. A color-singlet baryon consists of three quarks. According to the SU(3) group, baryons are given by the following product decomposition:

$$3 \otimes 3 \otimes 3 = 10 \oplus 8 \oplus 8 \oplus 1, \tag{1.4}$$

and mesons which made of two quarks are

$$3 \otimes \bar{3} = 1 \oplus 8. \tag{1.5}$$

SU(3)-flavor symmetry implies the existence of flavor singlets, octets and decuplets. In the spectrum of the lowest-lying baryons states, uds, there are eight ground state baryons that corresponding to an octet with $J^P = \frac{1}{2}^+$, and ten states of a decuplet with $J^P = \frac{3}{2}^+$ as shown in Fig. 1.3 in the array of $Y - I_3$, where I_3 is the third component of isospin, $Y = B + S$ is the sum of baryon quantum number and strange quantum number. There was one baryon predicted by SU(3) not observed at the time when the picture was formed, the Ω^- particle, made of three strange quarks, with a mass predicted to be around 1684 MeV. In 1964, the evidence of Ω^- particle was observed in a bubble chamber experiment, with the measured invariant mass and other parameters very close to predicted ones. The discovery of Ω^- indicates the SU(3) group is well established. The lightest two baryons are proton and neutron. The lightest baryon containing a charm quark is Λ_c. Similarly, in the meson spectrum, there exist octet and singlet states, and they can form into two different J^{PC} in ground states since the spin of $q\bar{q}$ system can be 0 or 1. Figure 1.4 shows the states of nine pseudoscalars ($J^P = 0^-$) and nine vectors ($J^P = 1^-$) in the array of $S - I_3$. The QCD theory does not forbid formations of the so-called ”exotics”, such as a color-singlet constituent other than the conventional $q\bar{q}$ or qqq hadrons. These include glueballs, made only of gluons; hybrids, made of both quarks and gluons; multiquark states, such as tetraquarks, pentaquarks. Such states, if they exist, will help in deepening our understanding of the properties of QCD.

Another famous property of QCD, called asymptotic freedom already mentioned, is that the closer the quarks are to each other, the weaker is the ”color charge”. When the quarks are really close to each other, the force is so weak that they behave almost as free particles. This is the discovery by D. Gross, H. Politzer, and F. Wilczek and they were awarded the Nobel Prize in physics in 2004. Numerically, the value of strong coupling α_s is running with the energy. The coupling can be given at the specific scale

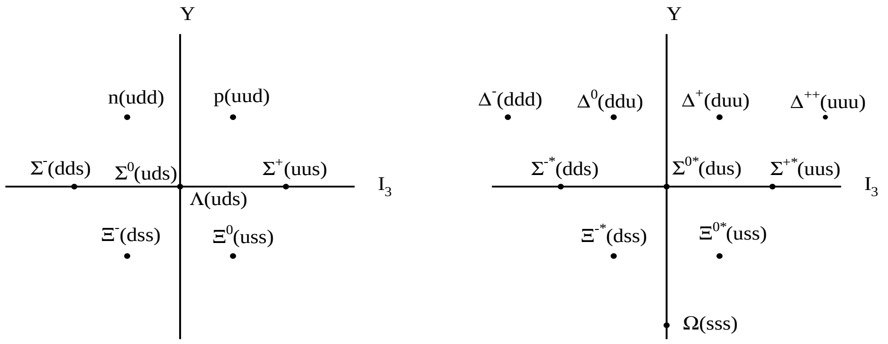

Figure 1.3 An example of the flavor SU(3) (a) octet of $J^P = \frac{1}{2}^+$ baryons and (b) SU(3) decuplet of $J^P = \frac{3}{2}^+$ baryons in the array of $Y - I_3$.

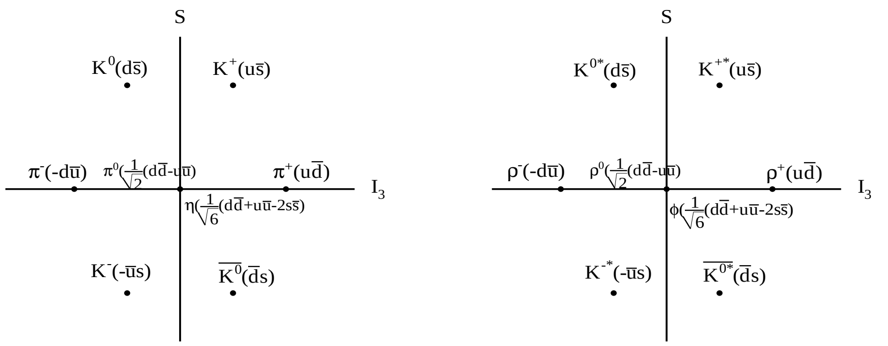

Figure 1.4 An example of (a) the octet of $J^P = 0^-$ psedoscalar mesons in the array of $S - I_3$ and (b)the octet of $J^P = 1^-$ vector mesons.

$Q^2 = M_Z^2$, from which we can obtain its value at any energy scale:

$$\alpha_s(Q^2) = \alpha_s(M_Z^2)\frac{1}{1 + b_0\alpha_s(M_Z^2)\ln\frac{Q^2}{M_Z^2} + \mathcal{O}(\alpha_s^2)}. \tag{1.6}$$

Figure 1.5 illustrates the running of α_s in a theoretical calculation and in physical processes at different energy scale. They both show evidence of running-α_s. To make this divergence explicit, we can rewrite Eq. 1.6 in the form:

$$\alpha_s(Q^2) = \frac{2\pi}{b_0\ln\frac{Q^2}{\Lambda_{QCD}^2}}. \tag{1.7}$$

The formula is the clearest expression of the statement that α_s becomes small as $(log(Q))^{-1}$ for large Q. The momentum scale Λ_{QCD} is the scale at which α_s becomes strong as Q^2 is decreased. Experimental measurements yield a value of $\Lambda_{QCD} \sim 200$ MeV.

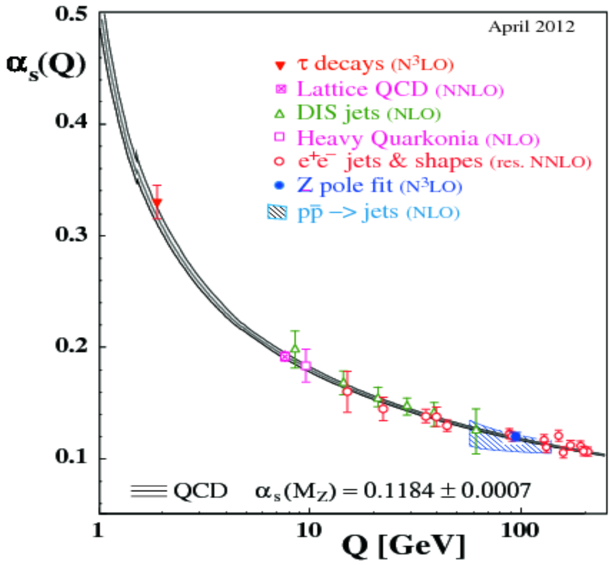

Figure 1.5 The running of α_s in theoretical calculation (band) and in physical processes at different energy scales.

Among the consequences of asymptotic freedom, there is that a perturbation expansion becomes meaningful at higher energy scales, $Q \gg \Lambda_{QCD}$. Although strong interactions are troublesome at small energies, they become simple when the energies are large so that $\alpha_s \ll 1$, and thus makes the leading order to be dominant. Experience shows that perturbative calculations give a resonable descriptions of hadronic scattering when the momentum transfer exceeds several GeVs.

At low energies, as the growing of running strong coupling α_s and the associated confinement of quarks and gluons, perturbative QCD becomes meaningless. Effective field theories are then introduced to describe the strong interactions of quarks and gluons at low energies, of which, the Chiral perturbation theory (ChPT) deals directly with mesons and baryons [6, 7]. It incorporates the basic symmetries of QCD into an effective Lagrangian expanded in powers of the external momenta of hadrons, since in the low energy, the degrees of freedom are no longer quarks or gluons, but hadrons. ChPT describes not only meson-meson or meson-baryon interactions at lowest order, it also experimentally well satisfies the Gell-Mann-Okubo relation which can be expressed like:

$$m_8^2 = \frac{1}{3}(4m_{K^*}^2 - m_\rho^2), \tag{1.8}$$

where m_8 is the mass of the eighth component of vector meson octet, m_{K^*} and m_ρ are the mass of K^* and ρ, respectively. However, a drawback of ChPT is its limited range of convergence. For example, for meson meson interaction, the limitation appears around 500 MeV where the σ pole shows up. Therefore, plain ChPT can do little for the investigation of the interesting resonances that occur in meson spectroscopy. However, a chiral unitary coupled channels approach has proven to be successful in describing meson meson and meson baryon interactions in all channels up to energies around 1.2 GeV in meson meson and 1.6 GeV in meson baryon interactions [8].

Lattice QCD is another tool for calculating the hadronic spectrum and the matrix elements of any operator within these hadronic states from first principles. Lattice QCD is QCD formulated on a discrete Euclidean space time grid. It still retains the fundamental characters of QCD. The discrete space-time lattice acts as a non-perturbative scheme with a finite values of the lattice spacing "a", yield an ultraviolet cutoff at π/a. As the spacing is reduced to zero, one could do the standard perturbative calculations using lattice regularization. However, these calculations are much complicated, therefore, LQCD can be simulated on the computer using methods analogous to those used for Statistical Mechanics systems. A very useful feature of LQCD is that the dependence of running α_s and the quark masses can be detailed predicted, which can be used to constrain effective theories like ChPT and so on.

1.1.3 Experimental Tests of QCD

Experimental tests of QCD-motivated models are very helpful for providing understanding of the strong interactions and for giving guidance to the development of nonperturbative QCD techniques. The upgraded Beijing Electron Positron Collider (BEPCII), an e^+e^- collider, which will be introduced in detail in next chapter, is a machine operating in the energy region of 2.0 - 4.6 GeV. This energy region connects nonperturbative QCD and the perturbative QCD regime. The collected J/ψ sample is the world record. Using J/ψ decays, one can study light hadron spectroscopy, search for new hadronic states and study the exotic mesons.

Measurements of exclusive light hadronic final states provide valuable information concerning physics of light quark resonance, nonperturbative QCD and hadron-production mechanism. Besides, exclusive cross sections can be written as functions of form factors that embody the influence of the strong interaction on the properties of electromagnetic interaction vertices. Precise measurements of hadronic form factors helps promote the understanding to the strong interaction. The experiments on exclusive cross sections and form factors are important inputs for various QCD-based theoretical models.

1.2 Nucleon Electromagnetic Form Factors

The Universe, to our current understanding, consists of 73% dark energy, 23% dark matter, and almost 4% visible matter which is made of proton, neutron and electron, bounded together by nuclear and electromagnetic forces into atoms and molecules. Therefore, nucleons constitute most of the visible matter. Understanding the internal structure of the nucleon is of high significance to particle physics.

The nucleons are not point-like particles, and the most direct evidence is the anomalous magnetic moment of proton and neutron. In Dirac function, the magnetic moment of a point-like proton is μ_N, where $\mu_N = \frac{e\hbar}{2M_p c}$ is the nuclear magneton, and the magnetic moment of a point-like neutron is 0. The measured magnetic moment of proton and neutron are 2.79μ_N and -1.91μ_N, respectively. The anomalous magnetic moment indicates that there exists an internal structure in the nucleons. Another evidence is from elastic scattering of electrons and protons. Theoretically, the differential cross section of the elastic scattering of point-like electron and point-like proton is Dirac scattering, expressed as:

$$(\frac{d\sigma}{d\Omega})_{ep} = (\frac{d\sigma}{d\Omega})_{\text{Mott}}(1 + 2\tau \tan^2 \frac{\theta}{2}), \tag{1.9}$$

where $(\frac{d\sigma}{d\Omega})_{\text{Mott}}$ refers to the Mott scattering of a electron and a spin 0, point-like charged particle. In the experiment of elastic scattering of 188 MeV electrons from gaseous target of hydrogen [9], the cross section against laboratory angles between 35° and 138° are measured as shown in Fig. 1.6. A comparison has been made with theoretical prediction as Eq. 1.9 and a modified Mott formula which takes into account both the anomalous magnetic moment of the proton and a finite size effect. The comparison shows that a finite size of the proton will account for the results.

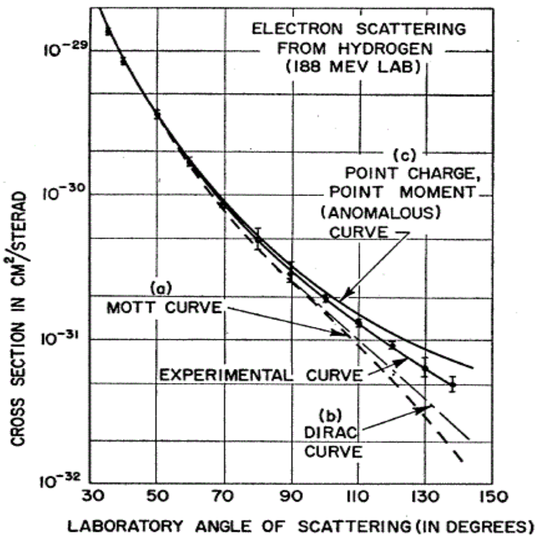

Figure 1.6 Experimental differential cross section of the elastic scattering of electron and proton, compared with theoretical prediction curve. Figure taken from Ref. [9]

The modified Mott formula, as introduced before, can be expressed by introducing the form factors (FFs). The FFs are semi-empirical functions, which help to describe the spatial distributions of electric charge and current and are among the most basic observable of the nucleon.

1.2.1 Introduce of Proton FFs

Proton FFs can be measured by means of elastic scattering of a lepton with a target proton, by means of electron-positron annihilation into proton-antiproton, as well as proton-antiproton annihilation into a lepton pair. It is assumed that the one-photon exchange approximation is valid. The lowest order Feynman diagram of lepton - proton scattering is shown in Fig 1.7(a). The momentum transfer squared, q^2, is negative and the FFs are by definition space-like. The lowest order e^+e^- annihilation process is shown in Fig. 1.7(b), q^2 is positive and the FFs are time-like. The basic kinematic variables are also shown in Fig. 1.7, where k, k' are the electron momenta and p, p' are the proton momenta. Since the electromagnetic vertex of the lepton is well-known, one can reliably extract the proton electromagnetic vertex Γ^μ by measuring cross section and polarization. Assuming the aforementioned one-photon exchange, i.e. in the Born approximation, and under the basic requirements of Lorentz invariance, hadronic vertex can be parameterized in terms of two FFs, F_1 and F_2,

$$\Gamma_\mu(p^{'}, p) = \gamma_\mu F_1(q^2) + \frac{i\sigma_{\mu\nu}q^\nu}{2m_p}\kappa_p F_2(q^2), \tag{1.10}$$

where m_p is the mass of proton, $\kappa_p = \frac{g_p-2}{2}$ is the anomalous magnetic moment, $g_p = \frac{\mu_p}{J}$, $\mu_p = 2.79$ is the magnetic moment of the proton and $J = \frac{1}{2}$ is the spin. The functions F_1 and F_2 are called Dirac and Pauli FF, respectively. The optical theorem, applied to lepton- nucleon scattering, implies that at the lowest order the FFs are real in the SL region, i.e. the complex conjugate of the amplitude in Fig. 1.7(a), $\mathcal{M}^+$, is identical to $\mathcal{M}$. In the TL region, as in in Fig. 1.7(b), the FFs can be complex above the first hadronic threshold, that is twice the pion mass.

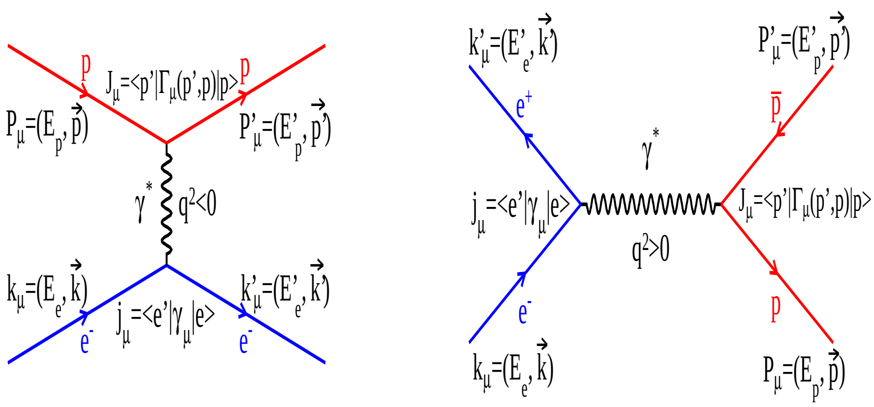

Figure 1.7 Feynman diagram of (a) $ep \to ep$ elastic scattering and (b) $e^+e^- \to p\bar{p}$ at the lowest order.

The Sachs FFs, electric G_E and magnetic G_M, are introduced as linear combinations of Dirac and Pauli FFs. Concerning the SL region, G_E and G_M are the Fourier transform of the charge and magnetization distribution of the nucleon, respectively. In the Breit frame G_M and G_E are spin-flip and non spin-flip amplitudes, respectively. They are expressed as

$$G_E(q^2) = F_1(q^2) + \tau\kappa_p F_2(q^2), \tag{1.11}$$

$$G_M(q^2) = F_1(q^2) + \kappa_p F_2(q^2). \tag{1.12}$$

where $\tau = \frac{q^2}{4m_p^2}$. At $q^2 = 0$, $F_1 = F_2 = 1$ and $G_E = G_M/\mu_p = 1$. In the TL region, the c.m. system is equivalent to the Breit frame since the helicities of bayons are opposite for the spinors aligned in G_M and the same for the spinors aligned in G_E.

1.2.2 Proton FFs in Space-like Region

In the SL region, the standard technique for the extraction of proton FF is through Rosenbluth separation [10]. In the one-photon exchange approximation, the cross section of unpolarized elastic scattering of electrons on target protons can be written as

$$\frac{d\sigma}{d\Omega} = (\frac{d\sigma}{d\Omega})_{\text{Mott}}[G_E^2 + \frac{\tau}{\epsilon}G_M^2]\frac{1}{1+\tau}, \tag{1.13}$$

where $\epsilon = 1/[1+2(1+\tau)\tan^2(\theta_e/2)]$ is the longitudinal polarization of the photon and θ_e is the electron scattering angle. The Rosenbluth separation, $\sigma_R = \frac{\epsilon}{\tau}G_E^2 + G_M^2$, depends linearly on ϵ. By measuring the differential cross section at different θ_e at the fixed q^2, one can extract both G_E and G_M. Experimental results of Rosenbluth separation can be found in Ref. [11] performed in SLAC from $Q^2 = 1.75$ to 8.83 GeV/c^2, where $Q^2 = -q^2 \geq 0$. The ratio $\mu_p G_E/G_M$ is observed to approach a constant value for $Q^2 > 3$ GeV/c^2. As well as the experiment performed in JLab [12] at Q^2 values of 2.64, 3.20 and 4.10 GeV^2 and shows a similar trend on $\mu_p G_E/G_M$.

A more recently method of extracting FFs in SL region is by elastic scattering of longitudinally polarized electrons on target proton $\overrightarrow{e} + p \rightarrow e + \overrightarrow{p}$. For one-photon exchange, the scattering of longitudinally polarized electrons results in a transfer of polarization to the recoil proton with only two non-zero components, P_l, parallel to the proton momentum and P_t, perpendicular to the proton momentum in the scattering plane. The ratio are given by

$$\frac{G_E}{G_M} = \frac{P_t}{P_l} \frac{E_e + E_{beam}}{2M_p} \tan\frac{\theta}{2} \tag{1.14}$$

The ratio G_E/G_M is obtained from a single measurement of the two recoil polarization components, where the Rosenbluth method required at least two cross section measurements made at different energies and angle combinations at the same Q^2. Results from the GEp-II experiment at JLab's Hall A [13, 14] for $\mu_p G_E/G_M$ by means of recoil proton polarization transfer method show that this ratio decreases rather quickly with increasing Q^2, which is inconsistent with the Rosenbluth method. One possible explanation could be higher order corrections (two photon exchange) to the elastic scattering process. It is assumed that these corrections do not affect significantly the results of the polarization transfer experiment, while are important in the Rosenbluth case. A small correction to the Rosenbluth separation could imply a large correction for the extracting of G_E, since G_E is the slope of Resenbluth plot. The two-photon exchange (TPE) correction has received considerable attention to explain this discrepancy. A direct measurement of the TPE contribution is given by the ratio of positron and electron elastic scattering $R^{e^+e^-}(\epsilon, Q^2) = \sigma(e^+p)/\sigma(e^-p)$. And the correction factor to the e^-p elastic cross section due to TPE is $1-(R^{e^+e^-}-1)/2$. The results suggest that TPE can provide an explanation for the observed discrepancy. However, there are not yet precise theoretical calculations of two photon exchange that can resolve the discrepancy. This puzzle shows how poor is still our knowledge of FFs.

1.2.3 Proton FFs in Time-like Region

In the TL region, measurements can be performed by means of electron-positron annihilation into a proton-antiproton pair. The final pair is produced in the states $^3S_1$ and $^3D_1$ as follows directly from angular momentum and parity considerations. Analyticity of Dirac and Pauli FFs (that is they should be continuous functions through the threshold) implies that G_E and G_M should be equal at threshold. Therefore the threshold angular dependence is expected to be isotropic and at threshold the D wave contribution should vanish. By the way BaBar present data do not confirm this assumption. Unfortunately the BaBar angular distribution, close to the threshold, is integrated on a finite energy interval. So, in principle, the ratio $|G_E/G_M|$ could become equal to 1 suddenly. Until now this is the standard point of view. In 1961, Cabibbo and Gatto discussed possible experiments with high-energy colliding beams of electron and positron in Ref. [15], where annihilation into baryon-antibaryon pairs is investigated and polarization effects arising from the nonreal character of the FFs on the absorptive cut are examined. In one-photon exchange approximation and by setting the electron mass to zero, the cross section is expressed in the form

$$\frac{d\sigma}{d\cos\theta_p} = \frac{\pi\alpha^2\beta}{2s^2}[|G_M|^2(1+\cos^2\theta_p) + \frac{1}{\tau}|G_E|^2\sin^2\theta_p], \tag{1.15}$$

where $\alpha = 1/137$ is the fine structure constant, $s = q^2$ is the square of center-of-mass energy, $\beta = \sqrt{1-4m_p^2/s}$ is the velocity of proton in e^+e^- c.m. system, and θ_p is the polar angle of proton in e^+e^- c.m. system. However, it has been pointed out that final state Coulomb correction to the Born cross section has to be taken into account in the case of charged fermion pair production. This correction has been usually introduced as an enhancement factor, C, corresponding to the Coulomb scattering S-wave function at the origin, squared. It is usually assumed to be the same as in the case of pointlike fermions (even in the case of a baryon pair), since Coulomb interaction is a long range interaction added to a short range one,therefore acting after the baryons have been built. In conclusion, it is assumed that C is the so called Sommerfeld-Schwinger-Sakharov rescattering formula [16]. This factor has a weak dependence on the fermion pair total spin, it is the same for G_E and G_M and can be factorized. The Coulomb enhancement factor for charged baryon pair is

$$C = \frac{y}{1-e^{-y}}. \tag{1.16}$$

with

$$y = \frac{2m_p}{q}\frac{\alpha\pi}{\beta} \tag{1.17}$$

The Coulomb factor is the S-wave Sommerfeld-Gamow factor, that takes into account the QED leading-order correction to the wave-function of the charged pair, and results to be proportional to $|\Psi_{p\bar{p}}(0)|^2$, where $|\Psi_{p\bar{p}}(0)|$ is the relative wave-function in the continuum. The distribution of Coulomb factor with invariant mass of $p\bar{p}$ system is shown in Fig. 1.8. Very near threshold Coulomb factor is $C \approx \pi\alpha/\beta$, therefore, the phase space factor β is cancelled and the cross section is expected to be finite and not vanishing even exactly at threshold. At the energies a few MeVs higher than threshold, the Coulomb correction factor should be safely assumed to be 1 with high precision. The BaBar data show that the cross section is roughly constant in a $\sim$ 200 MeV c.m. energy interval. Therefore there should be a kind of conspiracy between the Coulomb factor, which changes very quickly, and the FFs at threshold that should vary exactly in the opposite way. Another explanation could be that the $\mathcal{R}$ introduced in the resummation factor is not $\mathcal{R}_{em}$, but $\mathcal{R}_S$ taking into account that gluons, not only photons, are exchanged between the outgoing baryons. The threshold effect will be discussed in detail in Sec. 1.2.5. This question is still open and confirms that FFs are still far from being understood.

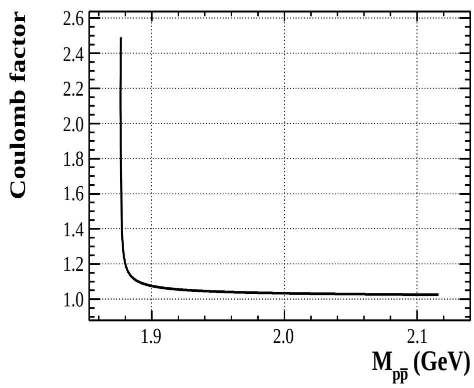

Figure 1.8 The distribution of Coulomb factor in dependence of $M_{p\bar{p}}$.

The FFs in TL region can also be measured from proton-antiproton annihilation to electron-positron pair, which is the inverse of electron-positron annihilation into a proton-antiproton pair. In the one-photon exchange approximation, the differential cross-section is the same as Eq. 1.15.

In the last forty year, many experiments have been performed to investigate the FFs in TL region through $e^+e^- \to p\bar{p}$ and $p^+p^- \to e^+e^-$ processes. Since the center-of-mass energies for these experiments are discrete, they are called scan experiments. These experiments are summarized in Table 1.1. The first measurements of a TL nucleon FF was performed at the e^+e^- collider ADONE in Frascati in 1972, using the process $e^+e^- \to p\bar{p}$ [17]. This historically first result was obtained with an optical s-park chambers setup at a center-of-mass energy (c.m energy) of $\sqrt{s} = 2.1$ GeV/c. In the following years a series of measurements were performed at the electron-positron colliders ADONE with the FENICE experiment [20], as well as at the Orsay colliding beam facility (DCI) with the detectors DM1 [18] and DM2 [19]. The em FF of the proton was explored by these facilities from nearly production threshold up to c.m. energies of 2.4 GeV/c. Precision measurements were also obtained with the BES-II experiment at BEPC [21], and with CLEO at CESR [22].

First attempts to measure the proton FF using the inverse reaction $p\bar{p} \to e^+e^-$ date back to the mid 1960's, while the first upper limits from antiproton beam experiments at BNL and CERN [23]. The discovery of this reaction was finally possible using an antiproton beam at PS/CERN in 1976 [24]. Antiproton experiments were later continued with great success at LEAR/CERN with the PS170 experiment and at FNAL.

Data in TL are collected in physical region, which is above the $p\bar{p}$ production threshold. The FFs in most experiments are calculated under the assumption $|G_E| = |G_M|$, while this assumption should hold only at $p\bar{p}$ threshold. In the PS170 experiment at LEAR [25], the $|G_E/G_M|$ ratio, from $p\bar{p}$ threshold up to $\sqrt{s} = 2.05$ GeV are presented. This is the only experiment that have measured the electromagnetic FFs ratios in scan experiments with uncertainties from 28.0% to 43.0%, and the electromagnetic FFs ratio shows a clear steep $\sqrt{s}$ dependence close to the threshold.

Besides the conventional scanning experiments, the FFs in TL can also be mea-

Table 1.1 Summary of the information from previous experiments. The precisions are for the cross sections.

Process	Date	Experiment	q^2 (GeV$^2/c^4$)	q^2 point	Event	Precision
$e^+e^- \to p\bar{p}$	1972	FENICE/ADONE [17]	4.3	1	27	24%
	1979	DM1/ORSAY-DCI [18]	3.75-4.56	4	70	25.0%
	1983	DM2/ORSAY-DC1 [19]	4.0-5.0	6	100	19.6%
	1998	FENICE/ADONE [20]	3.6-5.9	5	76	19.3%
	2005	BES/BEPC [21]	4.0-9.4	10	80	21.2%
	2006	CLEO/ [22]	13.48	1	16	33.3%
$p^+p^- \to e^+e^-$	1976	PS135/CERN [24]	3.52	1	29	15.7%
	1994	PS170/CERN [25]	3.52-4.18	9	3667	6.1%
	1993	E760/Fermi [26]	8.9-13.0	3	29	33.8%
	1999	E835/Fermi [27]	8.84-18.4	6	144	10.3%
	2003	E835/Fermi [28]	11.63-18.22	4	66	21.1%
$e^+e^- \to \gamma + p\bar{p}$	2006	BaBar/SLAC-PEPII [30]	3.57-19.1	38	3261	9.8%
	2013	BaBar/SLAC-PEPII [31]	3.57-19.1	38	6866	6.7%
	2013	BaBar/SLAC-PEPII [32]	9.61-36.0	8	140	18.4%

sured via initial-state-radiation (ISR) technique. The lowest-order of ISR process is $e^+e^- \to \gamma + p\bar{p}$. The Born cross section of this process, integrated over the nucleon momenta, is given by

$$\frac{d^2\sigma_{e^+e^-\to p\bar{p}\gamma}(M_{p\bar{p}})}{dM_{p\bar{p}}d\cos\theta_\gamma} = \frac{2M_{p\bar{p}}}{s}W(s,x,\theta_\gamma)\sigma_{p\bar{p}}(M_{p\bar{p}}), \tag{1.18}$$

where $\sigma_{p\bar{p}}(m)$ is the Born cross section for the nonradiative process $e^+e^- \to p\bar{p}$, $M_{p\bar{p}}$ is the $p\bar{p}$ invariant mass, $x = 2E_\gamma/\sqrt{s} = 1 - M_{p\bar{p}}^2/s$, E_γ and θ_γ are the ISR photon energy and polar angle in e^+e^- c.m. frame, respectively. W(s, x, θ_γ) is the probability of the initial state radiation of the photon with energy x$\sqrt{s}/2$ and polar angle θ_γ, as following:

$$W(s,x,\theta_\gamma) = \frac{\alpha}{\pi x}(\frac{2-2x+x^2}{\sin^2\theta_\gamma} - \frac{x^2}{2}). \tag{1.19}$$

There are two approaches for studying ISR events, untagged the ISR photon and tagged ISR photon. In the first approach, detection of ISR photon is not required, but all final hadrons must be detected and fully reconstructed. The ISR technique offers some advantages over conventional e^+e^- measurements. It can cover the entire hadronic mass range and the detection efficiency has low sensitively to hadron angular distributions in the hadronic system. The disadvantage of ISR is that the mass resolution and absolute mass scale calibration are much poorer than that of conventional scan experiments. In the BaBar experiment at PEP-II [30–32], the cross section was measured using ISR from $p\bar{p}$ production threshold up to $\sqrt{s} = 6.5$ GeV. The $|G_E/G_M|$ ratio was measured from threshold up to $\sqrt{s} = 3.0$ GeV, and the result shows an inconsistency with respect to the PS170 results, especially at low c.m. energies.

Concerning the effective FFs, though a lot of experiments have been performed to measure the TL FFs, the complex shape of proton TL FFs is largely not understood and has lead many speculations, which are summarized as following:

- The effective FF show very steep rise toward threshold as shown in Fig. 1.9, which can be clearly observed in BaBar and PS170 results. It has been speculated whether the threshold enhancement might be due to the existence of a hypothetical, narrow resonance with a mass just below threshold.

- From Fig. 1.9, we can find two rapid decreases of the FF near 2.25 GeV and 3.0 GeV indicates by the arrows. These steps are just below the threshold for $p\bar{\Delta}(1232)$ and $N(1520)\bar{N}(1520)$ and an s-wave threshold effect is suggested to be responsible for these structures [33].

- Perturbative QCD calculation predicts that the asymptotic values for SL and TL FFs to be identical at high energies. However, if one assumes that the effective FF could be an approximation of the TL magnetic FF, one finds that it is larger than the corresponding SL quantities by about a factor of two.

As discussed before, the FFs in TL have an imaginary part in physical region which can be estimated by the polarization of outgoing protons, even without a polarization of the incoming beams. In one-photon approximation, the polarization of proton perpendicular to the scattering plane is given by [34]

$$P_y = -\frac{\sin 2\theta Im(G_E(q^2)G_M^*(q^2))}{D\sqrt{\tau}} = -\frac{\sin 2\theta |G_E(q^2)||G_M(q^2)| \sin(\psi_E - \psi_M)}{D\sqrt{\tau}}, \tag{1.20}$$

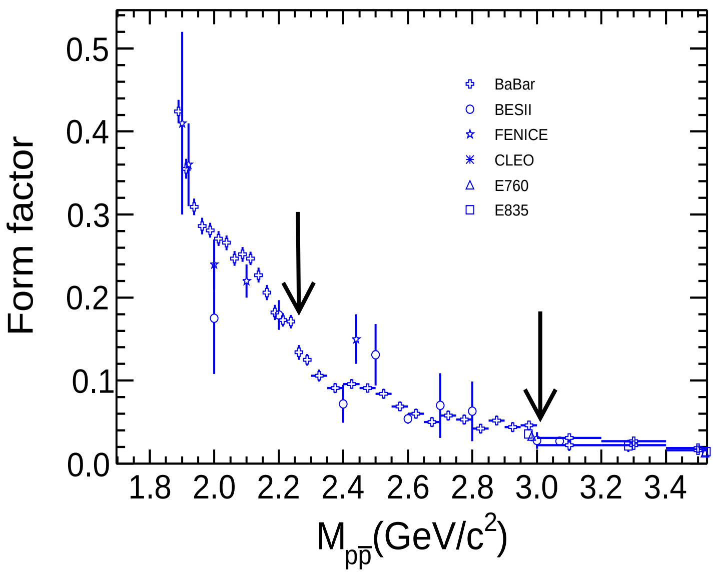

Figure 1.9 Effective FF of proton for the energy range 1.8 - 3.4 GeV.

with

$$D = |G_M(q^2)|^2(1+\cos^2\theta) + |G_E(q^2)|^2\frac{\sin^2\theta}{\tau}, \tag{1.21}$$

where ψ_E and ψ_M is the phase of the complex-value electric and magnetic FFs, respectively.

The other two components of the polarization, P_x and P_z, lie on the scattering plane and are different from zero only if the incoming electron beam has a non vanishing longitudinal polarization, P_e:

$$P_x = -P_e\frac{2\sin\theta Re(G_E(q^2)G_M^*(q^2)}{D\sqrt{\tau}}, \tag{1.22}$$

$$P_z = P_e\frac{2\cos\theta|G_M(q^2)|^2}{D\sqrt{\tau}}. \tag{1.23}$$

From the previous equations, we can find information on absolute values and phases can be extracted by measuring both the angular distributions and polarizations. However, there is no experiments in TL which has measured the phase difference of G_E and G_M yet.

In the SL experiments, the FFs provide the physical interpretation of the Fourier transforms of the spacial charge and magnetic structure of the proton, and the TL momentum transfer yields information about the frequency structure of the proton. For $q^2 > 0$, the "cloud" around the proton could have various kinds of resonance structure such as the ρ, ω and ϕ mesons. It would be of great interest to explore this region to see if this kind of structure is simple, *i.e.* one or two resonances with a more or less constant continuum, or whether more structure appears as the momentum transfer continues to larger negative values. Until now it has been assumed that analyticity holds in the case of FFs. That should allow to calculate their behaviors in the unphysical region by means of dispersion relations [35, 36] using the available data in both the TL and SL regions. In SL region, the $\mu_p G_E/G_M$ ratios have been measured at 16 Q^2 values in (0.5, 8.5) GeV^2 with the best precision to 1.7%, while the present precision of $|G_E/G_M|$ ratio in TL region exceeds 10%. Therefore, it is necessary to improve the measurement of $|G_E/G_M|$ ratio in TL region.

1.2.4 Nucleon FFs: Theory and Phenomenology

The FFs constitute a rigorous test for the phenomenological models which consist fundamental elements in QCD. At the high energies, where asymptotic freedom of gluons are functioning, FFs follow simple counting rules based and the perturbation QCD (pQCD) can predict the FFs well. The prediction of pQCD [37] shows $|G_M| \propto \mu_N/q^4$, yielding the relation

$$|G| = \frac{A}{s^2 ln^2(s/\Lambda^2)}, \tag{1.24}$$

where $\Lambda = 0.3$ GeV is the QCD scale parameter and A is a free parameter. The TL data are consistent with the $1/q^4$ expected asymptotic behavior at $q^2 > 4$ GeV^2. However, some particular behaviors are observed near the $p\bar{p}$ threshold, showing an almost uniform distribution which can not be explained by pQCD.

Phenomenological models which based on $Vector\ Meson\ Dominance$ where the external photon couples both to an intrinsic structure and to a meson cloud through the intermediate vector mesons (ρ, ω, ϕ) [38–40], have yield a very wide range of nucleon time-like form factors expectations. Such a model allows one to construct a very effective scheme of approximation by a description of the hadronic decay of the vector meson via $\gamma^* \to VM \to h\bar{h}$. If we expand the analysis to the unphysical region ($q^2 < 4M_N^2$), one can recognize that different channels can be opened with different energy threshold. In the energy interval $0 < q^2 < 4m_\pi^2$, there is no purely hadron production at all, while for increasing values of q^2 up to $q^2 < 4M_N^2$, one meets channels that contributes to the production of a virtual $N\bar{N}$ pair through the isovector ρ, ω and ϕ mesons. It contains many interesting information, particularly near the $N\bar{N}$ threshold. Furthermore, the opening of more production channels beyond the production threshold generates new overlapping cuts in the FFs. In the theoretical calculation, the combined data of SL and TL are analysed and fitted to the expectations. The meson-dominance FFs are generally comparable to the available experimental data within the uncertainties.

Another promising approach to the nucleon electromagnetic structure at low momentum transfer is the constituent quark models (CQMs) [41]. Constituent quarks are valence quarks for which the correlations for the description of hadrons by means of gluons and sea-quarks are put into effective quark masses of these valence quarks. It has already successfully applied to the pion FF in the whole kinematic range. The aim of the approach is to calculate as many quantities as possible in terms of quark degrees of freedom and to perform a direct evaluation of the SL and TL FFs.

In recent years, the chiral effective field theory has made contributions to the steep rise of the effective FFs for energies close to the $p\bar{p}$ threshold. By considering the interaction in the initial- or final $N\bar{N}$ state, the reaction $p\bar{p} \to e^+e^-$ and $e^+e^- \to p\bar{p}$ in the near-threshold region are analyzed [42]. The study is based on the one-photon approximation, but takes into account the effects of $p\bar{p}$ interaction based on the phenomenological $N\bar{N}$ meson-exchange modes. And then the amplitudes of $N\bar{N}$ is determined from partial wave analysis. And by including both $^3S_1$ and $^3D_1$ particle wave, the energy dependence of the experimental cross sections is described close to the threshold. The energy dependence of the $e^+e^- \to p\bar{p}$ cross section from experimental result is very well reproduced by this chiral effective field theory from threshold up to 100 MeVs, and by considering the renormalization factor 1.47, the $p\bar{p} \to e^+e^-$ cross sections near threshold are also well reproduced. In addition, the existing data on angular distributions are also well reproduced by this approach.

Another theory in non-perturbative region is the lattice QCD which has been applied to calculate the FFs of nucleon in recent year. In Ref. [43], lattice QCD calculations of nucleon electromagnetic form factors using pion masses $M_\pi = 149$ MeV is present. Compare with previous work on lattice work, the essential advance is calculation at the nearly physical pion mass, and the other advance is the removal of contamination due to excited states. The calculations of isovector nucleon observable are consistent with the results from experiment for the Sachs FFs, Dirac radius, Pauli radius, and magnetic moment up to $Q^2 = 0.5$ GeV^2.

1.2.5 The $N\bar{N}$ Production Threshold

The study of baryon anti-baryon production near the threshold provides many relevant insights in the reaction mechanism that governs the transition from the unphysical to the physical regions. The sizeable and sharp rising of the cross section close to the $p\bar{p}$ production shown in Fig. 1.9 has driven a lot of theoretical studies. According to this behavior it has been suggested:

- the $p\bar{p}$ final-state interaction (FSI) acting near the threshold [44]. The success of $p\bar{p}$ FSI effects in explaining the near-threshold enhancement in the $p\bar{p}$ mass spectrum of $J/\psi \to \gamma p\bar{p}$ suggests that the same mechanisms could be also responsible for the behaviour of the FFs. The reaction $e^+e^- \to p\bar{p}$ can involve a single partial wave, namely the coupled $^3S_1 -^3 D_1$ $p\bar{p}$ state. Close to the $p\bar{p}$ threshold, the reaction amplitude will be dominated by the $^3S_1$ component.

- a narrow meson resonance [20]. Many narrow resonances below threshold were predicted on the basis of a mostly attractive $N\bar{N}$ potential, as deduced by means of the meson exchange model of the NN potential and of the exchanged G parity. Besides, tails of $J^{PC} = 1^{--}$ below threshold have to be detected as large effects in the TL FFs.

- the correction on Coulomb enhancement factor and effective FF $|G_{\text{eff}}| = 1$ near threshold [45] [46]. In the standard theoretical calculation, $\mathcal{C} = \varepsilon \times \mathcal{R}$, where ε is the enhancement factor, responsible for the one-photon exchange $p\bar{p}$ final state interaction (FSI), $\varepsilon = \pi\alpha/\beta$. $\mathcal{R}$ is the resummation factor, responsible for the multi-photon exchange $p\bar{p}$ FSI, $\mathcal{R} = 1/(1 - e^{-\pi\alpha/\beta})$. The resummation factor is hold for point-like fermion pair. At threshold, the velocity β in Eq. 1.15 is canceled. Since $|G_E| = |G_M| = |G_{\text{eff}}|$ at threshold, Eq. 1.15 can be rewrote into:

$$\sigma = \frac{\pi^2\alpha^3}{2m_p^2}|G_{\text{eff}}|^2 = \sigma_{\text{point}}|G_{\text{eff}}|^2, \tag{1.25}$$

where $|G_{\text{eff}}|$ can quantitatively describe how the nucleon different from a point-like particle. σ_{point} is the cross section point-like particle, equals to 849 pb, which is surprisedly close to the BaBar result near threshold. Therefore, the effective form factor near threshold is found $|G(4m_p^2)| \sim 1$.

The cross sections of proton pair from threshold up to $\sqrt{s} = 1.905$ GeV is almost constant as observed by BaBar. By taking the Coulomb factor for point-like fermions, which has been applied for more than 30 years to get the proton FF, the proton FF shows an apparent steep decrease. It seems unlike to attach a physical meaning to the sharp decrease at threshold. To avoid this kind of ambiguity and interpret the almost constant cross sections, the gluon exchange is be account for in the Resummation factor, replacing $\mathcal{R}_{em}$ by $\mathcal{R}_S$. Assuming $\mathcal{R}_S = 1/(1-e^{-\pi\alpha_s/\beta})$, with α_s about 0.5, the flat proton pair cross section on a hundred MeV scale can be well reproduced.

According from the above explanations, the form factor $|G(4m_p^2)| \sim 1$ and applying the $\mathcal{R}_S$ could be a general feature for baryons. In the case of neutral baryons an interpretation of the non-vanishing cross section at threshold is suggested, based on quark electromagnetic interaction and taking into account the asymmetry between attractive and repulsive Coulomb factors. To settle these open questions, further measurement, such as the $\Lambda\bar{\Lambda}$, $\Lambda_c^+\bar{\Lambda}_c^-$ production cross section near threshold are needed.

1.3 The Structure of the Dissertation

In Chapter 2, the scheme of upgraded Beijing Electron Positron Collider (BEPCII) and Beijing Spectrometer detector (BESIII) is presented, as well as the BESIII Offline Software System (BOSS).

In Chapter 3, the analysis of proton form factor measurement through process $e^+e^- \to p\bar{p}$ at 12 center-of-mass energies is presented. Moreover, the ratio of electric to magnetic FFs, $|G_E/G_M|$ are extracted by different methods.

In Chapter 5, process $e^+e^- \to \Lambda\overline{\Lambda}$ is studied at the production threshold of $\Lambda\overline{\Lambda}$, and the cross section is measured by reconstructing both the charge decay channels and neutral $\overline{\Lambda}$ decay.

In Chapter 5, process $J/\psi \to p\bar{p}a_0(980)$, $a_0(980) \to \pi^0\eta$ is studied and the product branching fraction is measured for the first time, which provides experimental results for J/ψ decays to four body processes in ChPT prediction.

In Chapter 6, a summary is presented and the prospects of future FFs measurements at BESIII are discussed.

In the Appendix, some related work on BESIII are presented, such as the preliminary study of $e^+e^- \to \Lambda_c^+\overline{\Lambda}_c^-$ near production threshold, and the prepare study for $e^+e^- \to n\bar{n}$.

Bibliography

[1] M. Ablikim *et al.*, (BESIII Collaboration), Observation of a Charged Charmoniumlike Structure in the $e^+e^- \to \pi^+\pi^- J/\psi$ at $\sqrt{s} = 4.26$ GeV. Phys. Rev. Lett. **110**, 252001 (2013).

[2] Z. Q. Liu *et al.*, (Belle Collaboration), Study of $e^+e^- \to \pi^+\pi^- J/\psi$ and Observation of a Charged Charmoniumlike State at Belle. Phys. Rev. Lett. **110**, 252002 (2013).

[3] J. S. Poucher *et al.*, High-Energy Single-Arm Inelastic e-p and e-d Scattering at 6-Degrees and 10-Degrees. Phy. Rev. Lett. **32**, 118 (1974).

[4] G. Aad *et al.* (ATLAS Collaboration), Observation of a new particle in the search for the Standard Model Higgs boson with the ATLAS detector at the LHC. Phys. Lett. B **716**, 1 (2012).

[5] S. Charrchyan *et al.* (CMS Collaboration), Observation of a new boson at a mass of 125 GeV with the CMS experiment at the LHC. Phys. Lett. B **716**, 30 (2012).

[6] J. Gasser and H. Leutwyler, Chiral Perturbation Theory: Expansions in the Mass of the Strong Quark. Nucl. Phys. B **250**, 465 (1985).

[7] G. Ecker, Chiral perturbation theory. Prog. Part. Nucl. Phys. **35**, 1 (1995).

[8] C. b. Li, E. Oset and M. J. Vicente Vacas, Light scalar mesons in $J/\psi \to N\bar{N}\ meson\ meson$ decays in a chiral unitary approach. Phys. Rev. C **69**, 015201 (2004).

[9] R. W. McAllister and R. Hofstadter, Elastic Scattering of 188 MeV Electrons from the Proton and the Alpha Particle. Phys. Rev. , 1956, 102:851.

[10] M. N. Rosenbluth, High Energy Elastic Scattering of Electrons on Protons. Phys. Rev. **79**, 615 (1950).

[11] L Andlvahls *et al.*, Measurements of the electric and magnetic form-factors of the proton from $Q^2 = 1.75$ to 8.83 GeV/c^2. Phys. Rev. D **50**, 5491 (1994).

[12] I. A. Qattan *et al.*, Precision Rosenbluth measurement of the proton elastic form factors. Phys. Rev. Lett. **94**, 142301 (2005).

[13] V. Punjabi *et al.*, Proton elastic form-factor ratios to $Q^2 = 3.5$ GeV^2 by polarization transfer. Phys. Rev. C **71**, 069902 (2005).

[14] A. J. R. Puckett *et al.*, Final Analysis of Proton Form Factor Ratio Data at $Q^2 = 4.0$, 4.8 and 5.6 GeV^2.

[15] N. Cabibbo and R. Gatto, Electron Positron Colliding Beam Experiments. Phys. Rev. **124**, 1577 (1961).

[16] A. D. Sakharov, Interaction of an Electron and Positron in Pair Production. Zh. Eksp. Teor. Fiz. **18**, 631 (1948).

[17] M. Castellano *et al.*, The reaction $e^+e^- \to p\bar{p}$ at a total energy of 2.1 GeV. Nuovo Cim. A**14**, 1 (1973).

[18] B. Delcout *et al.*, (DM1 Collaboration), Study of the Reaction $e^+e^- \to p\bar{p}$ in the Total Energy Range 1925 MeV - 2181 MeV. Phys. Lett. B **86**, 395 (1979).

[19] D. Bisello *et al.*, (DM2 Collaboration), A Measurement of $e^+e^- \to p\bar{p}$ for 1975 MeV $\leq \sqrt{s} \leq 2250$ MeV. Nucl. Phys. B **224**, 379 (1983).

[20] A. Antonelli *et al.*, (FENICE Collaboration), The first measurement of the neutron electromagnetic form-factors in the timelike region. Nucl. Phys. B **517**, 3 (1998).

[21] M. Ablikim *et al.* (BES Collaboration), Measurement of the cross section for $e^+e^- \to p\bar{p}$ at center-of-mass energies from 2.0 GeV to 3.07 GeV. Phys. Lett. B **630**, 14 (2005).

[22] T. K. Pedlar *et al.* (CLEO Collaboration), Precision measurements of the timelike electromagnetic form-factors of pion, kaon and proton. Phys. Rev. Lett. **95**, 261803 (2005).

[23] D. L. Hartill *et al.* Anti-proton-proton annihilation into electron-positron pairs and gamma-ray pairs. Phys. Rev. **184**, 1415 (1969).

[24] G. Bassompierre *et al.*, Measurement of the Branching Ratio $\Gamma(\bar{p}p \to e^+e^-)/\Gamma(\bar{p}p \to Total)$ in antiProton-Proton Annihilation at Rest. Phys. Lett. B **64**, 475 (1976).

[25] G. Bardin *et al.*, Determination of the electric and magnetic form-factors of the proton in the timelike region. Nucl. Phys. B **411**, 3 (1994).

[26] T. A. Armstrong *et al.*(E760 Collaboration), Measurement of the proton electromagnetic form-factors in the timelike region at 8.9 GeV^2 - 13 GeV^2. Phys. Rev. Lett. **70**, 1212 (1993).

[27] M. Ambrogiani *et al.* (E835 Collaboration), Measurement of the magnetic form-factor of the proton in the timelike region at large momentum transfer. Phys. Rev. D **60**, 032002 (1999).

[28] M. Andreotti *et al.* (E835 Collaboration), Measureument of the magnetic form-factor of the proton for timelike momentum transfers. Phys. Lett. B **559**, 20 (2003).

[29] V. P. Druzhinin, S. I. Eidelman, S. I. Serednyakov and E. P. Solodov, Hadron Production via e^+e^- Collisions with Initial State Raidation. Rev. Mod. Phys. **83**, 1545 (2011).

[30] B. Aubert *et al.* (BaBar Collaboration), A Study of $e^+e^- \to p\bar{p}$ using initial state radiation with BABAR. Phys. Rev. D **73**, 012005 (2006).

[31] J. P. Lees *et al.* (BaBar Collaboration), Study of $e^+e^- \to p\bar{p}$ via initial-state radiation at BABAR. Phys. Rev. D **87**, no. 9, 092005 (2013).

[32] J. P. Lees *et al.* (BaBar Collaboration), Measurement of the $e^+e^- \to p\bar{p}$ cross section in the energy range from 3.0 to 6.5 GeV. Phys. Rev. D **88**, no. 7, 072009 (2013).

[33] J. L. Rosner, Effects of S-wave thresholds. Phys. Rev. D **74**, 076006 (2006).

[34] A. Z. Dubnickova, S. Dubnicka and M. P. Rekalo, Investigation of the nucleon electromagnetic structure by polarization effects in $e^+e^- \to N\bar{N}$ processes. Nuovo Cim. A **109**, 241 (1996).

[35] H. Pfister, Extrapolation of the proton form-factor into the timelike region. Nucl. Phys. B **20**, 320 (1970).

[36] H. W. Hammer, U. G. Meissner and D. Drechsel, Dispersion theoretical analysis of the nucleon electromagnetic form-factors: Inclusion of timelike data. Phys. Lett. B **385**, 343 (1996).

[37] S. J. Brodsky and G. R. Farrar, Sacling Laws for Large Momentum Transfer Processes. Phys. Rev. D **11**, 1309 (1975).

[38] R. Bijker and F. Iachello, Re-analysis of the nucleon space and time-like electromagnetic form-factors in a two-component model. Phys. Rev. C **69**, 068201 (2004).

[39] P. Masjuan, E. Ruiz Arriola and W. Broniowski, Meson dominance of hadron form factors and large-Nc phenomenology. Phys. Rev. D **87**, 014005 (2013).

[40] D. Scildknecht, Vector meson dominance. Acta Phys. Polon. B **37**, 595 (2006).

[41] T. Melde, K. Berger, L. Canton, W. Plessas and R. F. Wagenbrunn, Electromagnetic nucleon form factors in instant and point form. Phys. Rev. D **76**, 074020 (2007).

[42] J. Haidenbauer, X.-W. Kang and U.-G. Meiβner, The electromagnetic form factors of the proton in the timelike region. Nucl. Phys. A **929**, 102 (2014).

[43] J. R. Green, J. W. Negele, A. V. Pochinsky, S. N. Syritsyn, M. Engelhardt and S. Krieg, Nucleon electromagnetic form factors from lattice QCD using a nearly physical pion mass. Phys. Rev. D **90**, no. 7, 074507 (2014).

[44] J. Haidenbauer, H.-W. Hammer, U. G. Meissner and A. Sibirtsev, On the strong energy dependence of the $e^+e^- \to p\bar{p}$ amplitude near thresold. Phys. Lett. B **643**, 29 (2006).

[45] R. Baldini, S. Pacetti, A. Zallo and A. Zichichi, Unexpected feature of $e^+e^- \to p\bar{p}$ and $e^+e^- \to \Lambda\overline{\Lambda}$ cross sections near threshold. Eur. Phys. J. A **39**, 315 (2009).

[46] R. Baldini *et al.*, Neutral and charged baryon pair production at threshold unexpected results, internal note.

Chapter 2

BEPCII and BESIII

2.1 BEPCII

BEPCII (Beijing Electron Positron Collider) is a double-ring e^+e^- factory-like collider, working at the beam energy range from 1.0 GeV to 2.3 GeV which covers the τ-charm energy region, and reaches the peaking luminosity of $0.85 \times 10^{33}\mathrm{cm}^{-2}\mathrm{s}^{-1}$ at the optimized beam energy 1.89 GeV. It consists of a linac, two transport lines, two storage rings and one detector. The layout of BEPCII is shown in Fig. 2.1. It can used for two purposes, the first one is providing beams for high energy physics experiments, the second is for synchrotron radiation (SR) users. The design parameters for collider beams is shown in Table 2.1. The luminosity of e^+e^- collision can be expressed as

$$L(\mathrm{cm}^{-2}\mathrm{s}^{-1}) = 2.17 \times 10^{34}(1+r)\xi_y \frac{E(\mathrm{GeV})k_b I_b(\mathrm{A})}{\beta_y^*(\mathrm{cm})}, \tag{2.1}$$

where $r = \sigma_y/\sigma_x$, E is the beam energy, ξ_y is the beam-beam parameter, β_y^* is the vertical β function at the IP, k_b is the bunch number and I_b is the current of each bunch. An effective way to improve the luminosity is by adding more bunch number and reduce the β function at the IP at a certain energy.

BEPCII, started in early 2004, was successfully completed in 2008 with excellent quality, and the first test run was taken in 2008. BEPCII starts to take physical data in 2009. Since then, the collider has operated for high energy physics experiments as well as for synchrotron radiation application. The information of the high energy physics

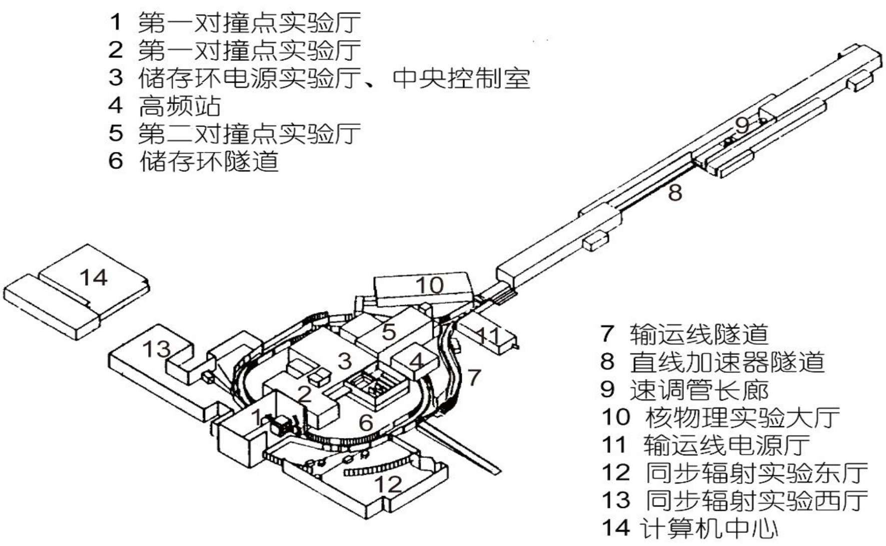

Figure 2.1 Layout of BEPCII

data taken till July 2014 is shown in Table. 2.2.

2.2 BESIII

The cylindrical BESIII detector has an effective geometrical acceptance of 93% of 4π and divides into a barrel section and two endcaps. Figure 2.2 shows a schematic view of BESIII detector, which from the inside out consists of a main drift chamber (MDC), a time-of-flight system (TOF), an electromagnetic calorimeter (EMC), a superconducting solenoid magnet (SSM) and a muon system (MUC)

a. MDC. Since the purpose of BESIII is for precise measurement of particle production and decay in τ-charm, the detection of charged particles is of the most important. MDC, as one of the most important sub-detectors, should provide the momentum and path of the charged particle from interaction point, provide energy loss measurement dE/dx, can cover most solid angle for large acceptance, provide high reconstruction efficiency for low-momentum charged particle, and provide the first level trigger condition for charged particles. To fulfill such requirements, the MDC consists of 43 cylindrical layers of drift cells, of which 8 stereo wire layers in the inner chamber and 16

Table 2.1 Main design parameters of BEPCII collision rings.

Parameters	Value
Circumference	235.53 m
Beam energy range	1.0-2.3 GeV
Optimized beam energy region	1.89 GeV
Bunch current /No.	9.8 mA / 93
Bunch size ($\sigma_x/\sigma_y/\sigma_z$)	380 μm/ 5.7 μm/13.5 mm
$beta$ function at IP (x/y)	1.0/0.015 m
Beam current	0.93 A
Design luminosity	1×10^{33}cm^{-2}s^{-1} @1.89 GeV
Beam lifetime	2.7 hrs.
Injection rate (e^+, e^-)	50 / 200 mA/min
Energy spread	5.16×10^{-4}
Crossing angle	11 mrad

Table 2.2 Summary of the data taken in BEPCII till July 2014.

Taking data	Total Num/Luminosity	Taking time
J/ψ	225+1086 M	2009+2012
ψ(2S)	106+350 M	2009+2012
ψ(3770)	2916 pb^{-1}	2010$\sim$2011
τ mass scan	24 pb^{-1}	2011
Y(4260)/Y(4230)/Y(4360)/scan	806/1054/523/488 pb^{-1}	2012$\sim$2013
4600/4470/4530/4575/4420	506/100/100/42/993 pb^{-1}	2014
J/ψ lineshape scan	100 pb^{-1}	2012
R scan at low energy	12 pb^{-1}	2012
R scan at high energy	795 pb^{-1}	2013$\sim$2014

stereo layers and 19 axial layers in the outer chamber. The stereo layers can provide position measurement at z-direction. The axial layers can provide information of track finding and is convenience to locate at the stairs. The acceptance of MDC covers the polar angle $|\cos\theta| < 0.93$. There are totally 6794 drift cells, made of 1 sense wire (gold-plated tungsten wire, ϕ=110 μm) inside and 8 field wire (gold-plated aluminum wires, ϕ=25 μm) outside. In a magnetic field of 1 Tesla, the single-wire resolution is better than 130 μm in the R-ϕ plane, and 2 mm at z-direction, which yields a momentum resolution of 0.5% at 1 GeV/c for charged particle. A helium-based gas mixture (He/C_3H_8=60/40) is used as the working gas. Due to its low atomic number Z, such working gas can reduce the effect of the multiple scattering. The dE/dx resolution from

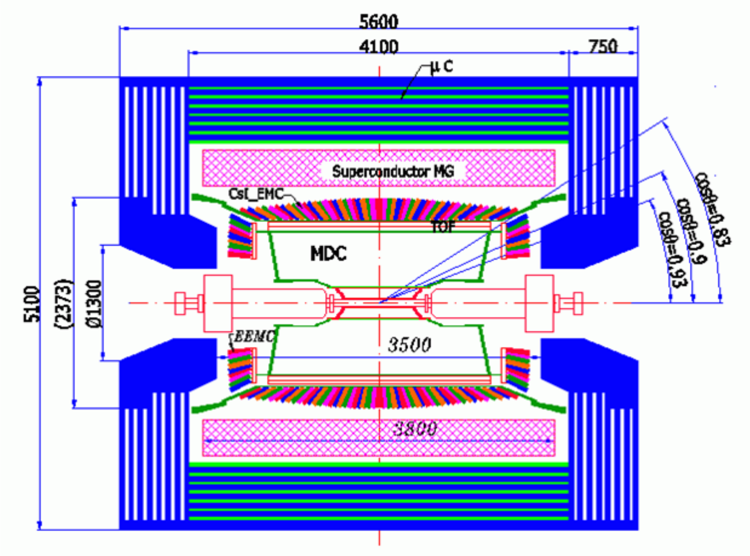

Figure 2.2 Layout of BEPCII

a truncated mean Laudau distribution is better than 6%. Under the optimized operating voltage, 2200 V, the position resolution is better than 110 μm, a 3σ $\pi/$K separation is possible up to 700 MeV/c, and the transverse momentum resolution is 0.46% at 1 GeV.

b. TOF. The TOF detector is placed between the MDC and the EMC. It measures the flight time of charged particles in MDC to identify the particle-type. It also provides the first level trigger condition and helps reject comic-ray background. The TOF consists of two layer barrels and one layer endcap and the structure is shown in Fig. 2.3. The barrel TOF is made of plastic scintillators BC408 with the acceptance of $|\cos\theta| < 0.83$, and the fine mesh photomultiplier (PMT) tubes directly attached to the two end faces of the scintillators bars. No light guides connecting the PMT and scintillators bars in the TOF is the main factor that contributes to the time resolution improvement. Each layer has 88 bars that are 5 cm thick. The time resolution is $100 \sim 110$ pb for single layer, and $80 \sim 90$ for double layers which allows 3σ $\pi/$K separation to reach 900 MeV/c at the polar angle to be 90°, while the polar angle of charged particle is less than 90°, the resolution can be better since the hit position is closer to PMT. The endcap TOF is made of 48 fan-shaped plastic scintillators BC404 with the acceptance of $0.85 < \cos\theta < 0.95$. The time resolution of endcap TOF is $110 \sim 136$ ps. The reason for a worse time resolution in endcap is the precision of track extrapolation in endcap is worse than in barrel since the number of hit layers is less in MDC. There are energy loss when a particle passing TOF, which will influence the shower energy resolution of EMC. To overcome this problem, the dE/dx measurement is obtained for both charged and neutral particles and an algorithm is developed to add such energy loss in EMC.

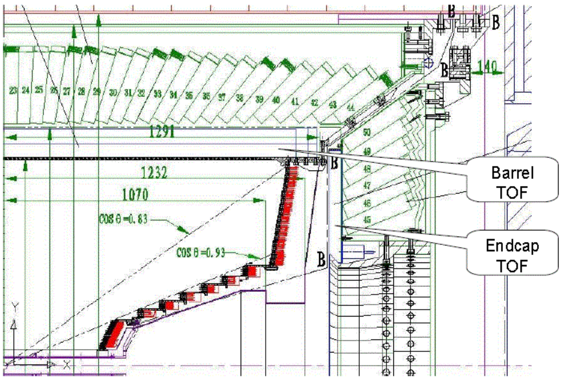

Figure 2.3 Schematic structure of TOF at BESIII.

c. EMC. The Electro-Magnetic Calorimeter plays an important role in the BESIII detector, whose primary function is to measure the energies and positions of electrons and photons precisely. Since there are sizable photons with energy below 500 MeV, the absorption type inorganic scintillation crystals is selected which can provide the best energy resolution at low energy region. The EMC consists of 6240 CsI(Tl) whose radiation length X_0 is 1.86 cm, in a cylindrical structure and two end-caps as shown in Fig. 2.4. To achieve the energy resolution $\sigma_E = 2.5\%$ at 1 GeV, the length of the crystals is 28 cm ($15X_0$). The position resolution is determined from the cross-section of crystals and number of energy deposited crystals of one cluster, and the optimize size of one crystal is $5 \times 5 \sim 6.5 \times 6.5$ cm^2 which gives the position resolution σ_{xy}=6 mm at 1 GeV. In the barrel, there are totally 44 rings of crystals along the z direction, each with 120 crystals. The acceptance is $|\cos\theta| < 0.83$. All crystals except two rings at the center point to z=$\pm$50 mm with a slight tilt angle of 1.5° in the ϕ direction to avoid particles passing the gap between crystals directly. In each endcap, there are 6 rings and all crystals point to z=$\pm$ 100 mm with a tilt of $1.5°$ in the ϕ direction. The acceptance is $0.85 < |\cos\theta| < 0.93$. The EMC can also provide deposition time information which is the time difference between the seed crystals and surrounded crystals. The time difference for an event is $\sigma_{\delta t}$ $\simeq$150 ns, therefore, a requirement on $\pm 4\sigma_{\delta t}$ can be applied to significantly suppress beam-associated background. The electronics noise for each crystals is less than 200 keV.

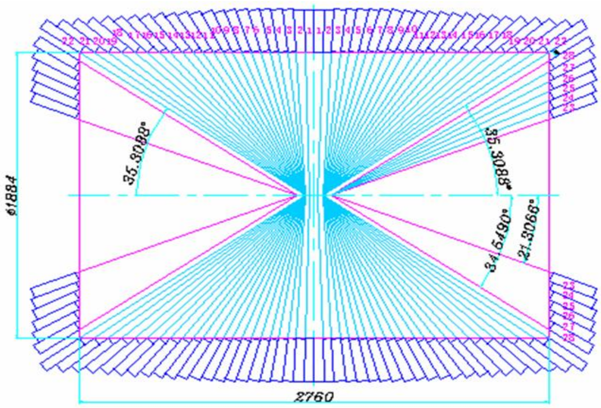

Figure 2.4 Schematic structure of crystals ranged in EMC.

d. SSM. The superconducting solenoid magnet is to provide a stable-magnetic field. The momentum of charged particles should be measured by the radius of deflection in MDC. The magnetic field value is decided to be 1 Tesla at BESIII by considering the particle can be deflected as more as possible and they can reach the outmost layer of MDC. The unevenness of the magnetic field is less than 5% and the precision of magnetic field is better than 0.3%. The SSM consists of yoke and superconducting coil, where the yoke can function as the magnetic flux loop, the absorber of muon system and the support of sub-detectors of BESIII. The diameter of the coil is 3 m and length is 3.5 m. The operation current is 3368 A. This is the first superconducting magnet of this type built in China.

e. MUC. The muon system is designed to distinguish muons from other charged particles, especially pions. It is mde of Resistive Plate Counter (RPC) sandwiched by iron absorbers. The drawing of a RPC superlayer module is shown in Fig. 2.5. A superlayer consists of two layer RPC and one layer readout copper strip which can provide one dimension readout and the strip orientates alternate in different layer to acquire two dimension position readout. In the barrel, there are 9 layers iron absorbers and 9 layers of RPC. The inner acceptance is $|\cos\theta| < 0.75$ and outer is $|\cos\theta| < 0.59$. In the endcap, there are 8 layers of RPC due to the limitation of space, and 9 layers iron absorbers since the there is no superconducting coil in endcap. The acceptance is $|\cos\theta| < 0.89$. The working gas is a mixture of Ar/F134A/C4H10 with the ratio 50:42:8. The working voltage is (7200 ± 200)V. The spatial resolution for one layer RPC is 1.2 cm. The detection efficiency for muons with momentum larger than 0.4 GeV/c is 95%. The contamination of pions is 10% in momentum region $0.4 \sim 0.6$ GeV/c, and less than 4% with momentum larger than 0.9 GeV.

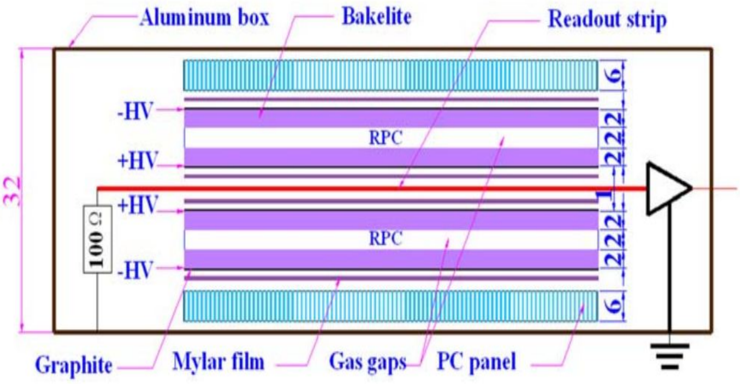

Figure 2.5 The cutaway drawing of a RPC superlayer module.

2.3 Trigger and BESIII Offline Software

The trigger system is required to select interesting physics events with a high efficiency and suppress backgrounds to a level that the data acquisition (DAQ) system can sustain which is 4000 Hz. The main background is the huge beam associated background and the radiative Bhabha-scattering, while the Bhabha events should not be completely eliminate for the sake of calibration and luminosity measurement. At the peak luminosity $L = 1 \times 10^{33}$ cm^{-2}s^{-1} at BESIII, the expected events rate of J/ψ and

$\psi(3686)$ is 2000 Hz and 600 Hz, respectively. Taking the acceptance of detector into consideration ($|\cos\theta| < 0.93$), events rate of Bhabha is 800 Hz. The events rate of cosmic rays is 1500 Hz.

A two-level scheme has been adopted for the BESIII trigger system: a level-1 (L1) hardware trigger and a level-2 software event filter. The L1 trigger is finished in 6.4 μs, which taking combined information from the EMC, MDC and TOF to select the interaction of interests for readout. The efficiencies of L1 trigger for most signals with topologies containing multiple charged tracks and photons are close to 100%. The rejection power for beam backgrounds, which is estimated to have a maximum level of 40 MHz, is about 5×10^{-5}, resulting in a background trigger rate of below 2000 Hz. The trigger rate for cosmic-ray background is about 90 Hz. The event filter is used to further reduce the data rate, the online event filtering is also called L3 trigger. The BESIII event filter algorithms are designed to suppress the background rate by about one half from 2000 Hz, and the data rate of less than 3000 Hz is written to tape.

The DAQ system of BESIII can be roughly divided into two parts: the readout subsystem whose primary duty is to read the event data segments from the Front-End Electronics (FEE) modules and send them to readout PCs, and the online system which is in charge of collecting data, building events and data storage. The readout subsystem sends data to and receives commands from the readout PCs of the online system.

The BESIII Offline Software System (BOSS) is developed on the operating system of Scientific Linux CERN (SLC), using C++ language and GAUDI framework. uses the C++ language and object-oriented techniques and runs primarily on the Scientific Linux CERN (SLC) operating system. The entire data processing and physics analysis software system consists of five functional parts: framework, simulation, reconstruction, calibration, and analysis tools.

The signal and background Monte Carlo (MC) samples are used to optimize the event selection criteria, estimate the background contamination and evaluate the selection efficiencies. The MC samples are generated using a Geant4-based simulation software package BESIII Object Oriented Simulation Tool (BOOST), which includes the description of geometry and material, the detector response and the digitization model, as well as a database for the detector running conditions and performances.

Chapter 3

Measurement of the Proton Form Factor by Studying $e^+e^- \to p\bar{p}$ at BESIII

At present, the knowledge of the electromagnetic FFs of nucleon in the TL region remains widely mysteries, which has been explained detailed in Sec. 1.2. To receive a significant progress in our understanding of TL nucleon FFs, more experimental program is required to obtain the precision results of FFs, and obtain statistically significant results for the electromagnetic FF ratio.

In this chapter, we present an investigation of the process $e^+e^- \to p\bar{p}$ based on data samples collected with the Beijing Spectrometer III (BESIII) at the Beijing Electron Positron Collider II (BEPCII) at 14 c.m. energies ($\sqrt{s}$). Information of these data sets are shown in Table 4.1. In the analysis, the three sub-samples with close c.m. energies, $\sqrt{s}$=3542.4, 3553.8 and 3561.1 MeV, is combined to give one result. The averaged c.m. energy of the three sub-samples is calculated by weighting their luminosity values, to be 3550.7 MeV. The Born cross section in these energy points are measured and the corresponding effective FFs are determined. The ratio of electric to magnetic FFs, $|G_E/G_M|$, and $|G_M|$ are measured at those c.m. energies where the statistics are large enough.

In this analysis, the generator software package Conexc [4] is used to simulate the signal MC samples $e^+e^- \to p\bar{p}$, and calculate the corresponding correction factors

Table 3.1 The integral luminosity of the analysed data sets.

$\sqrt{s}$ (MeV)	Taking time	Run No.	Lumi.(pb^{-1})
2232.4	12.06.08-12.06.16	[28624, 28648]	2.631 [1]
2400.0	12.06.08-12.06.16	[28577, 28616]	3.415 [1]
2800.0	12.06.08-12.06.16	[28553, 28575]	3.751 [1]
3050.0	12.05.28	[28312, 28346]	14.895 [1]
3060.0	12.05.28-12.05.30	[28347, 28381]	15.056 [1]
3080.0	12.05.23-1205.24, 12.04.08	[27147, 27233]&[28241, 28266]	30.730
3400.0	12.06.08-12.06.16	[28543, 28548]	1.729 [1]
3500.0	13.06.05-13.06.06	[33725, 33733]	3.613
3542.4	11.12.21-11.12.31, 13.06.05-13.06.06	[24983, 25015]&[33734, 33743]	8.685 [2]
3553.8	11.12.21-11.12.31	[25016, 25094]	5.596 [2]
3561.1	11.12.21-11.12.31	[25100, 25141]	3.873 [2]
3600.2	11.12.21-11.12.31	[25143, 25243]	9.553 [2]
3650.0	09.05.26-09.06.03, 13.06.05-13.06.06	[9613, 9779]&[33747, 33758]	48.823 [3]
3671.0	13.06.05-13.06.06	[33759, 33764]	4.586

for higher order process with one radiative photon in the final states. Another generator Phokhara [5] serves as a cross check of the radiative correction factors. At each c.m. energy, a large signal MC sample contributing 0.15% statistical uncertainty on detection efficiency is generated. The MC samples of QED background processes $e^+e^- \to l^+l^-$ (l = e, μ) and $e^+e^- \to \gamma\gamma$ are generated with the generator Babayaga [6]. The other background MC samples for the processes with the hadronic final states $e^+e^- \to h^+h^-$ (h = π, K), $e^+e^- \to p\bar{p}\pi^0$, $e^+e^- \to p\bar{p}\pi^0\pi^0$ and $e^+e^- \to \Lambda\bar{\Lambda}$ are generated with uniform phase space distributions.

3.1 Analysis Strategy

3.1.1 Event Selection

The charged tracks are reconstructed with the hits information from the MDC. A good charged track must be within the MDC coverage, $|\cos\theta| < 0.93$, and is required to pass within 1 cm of the e^+e^- interaction point (IP) in the plane perpendicular to the beam and within ± 10 cm in the direction along the beam. The combined information of dE/dx and TOF is used to calculate the particle identification (PID) probabilities of a pion, kaon or proton hypothesis, respectively, and the particle type with the highest probability is assigned to the track. In this analysis, exactly two good charged tracks, one proton and one antiproton, are required.

To suppress Bhabha background events, the ratio E/p of each proton candidate is required to be smaller than 0.5, where E and p are the energy deposited in the EM-C and the momentum measured in the MDC, respectively. For the samples with c.m. energy $\sqrt{s} > 2400.0$ MeV, the proton is further required to satisfy $\cos\theta < 0.8$ to suppress Bhabha background. The cosmic ray background is rejected by requiring $|T_{trk1} - T_{trk2}|$ <4 ns, where T_{trk1} and T_{trk2} are the measured time of flight in the TOF detector for the two tracks.

After performing the above selection criteria, the distributions of opening angle between proton and antiproton, $\theta_{p\bar{p}}$, at c.m. energies $\sqrt{s} =$ 2232.4 and 3080.0 MeV are shown in Fig. B.4. Good agreement between data and MC samples is observed, and a better resolution is achieved with increasing c.m. energy due to the smaller effects on the small angle multiple scattering. A c.m. energy dependent requirement, $i.e.$, $\theta_{p\bar{p}} > 178^\circ$ at $\sqrt{s} \leq 2400.0$ MeV, while $\theta_{p\bar{p}} > 179^\circ$ at $\sqrt{s} > 2400.0$ MeV, is further applied.

Finally, a momentum window cut is applied for both proton antiproton tracks. In the center-of-mass system, the momentum of each track can be fitted by a simple. Table 3.3 summarizes the expected momentum calculated by energy conservation in the center-of-mass, mean momentum and resolution from fitting of MC. Resolution of momentum is in dependence of the c.m. energy. The relation graph is shown in Fig. 3.2, from which we can determine that σ_p(MeV)=0.9009$\times E^2_{cm}$(GeV). Figure 3.3

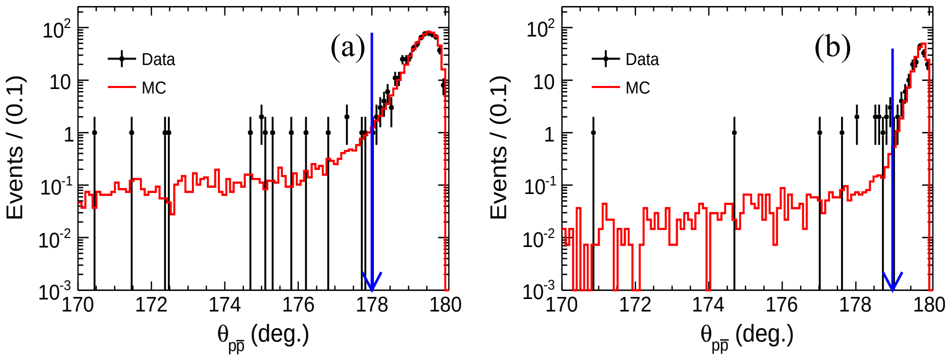

Figure 3.1 Opening angle distributions between proton and antiproton at the c.m. energies of (a) 2232.4 MeV, and (b) 3080.0 MeV.

shows the distribution of the momentum of proton or antiproton at c.m. energies $\sqrt{s} = 2232.4$ and 3080.0 MeV. A momentum window of 5 times the momentum resolution, $|p_{mea} - p_{exp}| < 5\sigma_p$, is applied to extract the signals, where p_{mea} and p_{exp} are the measured and expected momentum of the proton or antiproton in the c.m. system, respectively, and σ_p is the corresponding resolution.

Table 3.2 The expected momentum P_{exp} calculated by energy conservation in the center-of-mass, mean momentum p_{mea} and resolution σ_p from fitting of MC.

$\sqrt{s}$ (MeV)	P_{exp}(GeV)	P_{mea}(GeV)	σ_p(MeV)
2232.4	0.605	0.605	4.2
2400.0	0.748	0.748	5.0
2800.0	1.039	1.039	6.9
3050.0	1.202	1.203	8.4
3060.0	1.209	1.209	8.4
3080.0	1.223	1.222	8.5
3400.0	1.418	1.418	10.2
3500.0	1.477	1.478	11.1
3550.7	1.507	1.507	11.5
3600.0	1.536	1.537	11.8
3650.0	1.565	1.566	11.9
3671.0	1.578	1.579	12.5

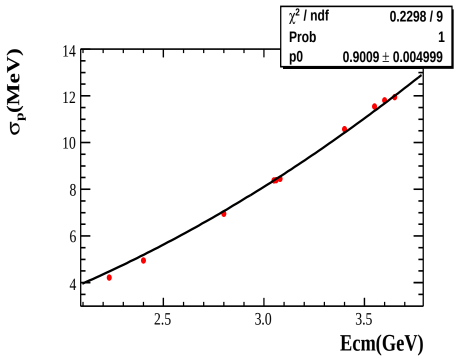

Figure 3.2 Dependence of resolution of momentum with $\sqrt{s}$.

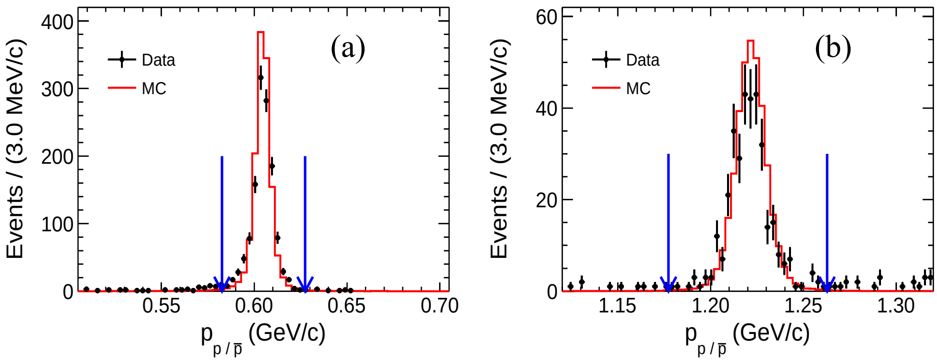

Figure 3.3 Momentum distribution of the proton or antiproton at the c.m. energies (a) 2232.4 MeV, and (b) 3080.0 MeV, two entries per event.

3.1.2 Background Analysis

The potential background contamination can be classified into two categories, the beam associated background and the physical background.

The beam associated background includes interactions between the beam and the beam pipe, beam and residual gas, and the Touschek effect [7]. The dedicated data samples, collected with BESIII detector at $\sqrt{s} = 2400.0$ and 3400.0 MeV, but with the separated beam condition, are used to study the beam associated background. Since the two beams do not interact with each other, all of the observed events are beam associated background, and can be used to evaluate the beam associated background at different c.m. energies by normalizing the data-taking time and efficiencies. With the same selection criteria, no events survived for the separated beam data samples, and the beam associated background at all c.m. energy points is negligible.

The physical background may come from the processes with two-body in final states, *e.g.* Bhabha or di-muon events, where leptons are misidentified as protons or antiprotons, or processes with multi-body final states including $p\bar{p}$, *e.g.* $e^+e^- \to p\bar{p}\pi^0(\pi^0)$. The contamination from physical background is evaluated by MC samples, and are listed in Table 5.1 for $\sqrt{s} = 2232.4$ and 3080.0 MeV, respectively, where N^{MC}_{gen} is the number of generated MC events, N^{MC}_{sur} is the number of events survived after the selection criteria, σ is the production cross section in e^+e^- annihilation process, which is from the Babayaga generator for Bhabha, di-muon, and di-photon processes, and from the previous experimental results for others processes [8, 9] $N^{MC}_{uplimit}$ and N^{MC}_{nor} are the estimated upper limit at the 90% confidence level (C.L.) and the normalized number of background events. The background contamination is found to be negligible.

Table 3.3 Physical background processes estimated from the MC samples at $\sqrt{s} = 2232.4$ and 3080.0 MeV.

	$\sqrt{s} = 2232.4$ MeV (2.63 pb^{-1})				$\sqrt{s} = 3080.0$ MeV (30.73 pb^{-1})			
Bkg.	N^{MC}_{gen} ($\times 10^6$)	N^{MC}_{sur}	σ (nb)	N^{MC}_{nor}	N^{MC}_{gen} ($\times 10^6$)	N^{MC}_{sur}	σ (nb)	N^{MC}_{nor}
e^+e^-	9.6	0	1435.01	0	39.9	1	756.86	1
$\mu^+\mu^-$	0.7	0	17.41	0	1.5	0	8.45	0
$\gamma\gamma$	1.9	0	70.44	0	4.5	0	37.	0
$\pi^+\pi^-$	0.1	0	0.17	0	0.1	0	< 0.11	0
K^+K^-	0.1	0	0.14	0	0.1	0	0.093	0
$p\bar{p}\pi^0$	0.1	0	< 0.1	0	0.1	0	< 0.1	0
$p\bar{p}\pi^0\pi^0$	0.1	0	< 0.1	0	0.1	0	< 0.1	0
$\Lambda\bar{\Lambda}$	0.1	0	< 0.4	0	0.1	0	0.002	0

The ratio of $p\bar{p}$ invariant mass and the c.m. energy, $M_{p\bar{p}}/\sqrt{s}$, from data and MC has been compared and is shown in Fig. 3.4 at different c.m. energies. There is good agreements between data and MC simulations. The signal yields are extracted by counting the number of events and are listed in Table 3.4, where the quoted uncertainties are statistical only.

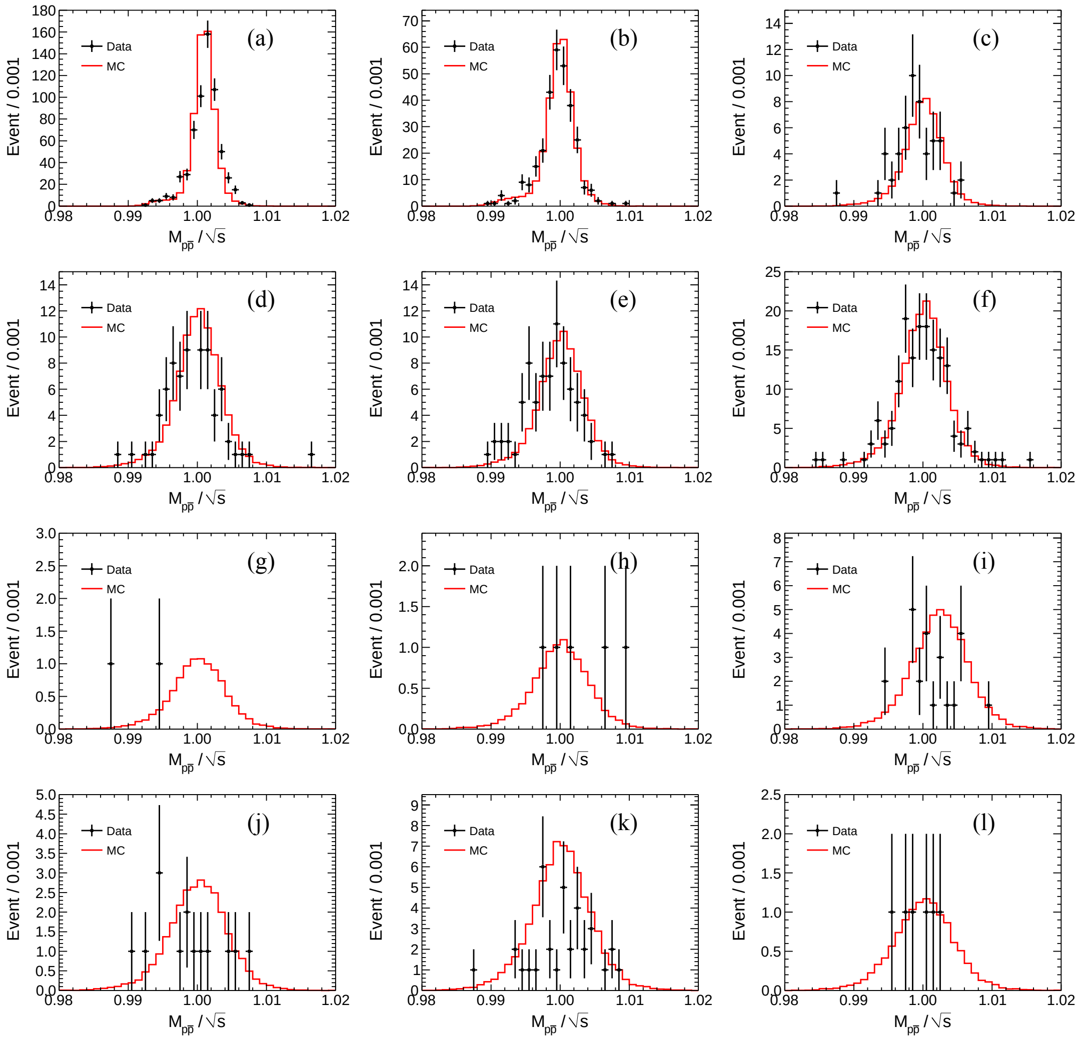

Figure 3.4 Comparison of $M_{p\bar{p}}/\sqrt{s}$ distributions at different c.m. energies for data (dots) and MC (histograms): (a) 2232.4, (b) 2400.0, (c) 2800.0, (d) 3050.0, (e) 3060.0, (f) 3080.0, (g) 3400.0, (h) 3500.0, (i) 3550.7, (j) 3600.2, (k) 3650.0, (l) 3671.0 MeV.

3.2 Extraction of the Born Cross Section of $e^+e^- \to p\bar{p}$ and the Effective FF

3.2.1 Born Cross Section and Effective FF

The differential Born cross section of $e^+e^- \to p\bar{p}$ can be written as a function of FFs, $|G_E|$ and $|G_M|$ [10],

$$\frac{d\sigma_{Born}(s)}{d\Omega} = \frac{\alpha^2\beta C}{4s}[|G_M(s)|^2(1+\cos^2\theta_p) + \frac{4m_p^2}{s}|G_E(s)|^2\sin^2\theta_p], \tag{3.1}$$

where $\alpha = \frac{1}{137}$ is the fine structure constant, $\beta = \sqrt{1-\frac{4m_p^2}{s}}$ is the velocity of proton in e^+e^- c.m. system, $C = \frac{\pi\alpha}{\beta}\frac{1}{1-exp(-\pi\alpha/\beta)}$ is the Coulomb correction factor for a point-like proton, s is the square of c.m. energy, θ_p is the polar angle of the proton in e^+e^- c.m. system. We assume that the proton is point-like above $p\bar{p}$ production threshold, meaning that the Coulomb force acts only on the already formed hadrons. At the energies we are considering here, the Coulomb correction factor can be safely assumed to be 1. Furthermore, under the assumption of the effective FF $|G| = |G_E| = |G_M|$ and by integrating over θ_p, it can be deduced:

$$|G| = \sqrt{\frac{\sigma_{Born}}{86.83\cdot\frac{\beta}{s}(1+\frac{2m_p^2}{s})}}, \tag{3.2}$$

where σ_{Born} is in nb and m_p, s in GeV.

Experimentally, the Born cross section of $e^+e^- \to p\bar{p}$ is calculated by

$$\sigma_{Born} = \frac{N_{obs} - N_{bkg}}{L\cdot\varepsilon\cdot(1+\delta)}, \tag{3.3}$$

where N_{obs} is the observed number of candidate events, extracted by counting the number of signal events, N_{bkg} is the expected number of background events estimated by MC simulations, L is the integrated luminosity estimated with the large angle Bhabha events, ε is the detection efficiency determined from a MC sample generated using the Conexc generator [4], which includes radiative corrections (which will be discussed in detail in next paragraph), and $(1+\delta)$ is the radiative correction factor which has also been determined using the Conexc generator. In the text, the product value $\varepsilon' = \varepsilon \times (1+\delta)$ is presented to account for the effective efficiency.

The derived Born cross section σ_{Born}, the effective FF $|G|$, as well as the related variables used to calculate σ_{Born} are shown in Table 3.4 at different c.m. energies. The comparison of σ_{Born} and $|G|$ to the previous experimental measurements are shown in Fig. 3.5 on linear scale and in Fig. 3.6 on a logarithmic scale. Comparing with the BaBar results [11], the precision of Born cross section is improved by 30% for data sets with $\sqrt{s} \leq 3080.0$ MeV, and the corresponding precision of effective FF is improved, too.

From Eq. 5.1, it is obvious that the detection efficiency depends on the ratio of the electric and magnetic FFs, $|G_E/G_M|$, due to the different polar angle θ_p distribution. In this analysis, the detection efficiency is evaluated with the MC samples. The ratio of $|G_E/G_M|$ is measured for data samples at c.m. energies $\sqrt{s}$ = 2232.4 and 2400.0 MeV, and for a combined data with sub-data samples at $\sqrt{s}$ = 3050.0, 3060.0, and 3080.0 MeV, which have close c.m. energy. The corresponding measured $|G_E/G_M|$ ratios are as the inputs for MC production. Details of $|G_E/G_M|$ ratio measurement can be found in Sec. 3.3. For other c.m. energy points, where the $|G_E/G_M|$ ratios are not measured due to the limited statistics, the detection efficiencies are obtained by averaging the efficiencies with setting $|G_E| = 0$ and $|G_M| = 0$, respectively. The corresponding product values of detection efficiencies and the radiative correction factors at different c.m. energies are listed in Table 3.4. The interference of $p\bar{p}$ final states between e^+e^- annihilation and J/ψ decay in the lower tail is assumed to be negligible [12].

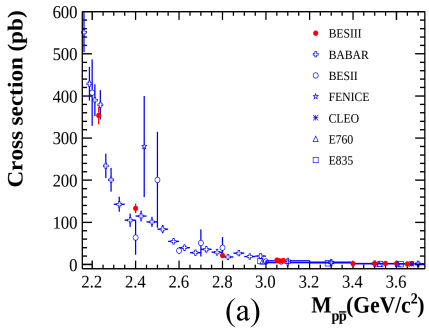

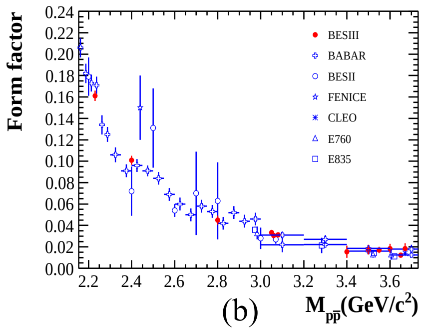

Figure 3.5 Comparison of (a) the Born cross section and (b) effective FF $|G|$, on a linear scale for $M_{p\bar{p}}$ from 2.20 to 3.70 GeV/c^2.

Table 3.4 Summary of the Born cross section σ_{Born}, the effective FF $|G|$. The first errors are statistics, and the second systematics.

$\sqrt{s}$ (MeV)	N_{obs}	N_{bkg}	ε' (%)	L (pb^{-1})	σ_{Born} (pb)	$\|G\|$ ($\times 10^{-2}$)
2232.4	614 ± 25	1	66.00	2.63	$353.0 \pm 14.3 \pm 15.5$	$16.10 \pm 0.32 \pm 0.35$
2400.0	297 ± 17	1	65.79	3.42	$132.7 \pm 7.7 \pm 8.1$	$10.07 \pm 0.29 \pm 0.31$
2800.0	53 ± 7	1	65.08	3.75	$21.3 \pm 3.0 \pm 2.8$	$4.45 \pm 0.31 \pm 0.29$
3050.0	91 ± 10	2	59.11	14.90	$10.1 \pm 1.1 \pm 0.6$	$3.29 \pm 0.17 \pm 0.09$
3060.0	78 ± 9	2	59.21	15.06	$8.5 \pm 1.0 \pm 0.6$	$3.03 \pm 0.17 \pm 0.10$
3080.0	162 ± 13	3	58.97	30.73	$8.8 \pm 0.7 \pm 0.5$	$3.09 \pm 0.12 \pm 0.08$
3400.0	2 ± 1	0	63.34	1.73	$1.8 \pm 1.3 \pm 0.4$	$1.54 \pm 0.55 \pm 0.18$
3500.0	5 ± 2	0	63.70	3.61	$2.2 \pm 1.0 \pm 0.6$	$1.73 \pm 0.39 \pm 0.22$
3550.7	24 ± 5	1	62.23	18.15	$2.0 \pm 0.4 \pm 0.6$	$1.67 \pm 0.17 \pm 0.23$
3600.2	14 ± 4	1	62.24	9.55	$2.2 \pm 0.6 \pm 0.9$	$1.78 \pm 0.25 \pm 0.35$
3650.0	36 ± 6	4	61.20	48.82	$1.1 \pm 0.2 \pm 0.1$	$1.26 \pm 0.11 \pm 0.07$
3671.0	6 ± 2	0	51.17	4.59	$2.2 \pm 0.9 \pm 0.8$	$1.84 \pm 0.37 \pm 0.33$

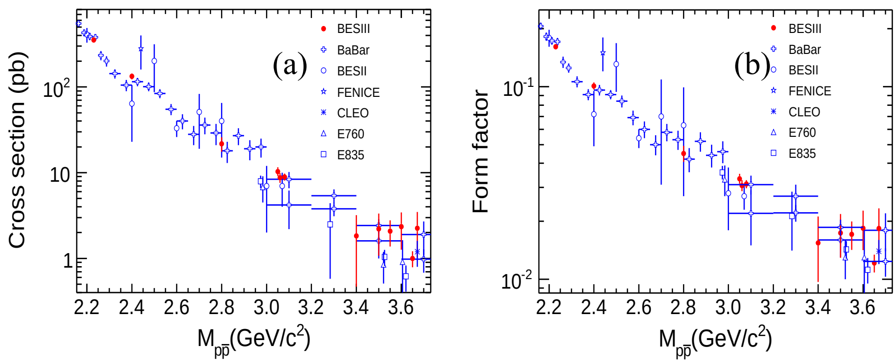

Figure 3.6 Comparison of (a) the Born cross section and (b) effective FF $|G|$, on a logarithmic scale for $M_{p\bar{p}}$ from 2.20 to 3.70 GeV/c^2.

3.2.2 Systematic Uncertainty on σ_{Born}

Several sources of systematic uncertainties are considered in the measurement of the Born cross sections and the corresponding effective FFs, including those of tracking, PID, E/p requirement, background estimation, theory uncertainty from radiative corrections, FF model dependence and integrated luminosity.

- The uncertainty of tracking efficiency is studied from control sample $J/\psi \to p\bar{p}\pi^+\pi^-$ and $\psi(3686) \to \pi^+\pi^- J/\psi \to \pi^+\pi^- p\bar{p}$. The tracking efficiency for proton is defined as $\frac{N_{good=4}}{N_{good\geq 3}}$. Following are the event selection criteria:
  - At least three good charged tracks and two of them are identified to be charged π and one is proton or anti-proton.
  - Require the missing mass in range of (0.85, 1.05) GeV/c^2. For the $\psi(3686)$ decay channel, we also require the recoil mass of $\pi^+\pi^-$ in J/ψ mass window. Fit the missing mass spectrum, we got the $N_{good\geq 3}$.
  - If number of good charge track equals to four, fit the missing mass spectrum, we get the $N_{good=4}$.

  Figure 3.7 shows comparison of tracking efficiency for proton and antiproton in each transverse momentum bin. Figure 3.8 shows comparison of the tracking efficiency for proton and antiproton in each $\cos\theta$ bin. Conservatively, we take 1.0% as the tracking efficiency uncertainty for both proton and anti-proton.

- The uncertainty of PID is also studied with control sample $J/\psi \to p\bar{p}\pi^+\pi^-$ and $\psi(3686) \to \pi^+\pi^- J/\psi \to \pi^+\pi^- p\bar{p}$. The selection criteria is similar to tracking efficiency except that we require four good charged tracks. We firstly studied efficiency of PID by requiring different information on the PID method. There are five different PID requirement: (1) combined information of dEdx, BTOF and ETOF; (2) combined information of dEdx and BTOF; (3) information of d-Edx only; (4) information of BTOF and ETOF; (5) information of BTOF only. From Fig. 3.9, the combined information of dEdx and TOF can give the largest

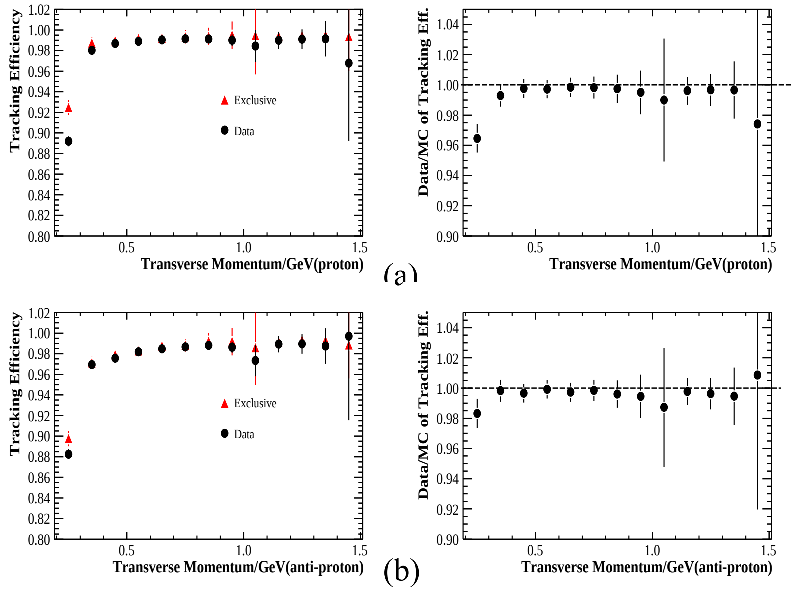

Figure 3.7 Comparison of tracking efficiency for (a) proton and (b) antiproton between data and MC in each transverse momentum bin.

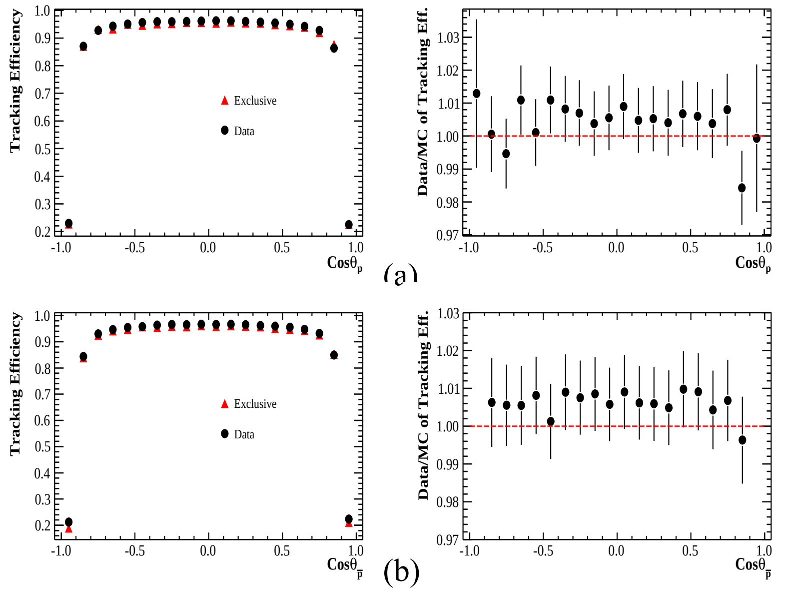

Figure 3.8 Comparison of tracking efficiency for (a) proton and (b) antiproton between data and MC in $\cos\theta$ bin.

efficiency. So we use method (1) to identify proton and antiproton. Figure 3.10 shows comparison of PID efficiency between data and MC in each transverse momentum bin. We take 1.0% as the PID uncertainty for proton and antiproton.

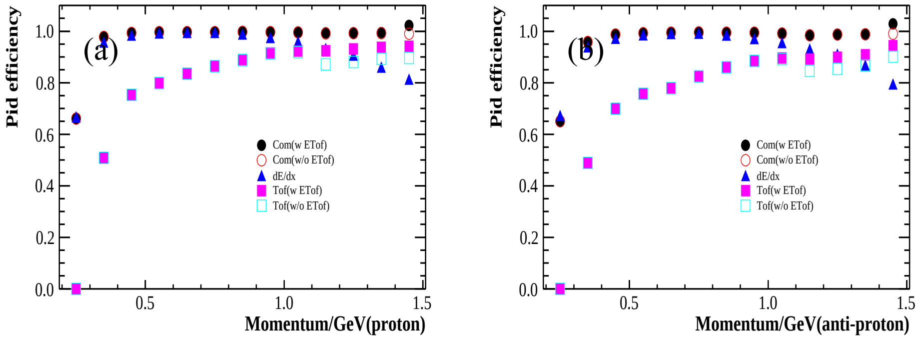

Figure 3.9 Efficiency of PID by requirement different information of detector for proton (a) and antiproton (b).

- For the uncertainty of the E/p cut, we select sample from process $J/\psi \to p\bar{p}\pi^+\pi^-$ and apply different E/p. Figure 3.11 shows comparison of efficiency with different E/p cut between data and MC. For E/p cuts less than 0.4, there are large difference between MC and data which is due to the inaccurate simulation of hadron performance in EMC. But it is safe for us to apply the cut E/p <0.5. And it will bring in 1.0% uncertainty.

- To study uncertainty from background, we use 2D-sideband method to estimate uncertainty of background. Sideband region is selected in $(p_{mean} - 11\sigma,\ p_{mean} - 6\sigma)$ and $(p_{mean} + 6\sigma,\ p_{mean} + 11\sigma)$. Figure 3.12 shows distribution of momentum of proton versus antiproton. Red box is the signal region, green boxes are sideband region and blue boxes are corner regions. The number of sideband background is estimated by number in green boxes minus number in blue boxes.

- Uncertainty of radiative correction factor. In the nominal results, the radiative correction factors are estimated with the Conexc generator. An alternative generator, Phokhara, is used to evaluate the theoretical calculation of radiative cor-

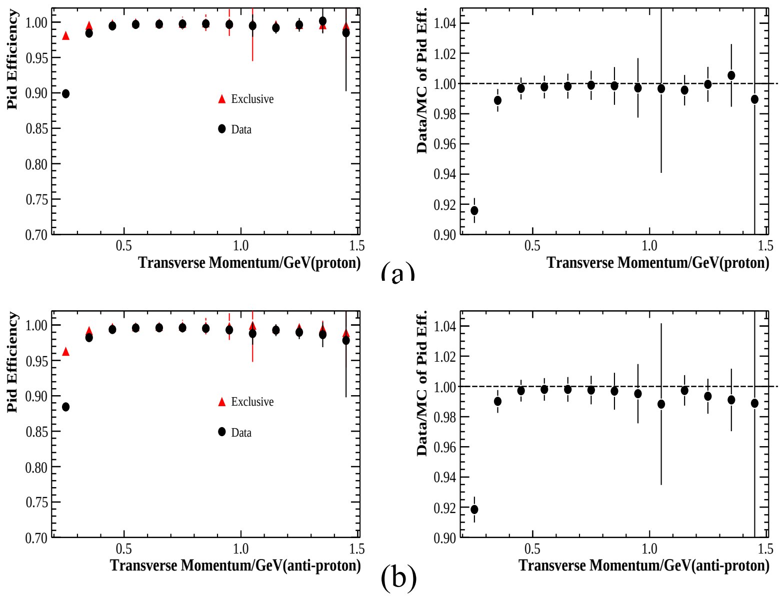

Figure 3.10 Comparison of the PID efficiency for (a) proton and (b) anti-proton between data and MC in each transverse momentum bin.

rection factors, and the difference in the resulting detection efficiency and the radiative correction factor, ε', are taken as the systematic uncertainty.

- For those c.m. energies with measured $|G_E/G_M|$ ratios, the uncertainties on the detection efficiencies are estimated by varying the $|G_E/G_M|$ ratios with 1 standard deviation measured in this analysis, found to be less than 5.0%. For other c.m. energy points, whose $|G_E/G_M|$ ratios are unknown, the uncertainties on the detection efficiencies are evaluated to be half of the differences between the detection efficiencies with setting $|G_E| = 0$ or $|G_M| = 0$, respectively, which give larger uncertainties exceeding 10.0%. Figure 3.13 shows difference on efficiency of this approach for each c.m. energy.

- The integrated luminosity is measured by analyzing large-angle Bhabha scattering process, and achieves 1.0% in precision.

All systematic uncertainties are summarized in Table 3.5. The total systematic uncertainty of the Born cross section is obtained by summing the individual contributions

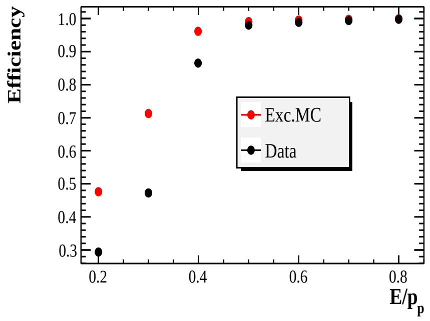

Figure 3.11 Comparison of the efficiency of proton for different E/p cut between data and MC.

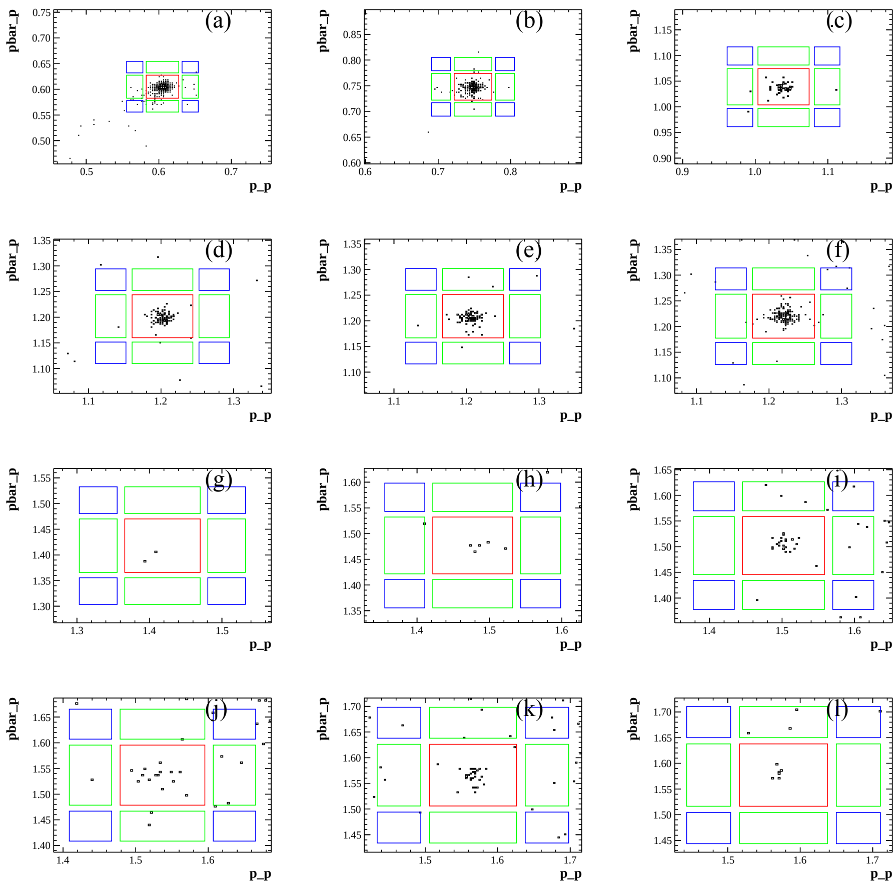

Figure 3.12 2D distribution of momentum of proton versus antiproton for data at different c.m. energies.

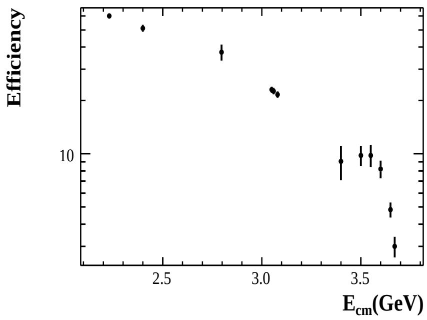

Figure 3.13 Efficiency obtained from MC simulation, plotted in log scale.

in quadrature. The effective FF $|G|$ is proportional to the root square of the Born cross section, and its systematic uncertainty is half of that of the Born cross section.

Table 3.5 Summary of systematic uncertainties (in %) for the Born cross sections σ_B and the effective form factor $|G|$ measurements.

$\sqrt{s}$ (MeV)	Trk.	PID	E/p	Bkg.	MC gen.	Model	Lum.	Total (σ_B)	Total ($\|G\|$)
2232.4	2.0	2.0	1.0	2.6	0.4	1.5	1.0	4.4	2.2
2400.0	2.0	2.0	1.0	2.0	1.8	4.5	1.0	6.1	3.1
2800.0	2.0	2.0	1.0	1.9	7.5	10.2	1.0	13.2	6.6
3050.0	2.0	2.0	1.0	2.2	0.9	4.0	1.0	5.6	2.8
3060.0	2.0	2.0	1.0	3.8	0.1	4.1	1.0	6.4	3.2
3080.0	2.0	2.0	1.0	0.0	0.1	4.3	1.0	5.3	2.7
3400.0	2.0	2.0	1.0	0.0	7.8	21.9	1.0	23.5	11.8
3500.0	2.0	2.0	1.0	20.0	7.0	12.9	1.0	25.0	12.5
3550.7	2.0	2.0	1.0	20.8	9.0	14.3	1.0	27.0	13.5
3600.2	2.0	2.0	1.0	35.7	4.3	11.6	1.0	37.9	18.9
3650.0	2.0	2.0	1.0	3.3	0.9	9.7	1.0	10.8	5.4
3671.0	2.0	2.0	1.0	33.3	0.7	13.3	1.0	36.0	18.0

3.3 Extraction of the Electromagnetic $|G_E/G_M|$ Ratio

3.3.1 Fitting on $\cos\theta_p$

The polar angular distribution of proton θ_p depends on the electric and magnetic FFs. The Eq. 5.1 can be rewritten as :

$$F(\cos\theta_p) = N_{norm}[1 + \cos^2\theta_p + \frac{4m_p^2}{s}R^2(1 - \cos^2\theta_p)], \tag{3.4}$$

where $R = |G_E/G_M|$ is the ratio of electric to magnetic FFs, $N_{norm} = kG_M(s)^2$ is the overall normalization factor, and k is a constant. The R and N_{norm} ($G_M(s)$) can be extracted directly by fitting the $\cos\theta_p$ distributions with Eq. 3.4.

The polar angular distributions $\cos\theta_p$ are shown in Fig. 3.15 for $\sqrt{s}$ = 2232.4 and 2400.0 MeV, as well as for a combined data sample with sub-data samples at $\sqrt{s}$ = 3050.0, 3060.0 and 3080.0 MeV, denoted as 3080.0 MeV in the following. The distributions are corrected with the detection efficiencies in different $\cos\theta_p$ bins which are evaluated by MC simulation samples as shown in Fig 3.14.

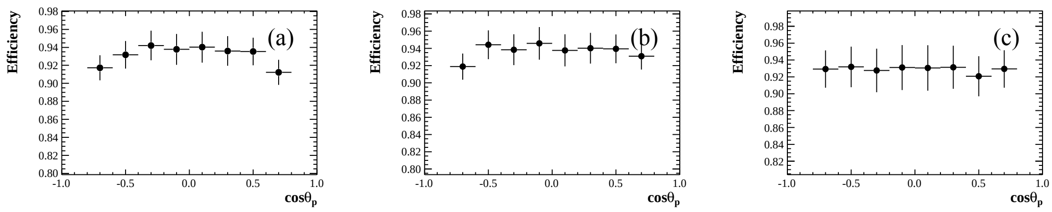

Figure 3.14 Angular dependence of detection efficiency for each c.m. energy region from MC(a) 2232.4, (b) 2400.0 and (c) 3080.0 MeV.

The distributions are fitted with Eq. 3.4 and shown in Fig. 3.15. The fit results as well as the corresponding qualities of fit, $\chi^2/n.d.o.f.$, are summarized in Table A.7, where χ^2 is defined as $\sum_{i=1}^{8}\frac{(\mu_i-\nu_i)^2}{\nu_i}$, μ_i is number of data in each bin and ν_i is number of fitted line in each bin. $n.d.o.f$ is number of freedom which is the number of bins subtracts number of parameters. The MC is then generated by inputting the $|G_E/G_M|$

ratios, and the comparison of angular distribution between data and MC is shown in Fig. 3.16 The corresponding $R = |G_E/G_M|$ ratios are shown in Fig. 3.17, and the results from the previous experiments are also presented on the same plot for comparison.

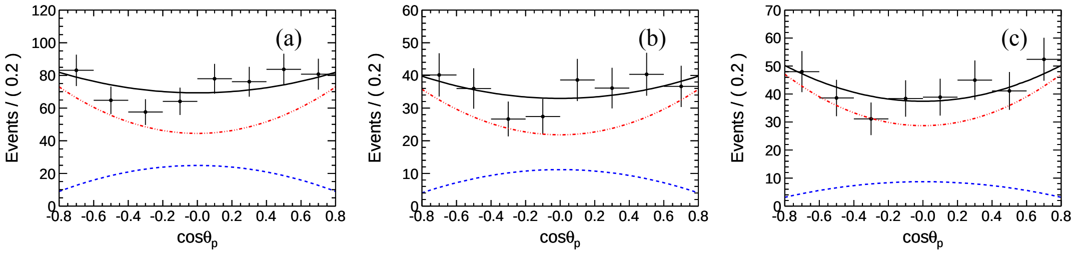

Figure 3.15 The fit results of $\cos\theta_p$ for (a) 2232.4, (b) 2400.0 and (c) 3080.0 MeV. The dashed line shows the contribution of the magnetic FF and the dot-dashed line of the electric FF.

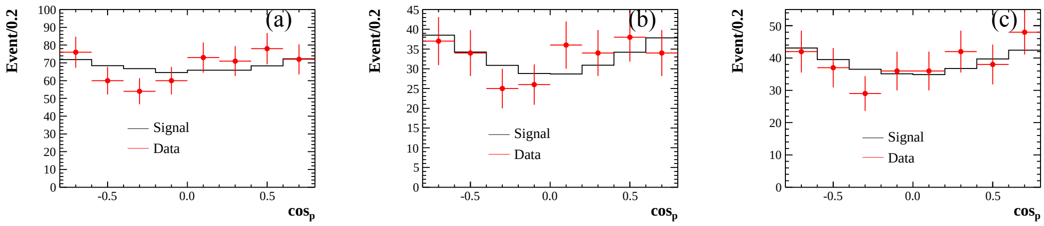

Figure 3.16 Comparison of $\cos\theta$ between data and MC for three c.m. energies: (a) 2232.4, (b) 2400.0 and (c) 3080.0 MeV.

3.3.2 Systematic Uncertainty on $|G_E/G_M|$ Ratio

The systematic uncertainties of the $|G_E/G_M|$ ratio and $|G_M|$ measurements are mainly from the difference of detection efficiency between data and MC, the background contamination, and the different fit range of $\cos\theta_p$. The small background contamination as listed in Table 3.4 is not considered in the nominal fit.

- To account for the difference of efficiency between data and MC on tracking, particle identification and E/p cut, efficiency curves are corrected by data/MC differences. The difference of efficiency versus $\cos\theta_p$ for each item is shown in

Table 3.6 Summary of the ratio of electric to magnetic FFs $|G_E/G_M|$, magnetic FF $|G_M|$ by two methods.

$\sqrt{s}$ (MeV)	$\|G_E/G_M\|$	$\|G_M\|$ ($\times 10^{-2}$)	χ^2/ndf
		Fit on $\cos\theta_p$	
2232.4	$0.87 \pm 0.24 \pm 0.05$	$18.42 \pm 5.09 \pm 0.98$	1.04
2400.0	$0.91 \pm 0.38 \pm 0.12$	$11.30 \pm 4.73 \pm 1.53$	0.74
(3050.0, 3080.0)	$0.95 \pm 0.45 \pm 0.21$	$3.61 \pm 1.71 \pm 0.82$	0.61
		$method\ of\ moment$	
2232.4	0.83 ± 0.24	18.60 ± 5.38	-
2400.0	0.85 ± 0.37	11.52 ± 5.01	-
(3050.0, 3080.0)	0.88 ± 0.46	3.34 ± 1.72	-

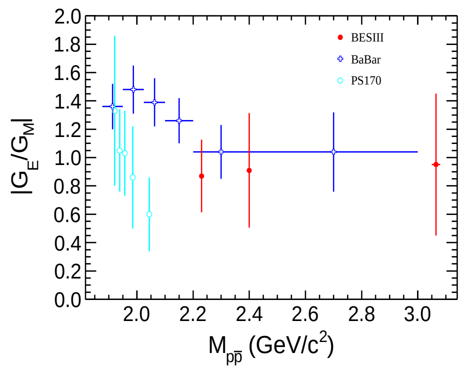

Figure 3.17 The measured ratio of electric to magnetic FFs $|G_E/G_M|$ at different c.m. energy for different experiments.

Fig. 3.18, where the proton sample are selected from the control sample $J/\psi \to p\bar{p}\pi^+\pi^-$. With the difference between data and MC efficiency taking into account, the efficiency corrected curve at $\sqrt{s} = 2.2324$ GeV is shown in Fig. 3.19. Figure 3.20 shows the fitting results of $\cos\theta_p$ with considering efficiency correction of data on $\cos\theta_p$.

- To study the uncertainty from background contamination, an alternative fit with background subtraction is performed, where the background contamination is estimated by the two-dimension sideband method. The fitting results in shown in Fig. 3.21. The differences are considered as the systematic uncertainties related

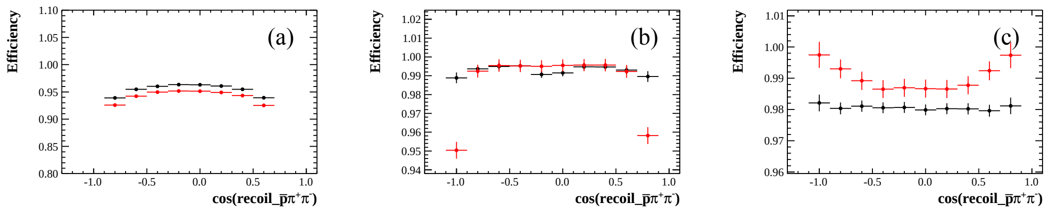

Figure 3.18 The angular dependence efficiency of (a) tracking, (b) particle identification and (c) the E/p cut, between MC and data,

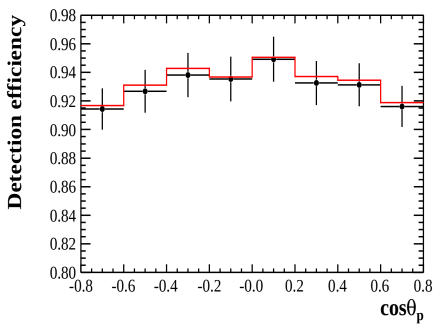

Figure 3.19 Detection efficiency at 2.2324 GeV for MC before (black dots) and after (red line) correction for data in detector response.

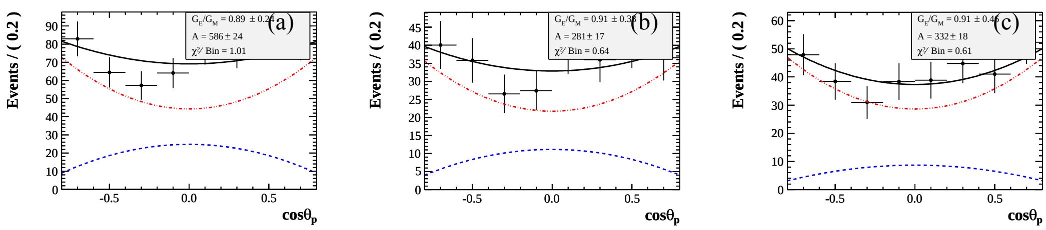

Figure 3.20 Fitting result with considering efficiency correction difference between data and MC: (a) 2232.4, (b) 2400.0 MeV and (c) 3080.0 MeV.

to background contamination.

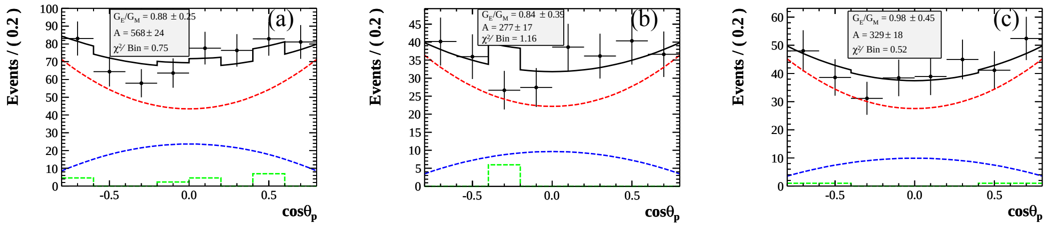

Figure 3.21 Fitting result of $\cos\theta$ with sideband: (a) 2232.4, (b) 2400.0 and (c) 3080.0 MeV. Green dashed line represents the sideband background.

- To study the uncertainty from fitting range, a fit with different range on $\cos\theta_p$ is performed. The fitting result is shown in Fig. 3.22. The differences to the nominal values are taken as the uncertainties.

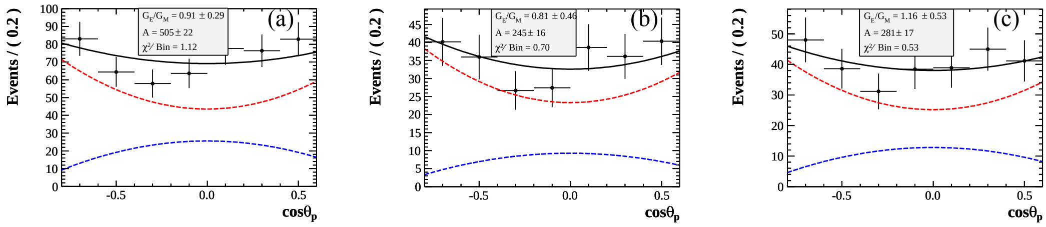

Figure 3.22 Fitting result of $\cos\theta$ by varying the fitting range to (-0.8, 0.6): (a) 2232.4, (b) 2400.0 and (c) 3080.0 MeV.

Table 3.7 summarizes the related systematic uncertainties for the $|G_E/G_M|$ and $|G_M|$ measurements. The overall systematic uncertainties are obtained by summing all the three systematic uncertainties in quadrature.

3.3.3 Method of Moment

As a crosscheck, a different method, named *method of moment* (MM) [13], is applied to extract the $|G_E/G_M|$ ratio, where the weighted factors in front of G_E and G_M may be used to evaluate the electric or magnetic FF from moments of the angular

Table 3.7 Summary of systematic uncertainties (in %) in $|G_E/G_M|$ ratio and $|G_M|$ measurement.

Source	$\lvert G_E/G_M\rvert$			$\lvert G_M\rvert$		
$\sqrt{s}$ (MeV)	2232.4	2400.0	$(3050.0, 3080.0)$	2232.4	2400.0	$(3050.0, 3080.0)$
Background contamination	1.1	7.7	3.2	1.4	7.7	3.2
Detection efficiency	2.3	1.1	4.2	2.3	1.1	4.2
Fit range	4.6	11.0	22.1	4.6	11.0	22.1
Total	5.3	13.5	22.7	5.3	13.5	22.7

distribution directly. The expectation value, or moment, of $\cos^2\theta_p$, for a distribution following Eq. 3.4 is given by:

$$\begin{aligned} < \cos^2\theta_p > = \frac{1}{N_{norm}} \int \frac{2\pi\alpha^2\beta C}{4s} \cos^2\theta_p[(1+\cos^2\theta_p)|G_M|^2 \\ + \frac{4m_p^2}{s}(1-cos^2\theta_p)|R^2|G_M|^2]d\cos\theta_p. \end{aligned} \tag{3.5}$$

Calculating this within the interval [-0.8, -0.8] where the acceptance is non-zero and smooth, gives for the acceptance correction:

$$R = \sqrt{\tau\frac{c < \cos^2\theta > -a}{b - d < \cos^2\theta >}}, \tag{3.6}$$

where $\tau = \frac{s}{4m_p^2}$,

$a = \int(\cos^2\theta + \cos^4\theta)d\cos\theta$,

$b = \int(\cos^2\theta - \cos^4\theta)d\cos\theta$,

$c = \int(1 + \cos^2\theta)d\cos\theta$,

$d = \int(1 - \cos^2\theta)d\cos\theta$.

After calculating the numerical value of the coefficients, Equation 3.6 can be rewrite to be:

$$R = \sqrt{\frac{s}{4m_p^2}\frac{< \cos^2\theta_p > -0.243}{0.108 - 0.648 < \cos^2\theta_p >}}. \tag{3.7}$$

The uncertainty of $< \cos^2\theta >$ is:

$$\begin{aligned}\sigma_{<\cos^2\theta>} &= \sqrt{\frac{1}{N-1}[< \cos^4\theta > - < \cos^2\theta >^2]}\\ &= \sqrt{\frac{1}{N-1}(\frac{e\tau + fR^2}{c\tau + dR^2} - (\frac{a\tau + bR^2}{c\tau + dR^2})^2)},\end{aligned} \tag{3.8}$$

where

$e = \int(\cos^4\theta + \cos^6\theta)d\cos\theta$,

$f = \int(\cos^4\theta - \cos^6\theta)d\cos\theta$.

The corresponding uncertainty of R gives:

$$\begin{aligned}\sigma_R &= \frac{(cb-ad)\tau}{2R(b-d<cos^2\theta>)^2}\sigma_{<\cos^2\theta>}\\ &= \frac{0.0741}{R(0.167- < \cos^2\theta >)^2}\frac{s}{4m_p^2}\sigma_{<\cos^2\theta_p>}.\end{aligned} \tag{3.9}$$

In the analysis of experimental data, $< \cos^2\theta_p >$ and $< \cos^4\theta_p >$ are the average of $\cos^2\theta_p$ and $\cos^4\theta_p$ which are calculated event-by-event, with taking the detection efficiency into account:.

$$< \cos^{2/4}\theta_p >= \overline{\cos^{2/4}\theta_p} = \frac{1}{N}\sum_{i=1}^{N}\cos^{2/4}\theta_{pi}/\varepsilon_i, \tag{3.10}$$

where ε_i is the detection efficiency with ith events kinematics and is estimated by the MC simulation.

For each event in data, a efficiency weighting factor should be taken into consideration. Fig. 3.23 is the efficiency curve. The $\cos\theta$ value in each event should be divided by $f(\cos\theta)$, $f(x) = 0.9359 - 0.002215x + 0.007469x^2 + 0.008019x^3 - 0.1694x^4$. In this way, the efficiency variation from detector has been corrected. Correspondingly, the number of event is recalculated to be N=$\Sigma_0^n \frac{1}{f(\cos\theta)}$. Where n is the number of signal events.

The test of this method is first applied on the MC sample at 2.23 GeV where the input $R = |G_E/G_M| = 1$. In the generate level, the bounds of the integration in Eq. 3.6 Eq. 3.9 is (-1.0, 1.0). For the reconstructed data, the bounds of the integration

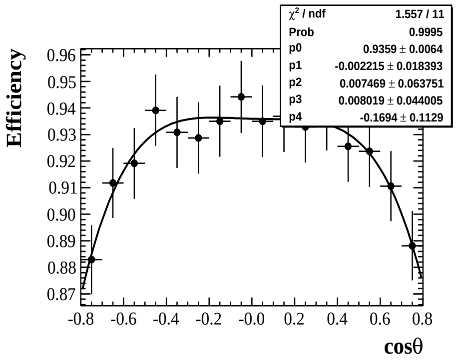

Figure 3.23 The efficiency curve in dependence on $\cos\theta$ at 2.2324 GeV, fitted by a forth order polynomial.

is from (-0.8, 0.8). Table 3.8 shows the result of the R and σ_R with different amount of MC sample calculated by method of moment..

Table 3.8 The calculated $R = |G_E/G_M|$ ratio and the uncertainty for a given number of events.

MC truth events			Reconstructed events		
N	R	σ_R	N	R	σ_R
370000	0.999	0.0064	300000	1.087	0.0111
70000	1.003	0.0144	60000	1.109	0.0251
7000	0.986	0.0454	6000	1.089	0.0784
4000	0.988	0.0642	3000	1.074	0.111
1500	0.952	0.102	1000	0.929	0.170

The extracted $|G_E/G_M|$ ratios and $|G_M|$ by MM at different c.m. energies are shown in Table A.7, too, where $|G_M|$ is calculated by N_{norm} in Eq. 3.4 with the measured $|G_E/G_M|$ ratio. The results are well consistent with those extracted by fitting the distribution of polar angle $\cos\theta_p$, and the statistical uncertainty is found to be comparable between the two different methods due to the same number of events.

3.4 Conclusion

Using data at 14 c.m. energies between 2232.4 MeV and 3671.0 MeV collected with the BESIII detector, we measured the Born cross sections of $e^+e^- \rightarrow p\bar{p}$ and extracted the corresponding effective FF $|G|$ under the assumption $|G_E| = |G_M|$. The results are in good agreement with previous experiments. The precision of Born cross section with $\sqrt{s} \leq 3.08$ GeV is between 6.0% and 18.9% which is much improved comparing with the best precision of previous results (between 9.4% and 26.9%) from BaBar experiment [11]; and the precision is comparable with those of previous results at $\sqrt{s} > 3.08$ GeV. The $|G_E/G_M|$ ratios and $|G_M|$ have been extracted at the c.m. energies $\sqrt{s} = 2232.4$ and 2400.0 MeV and a combined data sample with c.m. energy of 3050.0, 3060.0 and 3080.0 MeV, with comparable uncertainties to previous experiments. The measured $|G_E/G_M|$ ratios are close to unity which are consistent with those of the BaBar experiment at the same q^2 region. At present, the precision of $|G_E/G_M|$ ratio is dominant by statistics. A MC simulation study shows that the precision can achieve 10% or 3.0% if we have a factor of 5 or 50 times higher integrated luminosity. In the near future, a new scan at BEPCII with c.m energy ranging between 2.0 GeV and 3.1 GeV is foreseen to improve the precision of the measurement on $|G_E/G_M|$ ratio in a wide range.

Bibliography

[1] Z. Gao *et al.*, Measurement of the integrated luminositites of the data for R-scan at BESIII. BESIII Analysis Memo BAM-00157.

[2] M. Ablikim *et al.* (BESIII Collaboration), Precision measurement of the mass of the τ lepton. Phys. Rev. D **90**, 1, 012001 (2014).

[3] M. Ablikim *et al.* (BESIII Collaboration), Measurement of the integral luminosities of the data taken by BESIII at $\sqrt{s}$ =3.650 and 3.773 GeV. Chin. Phys. C **37**, 123001 (2013).

[4] R. G. Ping, An exclusive event generator for e^+e^- scan experiments. Chin. Phys. C **38**, 083001 (2014).

[5] H. Czyż, M. Gunia and J. H. Kühn, Simulation of electro-positron annihilation into hadrons with the event generator PHOKHARA. JHEP **1308**, 110 (2013).

[6] C.M. Carloni Calame, An Improved parton shower algorithm in QED. Phys. Lett. B **520** 16 (2001).

[7] C. Bernardini $et\ al.$, Lifetime and beam size in a storage ring. Phys. Rev. Lett. **10** 407 (1963).

[8] M. R. Whalley, A Compilation of data on hadronic total cross-section in e^+e^- interactions. J. Phys. G **29**, A1 (2003);

[9] B. Aubert $et\ al.$ (BaBar Collaboration), Study of $e^+e^- \to \Lambda\bar{\Lambda}$, $\Lambda\bar{\Sigma}^0$, $\Sigma^0\bar{\Sigma}^0$ using initial state radiation with BABAR. Phys. Rev. D **76**, 092006 (2007).

[10] N. Cabibbo and R. Gatto, Electron Positron Colliding Beam Experiments. Phys. Rev. **124** 1577 (1961).

[11] J. P. Lees *et al.* (BaBar Collaboration), Study of $e^+e^- \to p\bar{p}$ via initial-state radiation at BABAR. Phys. Rev. D **87**, 092005 (2013).

[12] M. Ablikim $et\ al.$ (BESIII Collaboration), Study of $J/\psi \to p\bar{p}$ and $J/\psi \to n\bar{n}$. Phys. Rev. D **86**, 032014 (2012).

[13] A. G. Frodesen, O. Skjeggestad and H. Tofte, $Probability\ and\ Statistics\ in\ Particle\ Physics$ Bargen, Norway: Universitetsforlaget (1979) 501p.

Chapter 4

Cross Section Measurement of $e^{+}e^{-} \to \Lambda\overline{\Lambda}$ Near Threshold and at Higher Energies

The Born cross section for the process $e^{+}e^{-} \to \gamma^{*} \to B\bar{B}$ where B is a spin-1/2 baryon, can be expressed in terms of electric and magnetic form factors G_E and G_M:

$$\sigma_{B\bar{B}}(m) = \frac{4\pi\alpha^2 C\beta}{3m^2}[|G_M(m)|^2 + \frac{1}{2\tau}|G_E(m)|^2], \tag{4.1}$$

where $\beta = \sqrt{1 - 4m_B^2/m^2}$ is the velocity, $\tau = m^2/4m_B^2$, m is the invariant mass of $B\bar{B}$ system, and m_B is the mass of baryon. The Coulomb factor, C, corresponding to the correction of re-scattering of pointlike charged fermion pair in the final states, equals to 1 for neutral baryon pair and $\frac{\pi\alpha}{\beta}\frac{1}{1-exp(-\pi\alpha/\beta)}$ for a charged baryon anti-baryon pair [1].

The Coulomb factor in the case of charged baryon pair production gives a non-zero cross section at threshold since it cancels the phase space factor β in the numerator. In the case of neutral baryon pair production, the cross section is expected to increase with the velocity of the final particles in the center-of-mass system, and the threshold angular distribution is expected to be isotropic since the S-wave dominance at threshold. The cross section of $e^{+}e^{-} \to \Lambda\overline{\Lambda}$ close to threshold has been measured in the BaBar experiment [2], in a wide $\sqrt{s}$ bin from $\Lambda\bar{\Lambda}$ threshold up to $\sqrt{s}$=2.27 GeV, to be 204 $\pm$ 60 $\pm$20 pb. Due to the large uncertainty in $\sqrt{s}$, no conclusion about the behavior just above the threshold could be drawn.

BESIII has collected data at a center-of-mass of 2232.4 MeV, which is only 1.0 MeV above $\Lambda\overline{\Lambda}$ production threshold. A precision measurement of the $e^+e^- \to \gamma^* \to \Lambda\overline{\Lambda}$ cross section just above the threshold, provides a test of the C parameterisations and of the hypothesis that Coulomb interactions on the constituent quark level is negligible. Besides the data at 2232.4 MeV, we also using data set at 2400.0, 2800.0 and 3080.0 MeV to study process $e^+e^- \to \Lambda\overline{\Lambda}$ and measure the Born cross section by reconstructing $\Lambda \to p\pi^-$, $\overline{\Lambda} \to \bar{p}\pi^+$.

In this analysis, the process of $e^+e^- \to \Lambda\overline{\Lambda}$ at 2232.4 MeV is generated in phase space distributions. For the charged channel reconstruction, the subsequent decays of $\Lambda \to p\pi^-$, $\overline{\Lambda} \to \bar{p}\pi^+$ are generated with EvtGen. For the neutral channel reconstruction, the decays of $\overline{\Lambda} \to \overline{n}\pi^0$ are generated with EvtGen. The process of $e^+e^- \to \Lambda\overline{\Lambda}$ at 2400.0, 2800.0 and 3080.0 MeV is generated with Conexc generator, the subsequent decays of $\Lambda \to p\pi^-$, $\overline{\Lambda} \to \bar{p}\pi^+$ are generated with EvtGen. The information of data sets we used are shown in Table 4.1.

Table 4.1 The integral luminosity of the analysed data sets.

$\sqrt{s}$ MeV	Lumi. (pb^{-1})
2232.4	2.63
2400.0	3.42
2800.0	3.75
3080.0	30.73

4.1 Measurement of $e^+e^- \to \Lambda\overline{\Lambda}$ Near Threshold

4.1.1 Reconstruction of $\Lambda \to p\pi^-$, $\overline{\Lambda} \to \bar{p}\pi^+$

4.1.1.1 Event Selection

The final state momenta from the process $e^+e^- \to \Lambda\overline{\Lambda}$ are much lower than most of BESIII analyses because the center-of-mass energy is very close to $\Lambda\overline{\Lambda}$ threshold. To study the behaviors of the final states, we generate the signal Monte Carlo events and study the track information event by event. Fig. 4.1 shows one of the typical event behaviors in the detectors. In this plot, we observe two tracks take circles which are low momentum pions. The other two tracks are not proton and antiproton, because the momentum of these tracks are much larger than we expected, but they are the secondary tracks that might come from $\bar{p}$ annihilation.

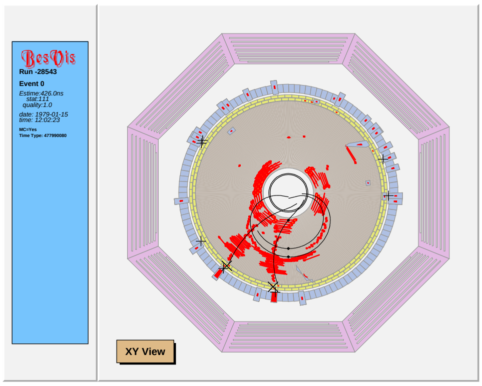

Figure 4.1 Typical behavior of final states in the process of $e^+e^- \to \Lambda\overline{\Lambda}$

The large energy loss for the low momentum proton makes it difficult to observe the track of proton in MDC. For the anti-proton, the cross section of interaction with materials of detectors is large at low momentum range. As a consequence, the anti-proton will annihilate with a proton in the detector material and produce secondary particles. It is therefore impossible to directly observe the anti-proton signal.

Based on the above reasons, the analysis is focused on searching for two low momentum pions and a possible antiproton signal. The good charged pion tracks are required to be well reconstructed from the MDC. They are required to originate from the interaction region $V_{xy} < 1.0$ cm, $|V_z| < 10$ cm, where V_{xy}, V_z are the closest distance of charged tracks to the interaction point (IP). The charged tracks must be within the polar angle $|\cos\theta| < 0.93$, θ is the angle between track and z axis. The number of good charged tracks should be 2 and the net charge should be 0. The pion momentum range is set to be [0.08, 0.11] GeV$/c$ which is determined by the Monte Carlo study as shown in Fig. 4.2.

Pions, kaons and protons are identified by means of dE/dx and TOF information.

The $\chi^2 = \chi^2(dE/dx) + \chi^2(TOF)$ is evaluated for any particle ID hypothesis, and converted into a confidence level. The particle is considered identified if it is consistent to one hypothesis only. In the following the two low momentum tracks are required to be identified as pions which are pions from Λ^0 or $\bar{\Lambda}^0$ decays.

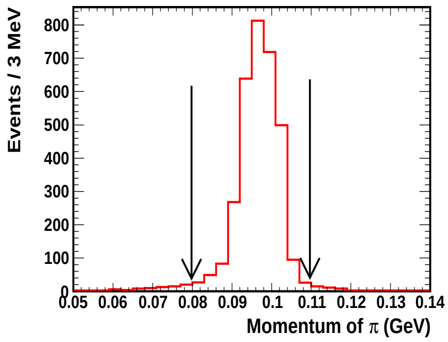

Figure 4.2 The momentum of pions from Λ^0 and $\bar{\Lambda}^0$ decays in MC.

To identify the antiproton, we require V_r less than 5 cm, where V_r is the largest one of V_{xy} of other charged tracks (not including the two low momentum pions). As the Fig. 4.3 shows, the antiproton, interacting on the beam pipe, should produce an enhancement around 3 cm.

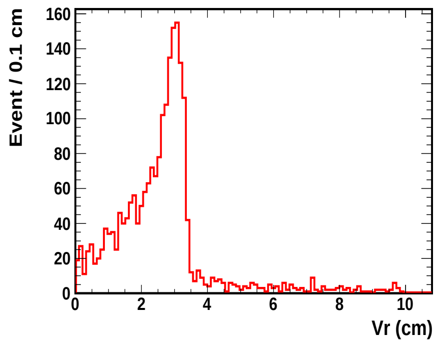

Figure 4.3 V_r distribution, where V_r is the largest one of V_{xy} of other charged tracks which are the secondary tracks from $\bar{\Lambda}^0 \to \bar{p}\pi^+ \to secondaries\ \pi^+$.

4.1.1.2 Background Analysis

The 1.47 pb^{-1} inclusive MC samples generated at $\sqrt{s} = 2232.4$ MeV are used to estimate the remaining backgrounds after the final event selections. The numbers of events from background MC samples are listed in Table 4.2. The main background is from two-photon processes and $q\bar{q}$ events, but the normalized numbers of events are not accurate because the cross section of these processes are poorly known.

Table 4.2 The expected numbers of events of $e^+e^- \to \Lambda\overline{\Lambda}$ annihilation to different final states.

Final states	Luminosity (pb^1)	Events generated	Events survived	Normalized number
e^+e^-	1.47	2.14 M	2	3.6
$\mu^+\mu^-$	1.47	26.7 k	1	1.8
$\gamma\gamma$	1.47	103 k	0	0
e^+e^-X	1.47	24 k	22	39.4
$q\bar{q}$	1.47	53.5 k	339	606.7

Since the cross section of $e^+e^- \to \Lambda\overline{\Lambda}$ and the background channels are not known a priori, the Vr distributions of the signal and background channels in Fig. 4.4 are normalized in such a way that the integral of the MC background distribution equals the integral of the MC signal distribution. In Fig. 4.4, most backgrounds are distributed within the range of [0, 1] cm in contrast to the $e^+e^- \to \Lambda\overline{\Lambda}$ events. This is bacuse the background tracks originate from e^+e^- collisions in the interaction point and not from $\bar{p}$ annihilations in the beam pipe. We could use the maximum value around 0 cm as the scale to estimate this kind of background contribution.

The background of $e^+e^- \to \pi^+\pi^- p\bar{p}$ has the same final state particles as our signal, and we could not use invariant mass of $\pi^- p$ to reconstruct Λ signal to distinguish the background. Therefore we have to estimate the number of this background from the data directly.

By checking the momentum distribution of pions for the process of $e^+e^- \to \pi^+\pi^- p\bar{p}$, the range is from 0.0 to 0.16 GeV/c. If we study the pion momentum range ([0.0 - 0.07] GeV/c and [0.12 - 0.16] GeV/c) which is out of pion momentum range [0.08, 0.11] of $e^+e^- \to \Lambda\overline{\Lambda}$ process, the enhancements around 3 cm could still be observed in the MC

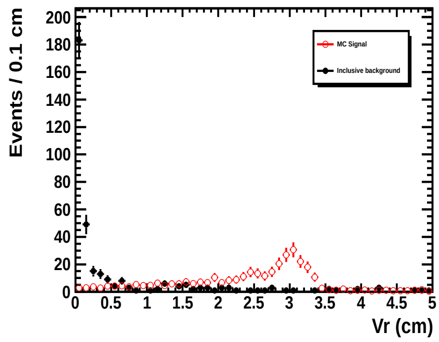

Figure 4.4 The ”Vr” distribution for signal and background from MC simulation.

in Fig. 4.5. But there is no such enhancements in the experimental data. According to the above checks, the process of $e^+e^- \to \pi^+\pi^- p\bar{p}$ is insignificant, and can be neglected when calculating the cross section of $e^+e^- \to \Lambda\bar{\Lambda}$.

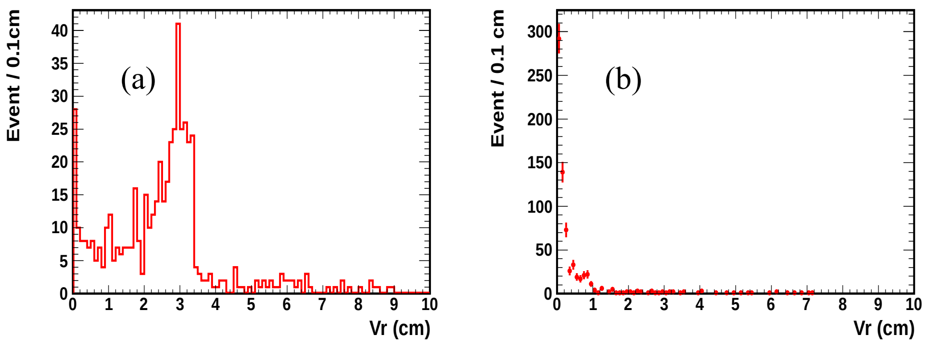

Figure 4.5 The V_r distribution in π momentum region of [0.0 - 0.07] GeV and [0.12 - 0.16] GeV for (a) the MC sample $e^+e^- \to \pi^+\pi^- p\bar{p}$ and (b) experimental data.

4.1.1.3 Fitting the V_r Distribution

After applying the above criteria, requiring two charged pions with momenta within 80-110 MeV/c, the V_r distribution could be drawn in Fig 4.6. The final function used in fitting the V_r distribution consists of the following parts:

1. The $\Lambda\bar{\Lambda}$ events are described by the signal MC shape;

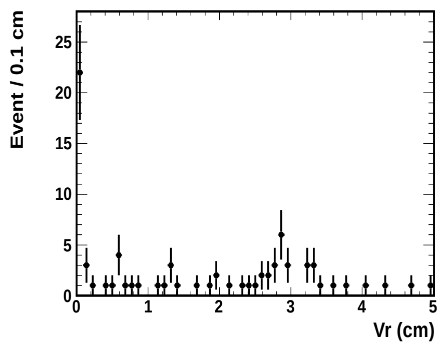

Figure 4.6 The "Vr" distribution in data after applying all the criteria.

2. Backgrounds are described by the shape in the sideband regions.

To check the background shape, we choose the three pion momentum sideband regions to compare with signal region in the V_r distribution. The three sideband regions are

- Sideband region 1: $p_{\pi^+} \in [0.08, 0.11]$ GeV/c and $p_{\pi^-} \in [0.15, 0.18]$ GeV/c;
- Sideband region 2: $p_{\pi^+} \in [0.15, 0.18]$ GeV/c and $p_{\pi^-} \in [0.08, 0.11]$ GeV/c;
- Sideband region 3: $p_{\pi^+} \in [0.15, 0.18]$ GeV/c and $p_{\pi^-} \in [0.15, 0.18]$ GeV/c.

We did Kolmogorov-Test to check the consistence of three sideband regions. The obtained value is larger than 0.99 which means they are consistent with each other. The sideband data can also describe the inclusive MC samples. Therefore, we can use the shape of the distribution corresponding to sideband events.

Fig. 4.8 shows the fitted V_r distribution for charged channel where an un-binned likelihood method is used. The fit yields N = 43 $\pm$ 7. The efficiency is 20.05 % from MC simulation after applying all the selections.

4.1.1.4 Cross Section Measurement

The Born cross section is calculated according to:

$$\sigma^B = \frac{N_{obs}}{\mathcal{L}_{int}(1+\delta)\epsilon\mathcal{B}}, \tag{4.2}$$

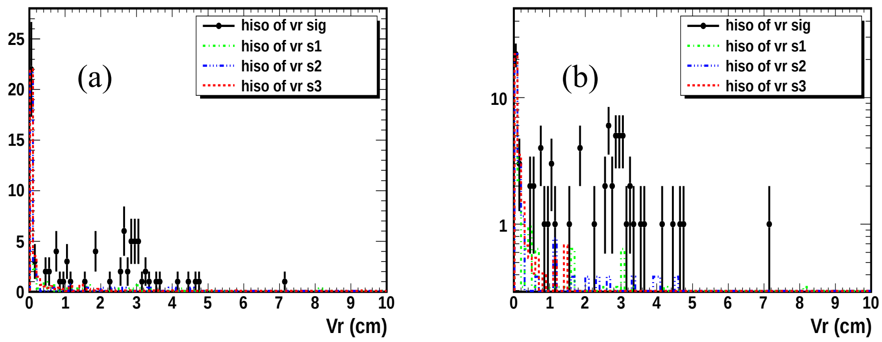

Figure 4.7 (a) V_r distributions for the signal pion momentum regions and sideband regions. (b) The same V_r distribution in log scale.

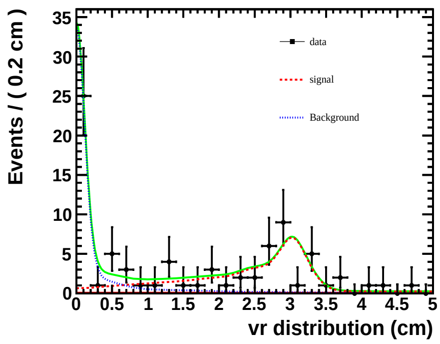

Figure 4.8 The fited V_r distribution.

where N_{obs} is the number of observed events, $\mathcal{L}_{int}$ is integrate luminosity, ϵ is selection efficiency, $\mathcal{B}$ are the branching ratios of $\Lambda \to \pi^- p$ and $\bar{\Lambda} \to \pi^+ \bar{p}$, $(1+\delta)$ is the radiative correction factor.

The radiative correction factor is evaluated considering beam energy spread and ISR, which cause an efficiency loss bringing the effective total energy below the threshold. The total c.m. energy spread at the J/ψ peak has been recently measured to be 0.92 MeV, has previously been found to be 1.3 MeV at the ψ' peak. The energy spread ΔE is expected to be proportional to E^2_{cm} Then energy spread ΔE at 2232.4 MeV can be calculated according to:

$$\Delta E(2.2324) = \Delta E(3.097) \times \frac{2.2324^2}{3.097^2} = 0.48\ MeV. \tag{4.3}$$

With energy spread, the effective c.m ($\Lambda\bar{\Lambda}$ invariant mass) is turned to $E_{eff_1} = E_{cm} + 0.48 \times G(0,\ 1)$, where $G(mean,\ \sigma)$ is the gaussian generator.

In a first approximation the probability of ISR photon emission can be expressed as

$$P(k) = \beta k^{\beta}(k^{-1} - 1 + 0.5k), \tag{4.4}$$

where k is the energy of radiated photon. The "Bond" factor β is due to radiation of photons mostly along direction of incoming electron, given by $\beta = \frac{4\alpha}{\pi}(log(\frac{E}{m_e}) - 0.5) = 0.07$. Taking into account statistical and systematic errors that affect this measurement, the systematic error introduced by the aforementioned approximation is considered negligible.

With radiated photon sampled according to the above function, the effective c.m is again turned to $E_{eff_2} = \sqrt{(E_{eff_1} - k)^2 - k^2}$, where E_{eff_1} is the effective c.m with energy spread correction. We sample 500,000 events at c.m 2232.4 MeV, the effective c.m above $\Lambda\overline{\Lambda}$ threshold is 61.5% which is the radiative correction factor (1+δ). The Born cross section for $e^+e^- \to \Lambda\overline{\Lambda}$ at $\sqrt{s}$ = 2.2324 GeV is 324.6± 52.8 pb.

4.1.1.5 Systematic Uncertainty

The sources of the systematic uncertainty for the cross section measurement are estimated as the follows:

- The uncertainty of tracking efficiency for pions. We choose the process of $J/\psi \to p\bar{p}\pi^+\pi^-$ as the control sample to study the pion tracking efficiency. We choose the same momentum range as our signal to do these studies. The formula is :

$$\epsilon = \frac{N_{4tracks}}{N_{4tracks} + N_{3tracks}}. \tag{4.5}$$

  Firstly, we should identify at least 3 tracks as 1 pion, 1 proton and 1 antiproton with PID method. If the recoil mass of these 3 tracks lies in the pion mass region, the number of events is the denominator when calculating the efficiency. Then, for the rest of tracks, we treat them as pion and draw the total invariant mass of these 4 tracks. We choose the track which invariant mass is closest to the J/ψ

mass. If the difference between the four track invariant mass and J/ψ mass is less than 100 MeV, we take the event number as the numerator. Fig 4.9 shows the comparison of data and MC for the selections.

The pion tracking efficiencies are 72.17 % for MC and 63.28 % for experimental data, respectively. The uncertainty of each pion track efficiency is 12.3%.

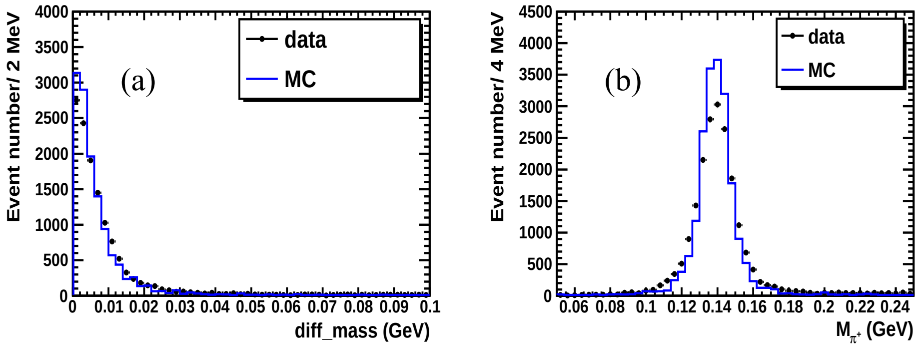

Figure 4.9 (a) The difference between invariant mass of 4 tracks and J/ψ mass (b) The distribution of 3 tracks recoil mass.

- The PID uncertainty for the pions. We also use the process of $J/\psi \to p\bar{p}\pi^+\pi^-$ as the control sample to study the pion PD efficiency which is defined as:

$$\epsilon = \frac{N_{PID}}{N_{4tracks}}, \tag{4.6}$$

where $N_{4tracks}$ is the same as the above definition and N_{PID} is the event number after applying the PID selection for pion. The pion PID efficiencies are almost 100% for both experimental data and MC because of the low pion momentum. The uncertainty for the each pion PID efficiency is 1% as a conservative estimation caused by the statistic of experimental data.

- The antiproton efficiency uncertainty is calculated by comparing the MC and data by the process of $J/\psi \to p\bar{p}\pi^+\pi^-$ which is defined as:

$$\epsilon = \frac{N_{Vr}}{N_{\bar{p}}}, \tag{4.7}$$

where $N_{\bar{p}}$ is defined as the event number when the recoil mass of π^+, π^- and p lies in the $\bar{p}$ mass region, and N_{Vr} is the event number after requiring the Vr less than 5 cm. The anti-proton efficiencies are 85.4% for MC and 85.6% for experimental data, respectively. The uncertainty for the each anti-proton track efficiency is 0.3%.

- The uncertainty of background shape: We use the inclusive MC shape instead of the sideband shape and the event number is changed from 43 to 41. The uncertainty is 4.6%.

- The uncertainty of MC generator: In our current analysis, we used Phase Space to generate the process. Then ISR correction factor is then calculated by a home-made fortran code which include energy spread and ISR into consideration. To cross check this method, we use Conexc to generate this process, the input line-shape is flat from threshold to 2232.4 MeV, the energy spread is 0.48 MeV. The corresponding ISR correction factor is 0.634 and the efficiency difference of these two method is 3.2%.

- The uncertainty of energy spread: In the $\psi(3686)$ scan for the data taken at $\Lambda_c\overline{\Lambda}_c$ threshold, the BEPCII energy spread is 1.6 MeV, instead of 1.3 MeV. Here, if we use 1.6 MeV to do E^2 extrapolation, the energy spread at 2232.4 MeV would be 0.59 MeV, and the corresponding correction factor is 0.603. The systematic error on cross section measurement is 2.0%.

- The uncertainty of energy measurement: In the reconstruction of $e^+e^- \to p\bar{p}$, we fit the invariant mass of $p\bar{p}$ by a single gaussian. The mean value of the center-of-mass is measured to be 2232.9 ± 0.2 MeV, which 0.5 MeV difference from the required energy, 2342.4 MeV. Therefore, we take 0.5 MeV as the uncertainty of energy scale. The ISR and energy spread correction factor at 2232.9 MeV is 0.639, which brings 3.9% uncertainty.

- Luminosity uncertainty is estimated to be 1.0% by analyzing large angle Bhabha scattering events [4].

We treat all the uncertainties uncorrelated and sum in quadrature. The total uncertainty is 13.4%.

The total uncertainties of the cross section measurement are listed in the Table 4.3.

Table 4.3 Uncertainty of the cross section measurement for charged channel.

Source	Uncertainty (%)
pion track efficiency	12.3
pion PID efficiency	1.0
anti-proton selection	0.3
Background line shape	4.6
MC generator	3.2
Energy spread	2.0
Energy scale	3.9
Luminosity	1.0
total	14.3

4.1.2 Reconstruction of $\overline{\Lambda} \to \bar{n}\pi^0$

4.1.2.1 Event Selection

In this analysis, instead of selecting the charged channel of $\Lambda \to p^+\pi^-$ and $\overline{\Lambda} \to \overline{p}\pi^+$, we used a semi-inclusive method by tagging only the $\overline{\Lambda} \to \overline{n}\pi^0$ decay. Comparing to charged decay channel of Λ or $\overline{\Lambda}$, the neutral channel of $\overline{\Lambda}$ has a smaller branching ratio, but by using semi-inclusive method, this loss is recovered. In the neutral channel of $\overline{\Lambda}$, $\overline{n}$ gives a signal in the EMC and the monoenergetic π^0 has a momentum of 105 MeV. Furthermore, $\overline{n}$ and π^0 has an opening angle larger than 140°. This information can be used to select signals from data.

Following are the event selections for this channel:

- For one event, the maximum number of good charged tracks is 2, which would come from $\Lambda \to p\pi^-$. A good track should satisfy $|V_r| < 1$ cm, $|V_z| < 10$ cm and $|\cos\theta| < 0.93$.
- Shower candidates are selected in the EMC by requiring a minimum energy deposition of 25 MeV in Barrel and 50 MeV in Endcap. If the number of charged track

is larger than 0, the opening angle between the shower to the closest charged track should be larger than 10°. For one event, there should be at least 3 good showers. To suppress the beam-associated noise, the number of good shower should be less than 20.

- The most energetic shower is selected as the $\bar{n}$ candidate. The quantities for the $\bar{n}$ candidate used for Multiple Variable Analysis (MVA) are:
  - energy deposit of the $\bar{n}$ shower (denoted "energy");
  - the full energy deposit within a 40° cone (denoted "ene_40d");
  - second moment of $\bar{n}$ shower (denoted "secmom");
  - lateral moment of $\bar{n}$ shower (denoted "latmom");
  - the energy seed of $\bar{n}$ shower (denoted "eseed");
  - number of hits of $\bar{n}$ shower (denoted "hit");
  - the total number of hits within a 40° cone of $\bar{n}$ shower (denoted "hit_40d");
  - $(E5\times5-E3\times3)/E5\times5$ (denoted "shape"), where $E5\times5/E3\times3$ denotes the energy deposited in $5\times5/3\times3$ crystals.
- To select a π^0 candidate, a mass constrained kinematic fit is applied for each photon pair. The angle between the π^0 candidate and $\bar{n}$ candidate is required to be larger than 140°. The photon pair from the π^0 decay should satisfy EMC timing requirement ($0 \leq T \leq 14$) in units of 50 ns) which is used to suppress electronic noise and to remove showers unrelated to the events. To remove background events in which a π^0 is falsely reconstructed from a high energy photon and a second spurious shower, the energy asymmetry $|E_{\gamma_1} - E_{\gamma_2}|/p_{\pi^0}$ is required to be less than 0.95. After applying these selection criteria, the photon pair with minimum χ^2_{1C} is selected as π^0 candidate. Figure 4.10(a) shows the comparison of χ^2_{1C} distribution for signal MC, data and background. To improve the signal-to-background ratio, events with $\chi^2_{1C} < 20$ are accepted by optimizing the figure of merit $S/\sqrt{S+B}$, as shown in Fig. 4.10(b), where S is the number of simulated

signal events with normalized to 80 events, and B is the number of $q\bar{q}$ background and separated beam background after normalized according to Table 4.4.

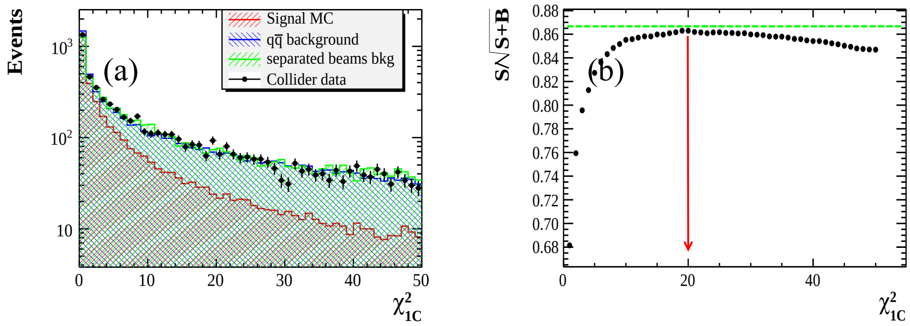

Figure 4.10 (a) Comparison of χ^2_{1C} distribution. (b) The figure of merit $S/\sqrt{S+B}$.

4.1.2.2 Background Analysis

After the preliminary selection, most background events from Bhabha ($e^+e^- \to e^+e^-$), Dimu ($e^+e^- \to \mu^+\mu^-$), Digamma ($e^+e^- \to \gamma\gamma$), and two-photon process ($e^+e^- \to e^+e^-X$) have been removed. Table 4.4 shows the survived number of different channel of background and signal MC for each selection criteria, from which we can conclude that inclusive hadronic final states $q\bar{q}$ is the dominant physical background source. Among the hadronic final state background channel, many contain several π^0s, which come from η, η', ω, ρ and K^0_s. There is no dominant background channel in this analysis. The normalized factor is determined by N^{exp}/N^{gen}, where N^{exp} is the number of events calculated according to the cross section and luminosity, N^{gen} is the number of events generated by MC simulation. The normalized background contaminated in data is shown in the last row.

Apart from the physical background, there is beam-associated background, which include events come from the interaction between beam and the beam pipe, beam and residual gas and the Touschek effect. A special data sample, collected with BESIII detector at c.m. energy 2.40 GeV and 3.40 GeV, but with the separated (non-colliding) beams, is dedicated to study the beam associated background. Since the two beam don't interact with each other, all of the observed events are beam associated background, and can be used to evaluate the beam associated background at c. .m energy 2.2324 GeV. The background from separated beam events is much higher than the experimental data. Therefore, the separated beam background can not be normalized according to the data-taking time or the number of events. The cut flow of the separated beams and the corresponding normalized events is shown in the last column in Table 4.5. Since there are 4686 events survived in collider data @ 2232.4 GeV and 1493 events of $q\bar{q}$ background, the number of events from separated beam is then normalized to 3193. Figure 4.11 shows the comparison of the variables between data and background with each components normalized. They show good consistence.

Table 4.4 The survived number of different background process and signal process for each selection criteria.

Channel	Bhabha	Dimu	Digamma	Two-photon	$q\bar{q}$	signal MC (PHSP)
Total number	9.60×10^6	7.00×10^5	1.90×10^6	8.0×10^4	1.99×10^6	1.10×10^5
$N_{good} <= 2$	9.57×10^6	6.99×10^5	1.90×10^6	7.7×10^4	1.10×10^6	108405
$N_{shower} >= 3$	17.44×10^3	1285	14.52×10^4	1.8×10^4	7.25×10^5	100705
π^0 sel	52	8	112	1015	6.87×10^4	42794
χ^2_{1C} <20	23	3	42	484	3.24×10^4	35772
cross section(nb)	1434.01	17.41	70.44	0.41	34.82	
expected num.	3.77×10^6	4.58×10^4	1.85×10^5	1078	9.16×10^4	
normalized factor	1/2.5	1/15.3	1/10.3	1/74	1/21.7	
normalized num.	9	0	4	7	1493	

Table 4.5 The survived number of data from separated beams and experimental data @ 2232.4 MeV for each selection criteria.

Channel	sep. beams @ 2400.0 MeV	sep. beams @ 3400.0 MeV	exp. data @ 2232.4 MeV
Total number	9.41×10^6	13.19×10^6	57.14×10^6
$N_{good} <= 2$	9.41×10^6	13.19×10^6	57.06×10^6
$N_{shower} >= 3$	2.21×10^6	2.59×10^6	14.01×10^6
π^0 sel	1894	4449	10629
$\chi^2_{1C} < 20$	888	2153	4686

4.1.2.3 Multiple Variable Analysis

A multiple variable analysis (MVA) is used to classify signal and background. 20k signal MC and 7.5k background are used for training and samples of the same size are

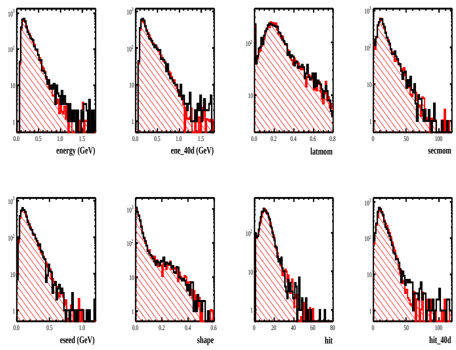

Figure 4.11 Comparison of variables between data and background.

used for testing, where the signal MC is the process $e^+e^- \to \Lambda\overline{\Lambda} \to \Lambda\bar{n}\pi^0$ which passes the above event selection, the background is a mix between $q\bar{q}$ and the separated beam events normalized to the data.

Figure 4.12 shows the comparison of input variables between signal and background. Figure 4.13 shows the linear correlation matrices for the input variables in the training sample. Three MVA methods are booked to classify background and signal Maximum Likelihood, Artificial Neural Network (ANN) and Boosted decision trees (BDT). The background rejection versus signal efficiency for different classifiers is shown in Fig. 4.14(a). The BDT classifier gives better performance than the likelihood estimator in the three method (likelihood, ANN and BDT). To make sure that the BDT classifier gives best performance of separating signal and background, various MVA methods are used and the background rejection versus signal efficiency is shown in Fig. 4.14(b), from which we can find that the BDT is the best classifier. In the following, the BDT estimator is further studied to classify signal/background.

To study whether the sample is overtrained, distributions of the classifiers between test and training samples are compared for BDT classifier, as shown in Fig. 4.15. From the Kolmogorov-Smirnov test, the probability of signal and background are both larger than 0.05 for BDT classifier, therefore, we can conclude that the training sample is not overtrained.

For the nine input variables, an importance ranking is provided by BDT classifier

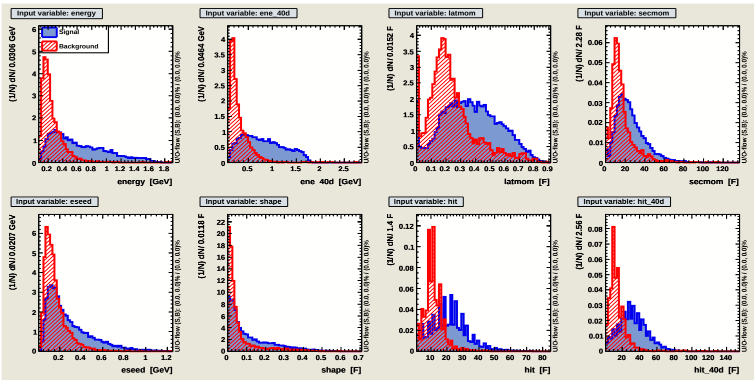

Figure 4.12 Comparison of input variables between signal and background.

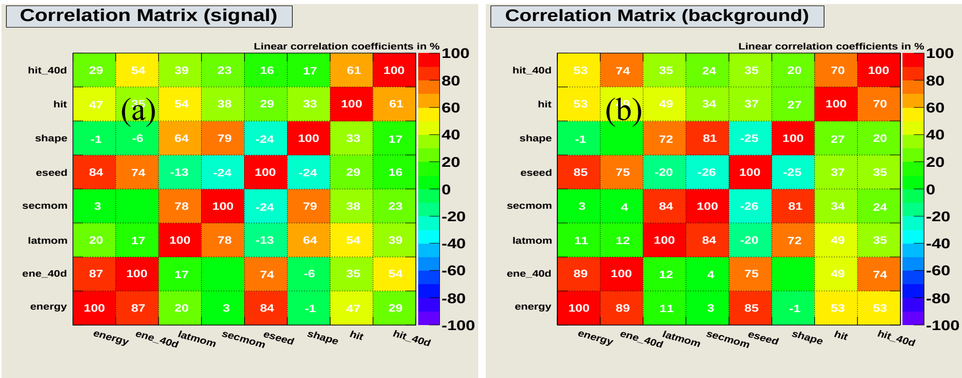

Figure 4.13 The linear correlation matrices for the input variables in the training sample for (a) signal sample and (b) background sample.

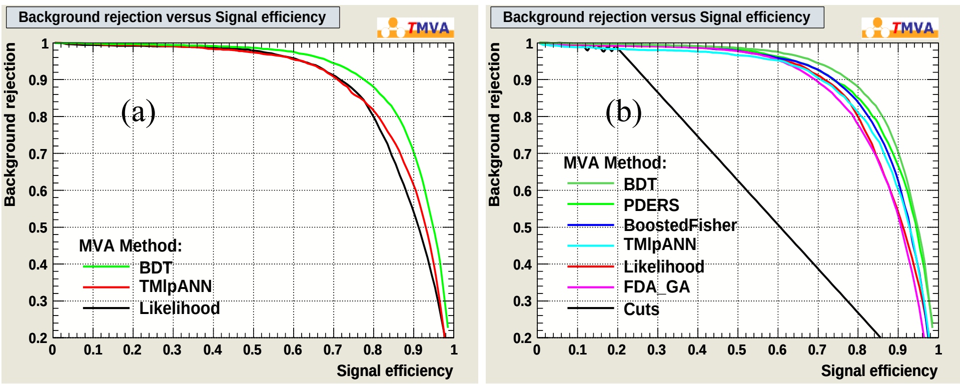

Figure 4.14 Background rejection versus signal efficiency for different classifier outputs.

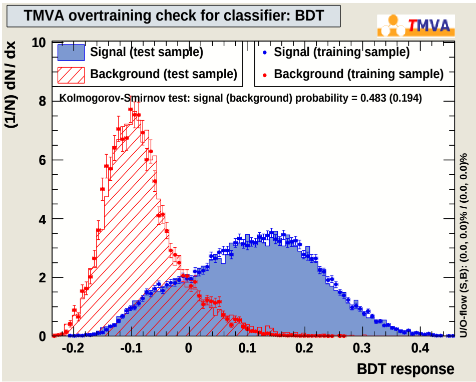

Figure 4.15 Classifier output distribution with test and training samples superimposed for BDT classifier.

as shown in Table 4.6.

Table 4.6 Ranking result for BDT classifier, top variable is best ranked.

Rank	Variable	Variable Importance
1	ene_40d	2.423e-01
2	energy	1.959e-01
3	eseed	1.310e-01
4	hit_40d	1.060e-01
5	hit	1.022e-01
6	latmom	9.272e-02
7	secmom	7.598e-02
8	shape	5.389e-02

After the MVA study, assuming the cross section of $e^+e^- \to \Lambda\bar{\Lambda}$ is 300 pb, there are 57 events in data and the signal to background ratio is 1:80. The optimal classifier cut value is determined for signal to background ratio 1:80 for BDT classifier, where the cut efficiencies for signal and background and the optimal cut value are shown in Fig. 4.16. The optimal cut is ”mva”>0.1309 for BDT classifier.

4.1.2.4 Fitting the P_{π^0} Distribution

Figure 4.17 shows scatter plots of $m_{\gamma\gamma}$ versus π^0 momentum P_{π^0} for experimental data, MC signal events, simulated $q\bar{q}$ background events and separated beam data after application of the MVA method. Signals are centred in the [0.08, 0.12] GeV region in

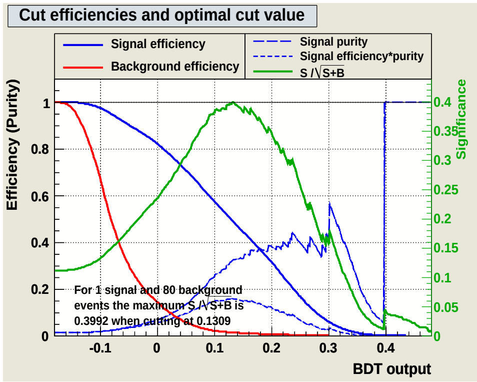

Figure 4.16 The cut efficiencies with different output classifier applied with 100 signal and 500 background events assumption for BDT classifier.

X-axis which corresponds to π^0 momentum, while in the data, concentration appears in the same region. It indicates the existence of a $\Lambda\bar{\Lambda}$ signal in the data.

The projection of P_{π^0} in the data is shown in Fig. 4.18(a), as well as the stack plot of signal and background, where the background is normalized. The peak around 0.1 GeV/c is not produced from background. To study the possible exclusive peaking background which has the same final states as the signal process, such as such as $e^+e^- \to p\pi^-\bar{\Lambda} \to p\pi^-\bar{n}\pi^0$ and $e^+e^- \to n\bar{n}\pi^0\pi^0$, the sample of such MC process is generated. The selection efficiency for the two processes are 4.6% and 6.3%, respectively. The number of events for the two exclusive background is estimated by assuming the cross section is the same as $e^+e^- \to \Lambda\bar{\Lambda}$, and the corresponding distribution on P_{π^0} is shown in Fig. 4.18(b), where there is no peak observed in the distribution of background processes.

The signal yields in data is obtained by fitting momentum distribution of π^0 with the un-binned method, where the signal is described by MC shape convoluted with a gaussian function, and background is described by a second-order polynomials. The result is shown in Fig. 4.19. The yield number of signal events is 22.8 ± 7.7. The significance of signal is 4.3σ. Selection efficiency is 13.0% from MC simulation which is generated in phase space. To account for the possible D-wave in the process $e^+e^- \to \Lambda\bar{\Lambda}$, we generate a set of MC by setting the angular distribution of Λ into $(1 + \cos^2\theta)$,

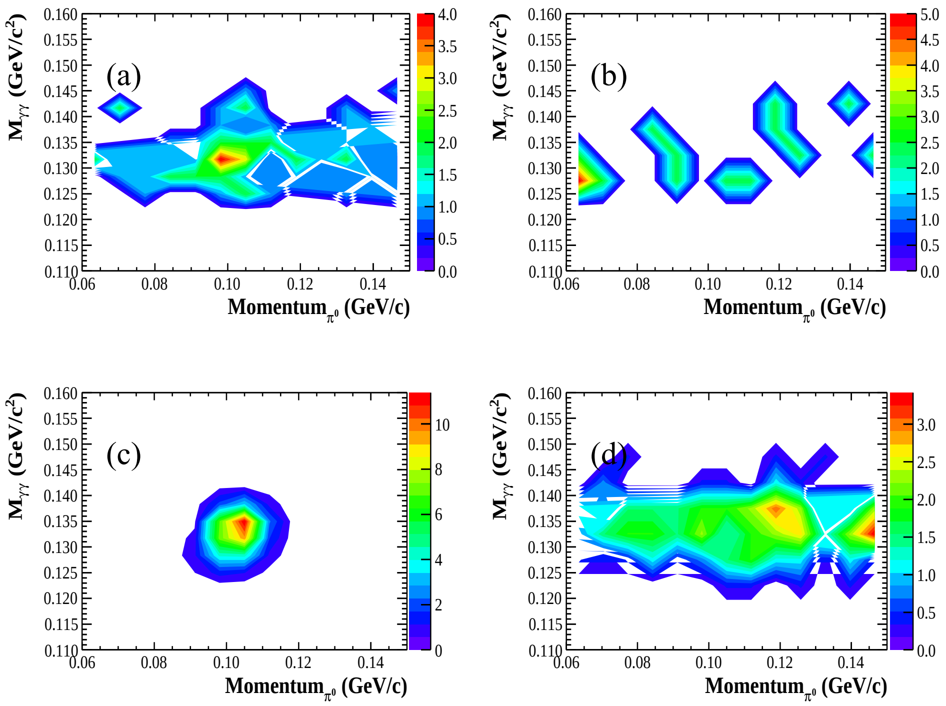

Figure 4.17 Scatter plot of M_{π^0} versus p_{π^0} for (a) data, (b) separated beams background, (c) signal MC and (d) $q\bar{q}$ background.

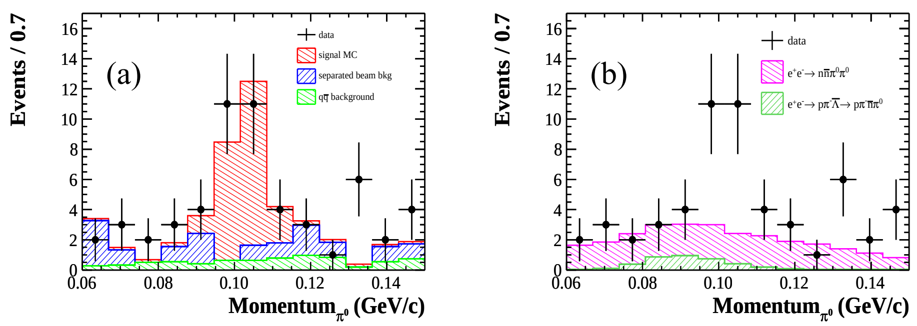

Figure 4.18 Momentum distribution of π^0 (a) between data and inclusive background, (b) between data and possible exclusive background processes.

the difference of the reconstructed efficiency to phase space MC is only 0.5%.

Cross section for $e^+e^- \to \Lambda\bar{\Lambda}$ is calculated to be:

$$\begin{aligned}\sigma &= \frac{N_{sig}}{\varepsilon \times (1+\delta) \times L \times Br(\bar{\Lambda} \to \bar{n}\pi^0) \times Br(\pi^0 \to \gamma\gamma)} \\ &= \frac{22.8 \pm 7.7}{13.0\% \times 61.5\% \times 2.63 \times 35.8\% \times 98.8\%} = 306.6 \pm 103.5\ pb.\end{aligned} \tag{4.8}$$

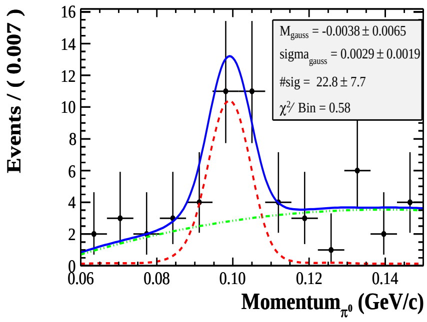

Figure 4.19 The results of fitting the momentum distribution of π^0.

4.1.2.5 Systematic Uncertainty

- To study the $\bar{n}$ selection efficiency, we select the $\bar{n}$ sample from the $J/\psi \to p\bar{n}\pi^-$ control sample. The selection of good charged track is the same as described in section. 4.1.2.1, and at least two good charged tracks are required. The number of positive protons and negative pions are required to equal to 1 after the particle identification. Missing one $\bar{n}$, a 1C kinematic fit is performed on the proton and pion, and χ^2_{1C} is required to be less than 10. After the selection, the purity of sample is estimated to be 97.29% from the topology of inclusive MC. No peaking background is observed in the recoil mass of proton and pion.

  The number of observed events in the sample, denoted as N_{sample}, is obtained by fitting the invariant mass of the recoil vector of proton and pion by an MC shape convoluted with a Gaussian function and a flat background described by polynomials, since there is no peaking background from inclusive MC study. $\bar{n}$

candidates are the most energetic showers (as described in section 4.1.2.1) and the angle of the shower with recoil vector of proton and pion is less than $40°$. The number of $\bar{n}$ detected satisfying the above selection criteria, denoted as $N_{\overline{n}}$, is obtained by fitting the invariant mass of recoil vector of proton and pion.

Figure 4.20 shows the efficiency of $\bar{n}$ selection in data and MC. The difference of efficiency of $\bar{n}$ selection in high momentum region for data and MC is large. At low momentum region [0.03, 0.18] GeV, the overall selection efficiency of $\bar{n}$ is $(71.4 \pm 1.0)\%$ for data and $(71.0 \pm 0.7)\%$ for MC. Therefore, for our analysis process, the difference of the efficiency of $\bar{n}$ selection is $(0.4 \pm 1.2)\%$. Therefore the conservative systematic uncertainty is $1.6/0.71\% = 2.2\%$.

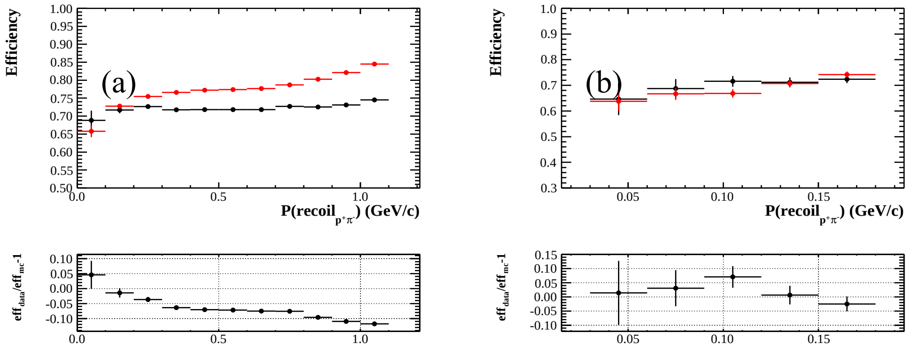

Figure 4.20 (a) $\bar{n}$ selection efficiency in momentum region (a) [0.0, 1.2] GeV/c and (b) [0.03, 0.18] GeV/c in data (black) and MC(red).

- The selection efficiency of π^0 is studied by using the $\psi(3686) \to \pi^0\pi^0 J/\psi$ control sample. The J/ψ resonance is tagged through decay channel $J/\psi \to e^+e^-/\mu^+\mu^-$, and the high momentum π^0 is tagged. In order to avoid overlapping momentum regions, the tagged high momentum π^0 is required to be larger than 0.3 GeV/c.

  Following are the event selection: To tag the J/ψ resonance, number of good charged tracks is required to be larger than 2. There should be two tracks with momentum larger than 1.0 GeV identified as lepton tracks. For e^+e^- channel, the ratio of energy deposited in EMC and the momentum measured in MDC, E/p, should be larger than 0.7; For $\mu^+\mu^-$ channel, the energy deposited in EMC should be smaller than 0.45 GeV. And the mass window for lepton pairs is required to be in [2.95, 3.20] GeV/c^2.

To tagged the high momentum π^0, at least two good showers are selected. Energy of the photons in π^0 candidates should be larger than 0.08 GeV. The momentum of the π^0 is larger than 0.3 GeV. To veto the background from $\psi(3686) \to \gamma\chi_{cJ} \to \gamma\gamma J/\psi$, the momentum of π^0 should be less than 0.4 GeV. Since one π^0 is untagged, a 1C kinematic fit is performed for π^0 and two leptons and χ^2_{1C} is required to be less than 20. The background level studied from inclusive MC is 0.33%.

The low momentum π^0 selection efficiency is defined as: N_{obs}/N_{tag}, where N_{tag} is the number of events which survived the above selection criteria contain a high momentum π^0, whereas N_{obs} is the number of events where also a low momentum π^0 is reconstructed. The selection criteria of the low momentum π^0 is the same as described in section 4.1.2.1. Figure 4.21 shows the momentum of the recoil vector of tagged π^0 and J/ψ, the black dots represent the observed events of tagging π^0 and J/ψ, the red line represents the events of tagged π^0, J/ψ and the other π^0. Figure 4.22 shows the efficiency of π^0 selection in data and MC. The overall efficiency of π^0 selection in momentum region [0.03, 0.24] GeV/c is $(51.06 \pm 0.16)\%$ for data and $(51.90 \pm 0.18)\%$ for signal MC. The difference of the selection efficiency of π^0 is $(0.84 \pm 0.25)\%$. The conservative uncertainty of π^0 selection is 2.1%.

- The uncertainty of the cut on χ^2_{1C} is study by using the same control sample $\psi(3686) \to \pi^0\pi^0 J/\psi$. The selection criteria is the same as described in previous paragraphs. The efficiency of χ^2_{1C} requirement is ratio the number of events that with and without cut χ^2_{1C} on the low momentum π^0. The overall efficiency of χ^2_{1C} cut in π^0 momentum region [0.03, 0.24] GeV/c is $(87.71 \pm 0.33)\%$ for data and $(87.39 \pm 0.34)\%$ for signal MC. The difference of the selection efficiency is $(0.32 \pm 0.47)\%$. The conservative uncertainty of $\chi^2_{1C} < 20$ cut is 0.9%.
- The systematic uncertainty of Multiply Variable Analysis is studied by selecting

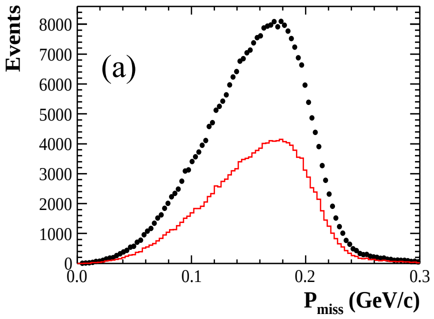

Figure 4.21 The momentum of the recoil vector of tagged π^0 and J/ψ for (a) data and (b) MC.

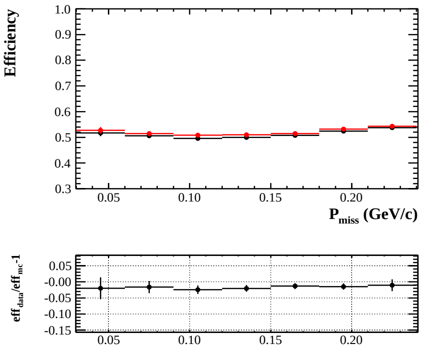

Figure 4.22 π^0 selecting efficiency in momentum region [0.03, 0.24] GeV/c in data (black) and MC(red).

$\bar{n}$ sample from control sample $J/\psi \to p^+\bar{n}\pi^-$. After selecting the most energetic shower and the matching angle of the selected shower to recoil vector of proton and pion to be less than 40 degree, the variables of $\bar{n}$ shower is used for MVA. The same classifier obtained in section 4.1.2.3 is applied for signal MC and data of control sample. The selection efficiency of classifier cut on data and MC are shown in Fig. 4.23. The overall efficiency of MVA classifier cut in $\bar{n}$ momentum region [0.03, 0.18] GeV/c is (71.19 ± 1.22)% for data and (73.20 ± 0.87)% for signal MC. The difference of selection efficiency is (2.01 ± 1.50)%. The conservative uncertainty of MVA cut is 4.8%.

- The uncertainties of fitting method are studied from three aspects: the fitting

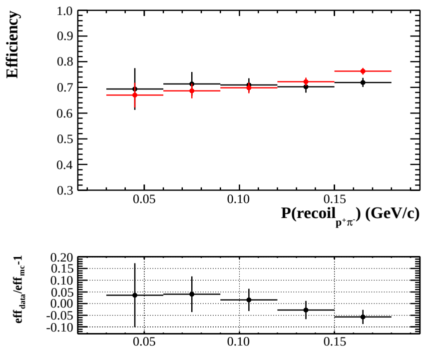

Figure 4.23 MVA classifier cut efficiency in momentum region [0.03, 0.18] GeV/c.

range, and the background shape. To study the uncertainty from fitting range, the fitting range of $p(\pi^0)$ is varied from [0.06, 0.15] GeV/c to [0.07, 0.14] GeV/c, [0.06, 0.15] GeV/c and [0.06, 0.14] GeV/c, the largest difference is taken as the uncertainty where the fitting result is shown in Fig. 4.24(a). To study the uncertainty of background shape, two sources are used to describe the background shape: $q\bar{q}$ background and separated beam background. The number of events from the two background sources are obtained from fitting. The fit result is shown in Fig. 4.24(b). We also fit the background by a first-order polynomial, and the fitting result is shown in Fig. 4.24(c).

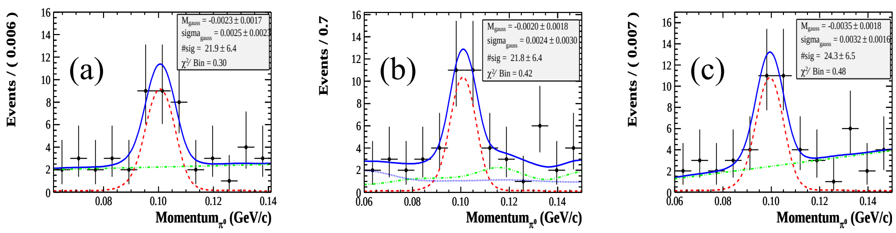

Figure 4.24 (a) fitting range varying from [0.06, 0.15] GeV/c to [0.07, 0.14] GeV/c. (b) background described by shape from $q\bar{q}$ background and separated beams. (c) background described by a first-order polynomial.

- The uncertainty of ISR correction is studied by changing the MC generator form phase space to Conexc. The input line-shape is flat from threshold to 2232.4 MeV, the energy spread is 0.48 MeV. The corresponding ISR correction factor is 0.634

and the select efficiency is 13.0%. The systematic uncertainty on ISR correction factor is 3.2%.

- The uncertainty of energy spread: In the $\psi(3686)$ scan for the data taken at $\Lambda_c\overline{\Lambda}_c$ threshold, the BEPCII energy spread is 1.6 MeV, instead of 1.3 MeV from previous scan. Here, we use 1.6 MeV to do E^2 extrapolation, the energy spread at 2232.4 MeV would be 0.59 MeV, and the corresponding correction factor is 0.603. The systematic error on the cross section measurement is 2.0%.

- In the reconstruction of $e^+e^- \to p\bar{p}$, we fit the invariant mass of $p\bar{p}$ by a single gaussian. The mean value of the center-of-mass is measured to be 2232.9 ± 0.2 MeV, which 0.5 MeV difference from the required energy, 2342.4 MeV. Therefore, we take 0.5 MeV as the uncertainty of energy scale. value, 2232.4 MeV. The ISR and energy spread correction factor at 2232.9 MeV is 0.639, which gives an uncertainty of 3.9%.

- In Ref. [5], the trigger efficiencies at BESIII are determined from J/ψ and $\psi(3686)$ data. For pure-neutral events, trigger condition is at least two shower cluster and a medium energy threshold requirement. In this analysis, at least three good showers are required. Therefore, the trigger efficiency is depending on the medium energy threshold requirement. Figure 4.25 shows the EMC trigger efficiency of medium energy threshold versus total EMC energy. Trigger efficiency is 100.0% for total deposit energy larger than 0.7 GeV. Figure 4.25 shows the total deposited energy in EMC for this analysis. There are 2.5% events with total deposited energy in [0.5, 0.7] GeV. Taking an average of trigger efficiency of such events as 70.0%, the total trigger efficiency will be $70.0\% \times 2.5\% + 100.0\% \times 97.5\% = 99.25\%$. Conservatively, the uncertainty from trigger efficiency is 1.0%.

- The uncertainty of luminosity is estimated to be 1.0% by analyzing large angle Bhabha scattering events [4].

We treat all the uncertainties uncorrelated and sum in quadrature. The uncertainties of cross section are listed in Table 4.7.

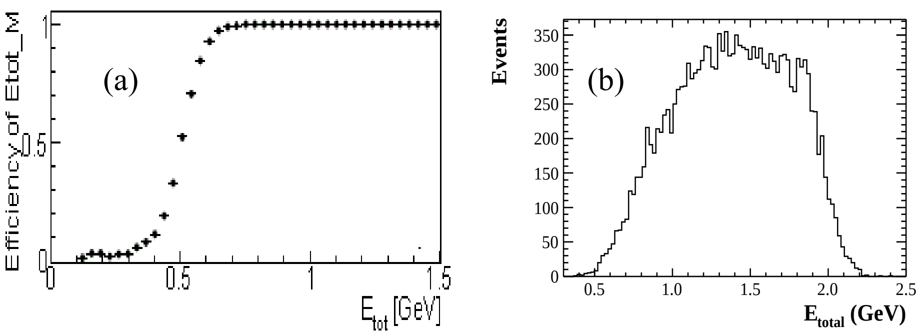

Figure 4.25 (a)Efficiency of the medium energy threshold versus total EMC energy. (b) Total EMC energy in signal MC process $e^+e^- \to \Lambda\overline{\Lambda} \to \Lambda\overline{n}\pi^0$.

Table 4.7 Summary of the uncertainties.

Systematic source	Uncertainty
$\bar{n}$ selection	2.2%
π^0 selection	2.1%
χ^2_{1C} cut	0.9%
MVA classifier cut	4.8%
Fitting range	3.9%
Background shape	7.9%
MC generator	3.2%
Energy spread	2.0%
Energy scale	3.9%
Trigger efficiency	1.0%
Luminosity	1.0%
sum	11.9%

4.1.3 Combined Result

The weighted least squares method is used to calculate the combined result for $\sigma(e^+e^- \to \Lambda\overline{\Lambda})$. The weighted average measurement value and the corresponding error can be written as:

$$\overline{x} \pm \delta\overline{x} = \frac{\sum_j x_j \cdot \sum_i \omega_{ij}}{\sum_i \sum_j \omega_{ij}} \pm \sqrt{\frac{1}{\sum_i \sum_j \omega_{ij}}}, \tag{4.9}$$

where ω_{ij} is the element of V^{-1} and the covariance error matrix V is:

$$V = \begin{pmatrix} \sigma_{T1}^2 & Cov(x_1, x_2) & ... & Cov(x_1, x_n) \\ Cov(x_2, x_1) & \sigma_{T2}^2 & ... & Cov(x_2, x_n) \\ ... & ... & ... & ... \\ Cov(x_n, x_1) & Cov(x_n, x_2) & ... & \sigma_{Tn}^2), \end{pmatrix} \tag{4.10}$$

$$\sigma_{Ti}^2 = \sigma_i^2(stat.) + \sigma_i^2(sys1.) + \sigma_i^2(sys2.) + ..., \tag{4.11}$$

$$Cov(x_i, x_j) = x_i \cdot \epsilon_{ij} \cdot x_j \cdot \epsilon_{ji}. \tag{4.12}$$

where σ_{Ti} stands for the total uncertainty in the measurement mode i, and $\sigma_i(stat.)$ and $\sigma_j(sysj.)$ are the statistical error and the systematic error for the source j in the measurement mode i respectively. $Cov(x_i, x_j)$ is the covariance systematical error between measurement mode i and j. x_i is the measured value in the measurement mode i, and $\epsilon_{ij} = \epsilon_{ji}$ is the common relative systematic error (in percentage) between mode i and j.

In case of two measurements, σ_{Ti} and $Cov(x_i, x_j)$ can be written as:

$$\sigma_{Ti}^2 = \sigma_i^2(stat.) + \sigma_i^2(sys1.) + \sigma_i^2(sys2.) + ... = \sigma_i^2 + x_i^2 \cdot \epsilon_f^2, \tag{4.13}$$

$$Cov(x_i, x_j) = x_i \cdot \epsilon_{ij} \cdot x_j \cdot \epsilon_{ji} = x_i \cdot x_j \cdot \epsilon_f \cdot \epsilon_f, \tag{4.14}$$

where σ_i is the independent error in the measurement mode i, including statistic error and independent systematic errors, and ϵ_f is the common relative systematic error between the two measurements. The corresponding covariance error matrix V is:

$$V = \begin{pmatrix} \sigma_1^2 + \epsilon_f^2 x_1^2 & \epsilon_f^2 x_1 x_2 \\ \epsilon_f^2 x_1 x_2 & \sigma_2^2 + \epsilon_f^2 x_2^2 \end{pmatrix}, \tag{4.15}$$

The weighted average measured value and the corresponding error are:

$$x = \frac{x_1\sigma_2^2 + x_2\sigma_1^2}{\sigma_1^2 + \sigma_2^2 + (x_1 - x_2)^2\epsilon_f^2}, \tag{4.16}$$

$$\sigma^2(x) = \frac{\sigma_1^2\sigma_2^2 + (x_1\sigma_2^2 + x_2\sigma_1^2)\epsilon_f^2}{\sigma_1^2 + \sigma_2^2 + (x_1 - x_2)^2\epsilon_f^2}. \tag{4.17}$$

In our analysis, the common systematic sources are uncertainty from MC generator, energy spread, energy scale and luminosity, which takes 5.5%. The combined result is calculated to be 319.5 ± 57.6 pb where the uncertainty is the square of statistical and systematic errors.

4.2 Measurement of $e^+e^- \to \Lambda\overline{\Lambda}$ at 2400.0, 2800.0 and 3080.0 MeV

4.2.1 Event Selection

Following are the event selection of reconstruction of $\Lambda\overline{\Lambda}$:

- A good track should satisfy $|V_r| < 30$ cm, $|V_z| < 10$ cm and $|\cos\theta| < 0.93$. For one event, at least four good charged tracks is required.

- The combined information of dE/dx and TOF is used to calculate the particle identification (PID) probabilities of a pion, kaon or proton hypothesis, respectively. The particle type with the highest probability is assigned to the track. In this analysis, one proton antiproton pair and one pion ($\pi^+\pi^-$) pair are required.

- $\Lambda(\overline{\Lambda})$ candidates are reconstructed with proton and pion tracks. The secondary vertex fit is performed and the track parameters are used to get the invariant mass $M_{p\pi^-}(M_{\bar{p}\pi^+})$. Figure 4.26 shows the ratio of decay length over its standard deviation. Good agreements can be observed between data and MC. The mass window cuts $|M_\Lambda - 1.115| < 0.01$ GeV for both Λ and $\overline{\Lambda}$ candidates are further applied as shown in Fig. 4.27.

- The distributions of opening angle between Λ and $\overline{\Lambda}$ in center-of-mass system are shown in Fig. 4.28. The c.m. energy dependent requirements, $\theta_{\Lambda\overline{\Lambda}} > 170°$ at 2.40 GeV, $\theta_{\Lambda\overline{\Lambda}} > 176°$ at 2.80 GeV, and $\theta_{\Lambda\overline{\Lambda}} > 178°$ at 3.08 GeV are further applied,

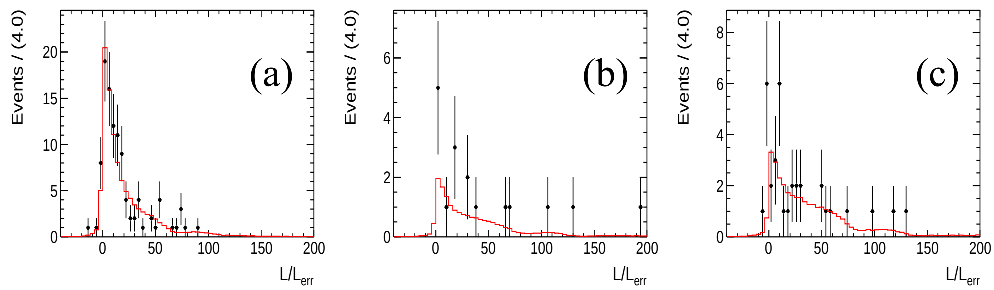

Figure 4.26 Ratio of decay length over its standard deviation at (a) 2.40 GeV, (b) 2.80 GeV and (c) 3.08 GeV.

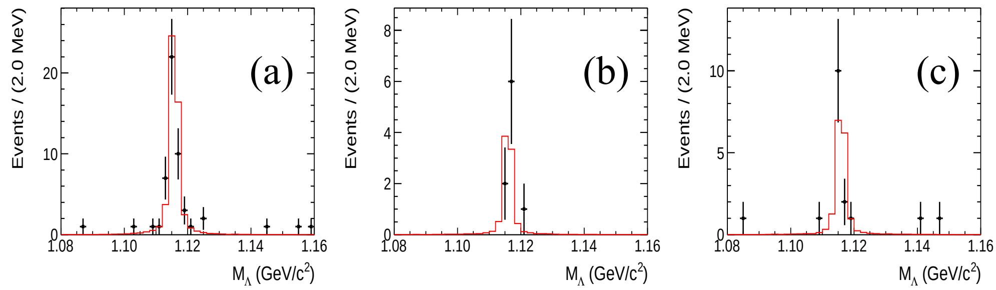

Figure 4.27 The invariant mass distribution of M_{Λ} at (a) 2.40 GeV, (b) 2.80 GeV and (c) 3.08 GeV.

since at higher c.m.energies, the background channel such as $e^{+}e^{-} \to \Sigma^{0}\overline{\Sigma^{0}}$, $e^{+}e^{-} \to \Xi^{0}\overline{\Xi^{0}}$ and $e^{+}e^{-} \to \Sigma^{0}\overline{\Lambda} + c.c$ will contaminate event in data.

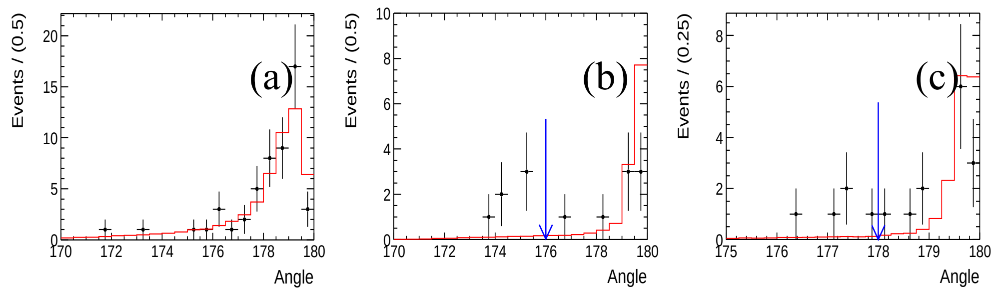

Figure 4.28 The distributions of opening angle between Λ and $\overline{\Lambda}$ in center-of-mass system at (a) 2.40 GeV, (b) 2.80 GeV and (c) 3.08 GeV.

- Figure 4.29 shows the momentum distribution of Λ and $\overline{\Lambda}$. Good agreements are observed between data and MC. Figure 4.30 shows the comparisons of the ratio of the $\Lambda\overline{\Lambda}$ invariant mass to c.m. energy, $M_{\Lambda\overline{\Lambda}}/E_{cm}$, between data and MC. The signal yields are extracted by the number counting method.

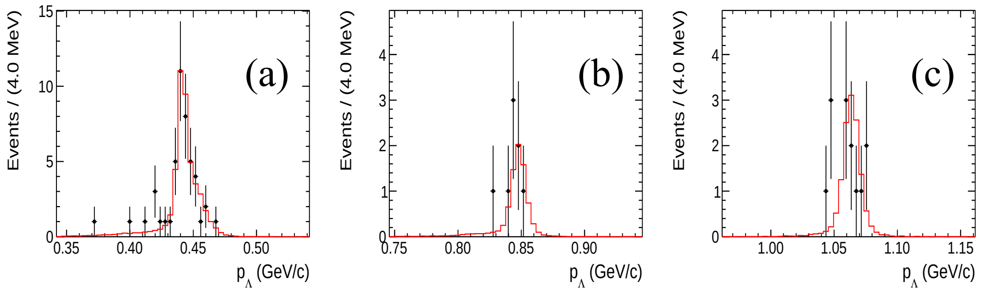

Figure 4.29 The momentum distribution of Λ at (a) 2.40 GeV, (b) 2.80 GeV and (c) 3.08 GeV.

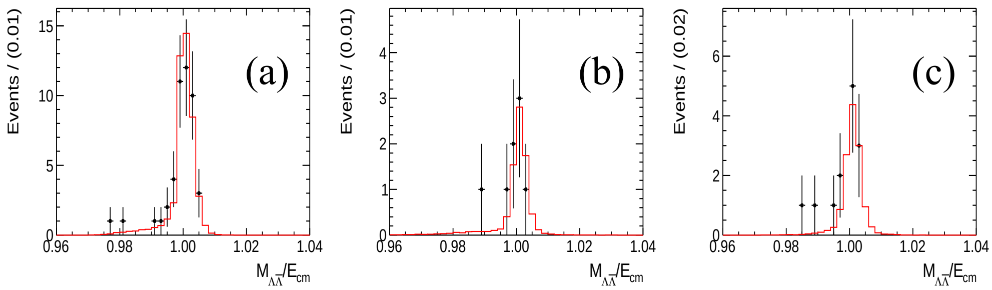

Figure 4.30 The ratio of the $\Lambda\overline{\Lambda}$ invariant mass to c.m. energy, $M_{\Lambda\overline{\Lambda}}/E_{cm}$ at (a) 2.40 GeV, (b) 2.80 GeV and (c) 3.08 GeV.

4.2.2 Background Analysis

The background of the $e^+e^- \to \Lambda\overline{\Lambda}$ channel either comes from non-M_Λ background or M_Λ peaking background.

The non-M_Λ background is studied from two dimensional sideband of M_Λ and $M_{\overline{\Lambda}}$ as shown in Fig. 4.31. The red boxes denote the signal region $|M_\Lambda - 1.115| < 0.01$ GeV and $|M_{\overline{\Lambda}} - 1.115| < 0.01$ GeV. The blue boxes denote the sideband region $1.084 < M_\Lambda < 1.104$ GeV or $1.084 < M_{\overline{\Lambda}} < 1.104$ GeV. The green boxes denote the corner region $1.084 < M_\Lambda < 1.104$ GeV and $1.084 < M_{\overline{\Lambda}} < 1.104$ GeV. The number of the non-M_Λ background is estimated by the number of events in sideband region minus the number the events in corner region.

The M_Λ peaking background is studied from exclusive background analysis. The possible peaking background is listed in Table 4.8. The contribution of the FSR amplitude is $d\sigma/dm \simeq |F|^2 8m\alpha^3\beta/(27s^2)$ which is proportional to α^3. The cross section of the baryon pair production is from reference [6] [2]. By simulating 40k number of events

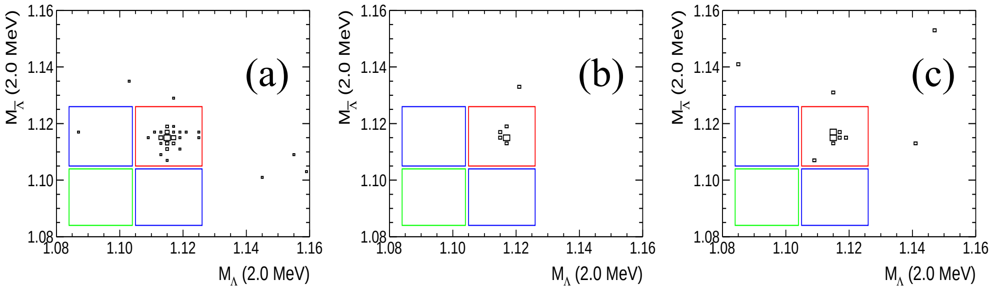

Figure 4.31 Two dimensional distribution of the momentum of Λ versus $\bar{\Lambda}$ at (a) 2.40 GeV, (b) 2.80 GeV and (c) 3.08 GeV.

for each background channel at each c.m. energy, the efficiency of the background channel passing above selection criteria is obtained. And the normalized background event contaminated in signal is calculated which found to be negligible.

Table 4.8 Summary of the peaking background.

	$\sqrt{s} = 2400.0$ MeV			$\sqrt{s} = 2800.0$ MeV			$\sqrt{s} = 3080.0$ MeV		
Source	ϵ_{sel}^{MC}	σ (pb)	N_{nor}^{MC}	ϵ_{sel}^{MC}	σ (pb)	N_{nor}^{MC}	ϵ_{sel}^{MC}	σ (pb)	N_{nor}^{MC}
$e^+e^- \to \gamma_{FSR}\Lambda\bar{\Lambda}$	1.6%	< 1.3	0.1	0.5%	< 0.16	0	0.2%	< 0.04	0
$e^+e^- \to \Sigma^0\bar{\Sigma}^0$	0	30	0	0.2%	17	0.1	0.2%	3.4	0.2
$e^+e^- \to \Lambda\bar{\Sigma}^0$		32	-		2.9			< 8.7	
$e^+e^- \to \Xi^0\bar{\Xi}^0$				0	-	0	0	-	0
Sum			0.1			0.1			0.2

4.2.3 Calculation of Born Cross Section and Effective FF

The Born cross section of $e^+e^- \to \Lambda\bar{\Lambda}$ is calculated by

$$\sigma_{Born}(e^+e^- \to \Lambda\bar{\Lambda}) = \frac{N_{sig} - N_{bkg}}{L \cdot \varepsilon \cdot (1+\delta) \cdot Br(\Lambda \to p\pi^-) \cdot Br(\bar{\Lambda} \to \bar{p}\pi^+)}, \tag{4.18}$$

where N_{sig} is the observed number of candidate events, extracted by counting the number of signal events, N_{bkg} is the expected number of background events from non-M_Λ and M_Λ peaking background, L is the integrated luminosity estimated with the large angle Bhabha events, ε is the detection efficiency determined from a MC sample generated using the Conexc generator, which includes radiative corrections, and $(1+\delta)$ is the radiative correction factor which has also been determined using the Conexc generator. Since the detection efficiency depends on the angular distribution of production baryon. In this analysis, the detection efficiency is evaluated with the MC samples by sampling the baryon angular with $(1+\cos^2\theta)$ and $(1-\cos^2\theta)$. The nominal detection efficiency is the average of the efficiencies. Table 4.9 summarized the derived Bron cross section σ_{Born} and the related variables, where ε_1 is the detection efficiency with baryon angular $(1+\cos^2\theta)$. ε_2 is the detection efficiency with baryon angular $(1-\cos^2\theta)$. $\overline{\varepsilon}$ is the average detection efficiency.

Table 4.9 Summary of the Born cross section σ_{Born} and effective FF $|G|$ at different c.m. energies $\sqrt{s}$.

$\sqrt{s}$ (GeV)	N_{sig}	N_{bkg}	L (pb^{-1})	$\varepsilon_1(\%)$	$\varepsilon_2(\%)$	$\overline{\varepsilon}(\%)$	$(1+\delta)$	σ_{Born} (pb)	$\|G\|(\times10^{-2})$
2.40	46 ± 7	1	3.42	21.64	28.22	24.93	0.97	133±20	12.93 ± 0.97
2.80	8 ± 3	0	3.75	22.68	28.22	25.45	1.34	15.3±5.4	4.16 ± 0.73
3.08	13 ± 4	0	30.73	16.09	20.26	18.18	1.48	3.9±1.1	2.21 ± 0.31

By assuming the electric and magnetic FFs to be equal, $|G| = |G_E| = |G_M|$, Eq. 4.1 can be rewrited into:

$$\sigma_{Born} = \frac{4\pi\alpha^2 C\beta}{3m^2}[1+\frac{1}{2\tau}]|G|^2, \tag{4.19}$$

where the Coulomb factor C equals to 1 for neutral baryon pairs. The effective FF can be deduced into:

$$|G| = \sqrt{\frac{3m^2}{4\pi\alpha^2\beta}\frac{\sigma_{Born}}{1+\frac{1}{2\tau}}}. \tag{4.20}$$

The effective FF $|G|$ for each c. m. energy are shown in Table 4.9, too.

4.2.4 Systematic Uncertainty

- To study the uncertainty of Λ efficiency, the sample of Λ is selected from control sample of $J/\psi \to pK^-\Lambda + c.c.$ The good charged track should satisfy $|V_r| < 1$ cm, $|V_z| < 10$ cm and $|\cos\theta| < 0.93$. For one event, at least two good charged tracks are required. Particle identification is applied by combing the information of dE/dx and TOF, and one positive proton and one negative kaon are required. Missing one $\overline{\Lambda}$, a 1C kinematic fit is performed on the proton and kaon, and χ^2_{1C} is required to be less than 10. And the invariant mass of the recoiled vector of proton and kaon is required to be in [1.07, 1.17] GeV. After the selection, the purity of sample is 93.9% from the topology of inclusive MC. No peaking background is observed in the invariant mass of the recoiled vector of proton and kaon. The number of observed events in sample, denoted as N_{sample}, is obtained by fitting the invariant mass of recoil vector of proton and kaon by MC shape convoluted with Gaussian function and a flat background described by polynomials.

To reconstruction $\overline{\Lambda}$ from $\bar{p}\pi^+$, two additional charged tracks are selected, where the charged track should satisfy $|V_r| < 10$ cm, $|V_z| < 30$ cm, and $|\cos\theta| < 0.93$. With particle identification, one antiproton and positive pion are required. A second vertex fit is applied for proton and pion. The above selection criteria of $\overline{\Lambda}$ is the same as in section 4.2.1. The number of reconstructed $\overline{\Lambda}$ is denoted as $N_{\overline{\Lambda}}$, by fitting the invariant mass of recoil vector of proton and kaon after the above selection criteria applied.

Figure 4.32 shows the efficiency of $\overline{\Lambda}(\Lambda)$ reconstruction versus different momentum of $\overline{\Lambda}(\Lambda)$. The overall reconstruction efficiency of $\overline{\Lambda}$ is $(32.8 \pm 0.1)\%$ for data and $(33.9 \pm 0.1)\%$ for MC. The overall reconstruction efficiency of Λ is $(36.4 \pm 0.1)\%$ for data and $(35.0 \pm 0.1)\%$ for MC. Therefore, the systematic reconstruction efficiency is 3.4% for $\overline{\Lambda}$ and 3.8% for Λ.

- The uncertainty of mass window requirement on Λ and $\overline{\Lambda}$ is studied from the control sample of $J/\psi \to pK^-\Lambda + c.c.$ After select the $\Lambda/\overline{\Lambda}$ sample, a mass window cut is applied on MC and data. The efficiency of mass window cut $|M_\Lambda - 1.115| < 0.01$ GeV is 96.0% and 93.67% for MC and data, respectively. The efficiency of mass window cut $|M_{\overline{\Lambda}} - 1.115| < 0.01$ GeV is 96.01% and 93.25% for MC and data, respectively. The uncertainty of mass window cut is 2.49% for Λ and 2.96% for $\overline{\Lambda}$.

- The uncertainty of the baryon angular distribution is evaluated to be half of the

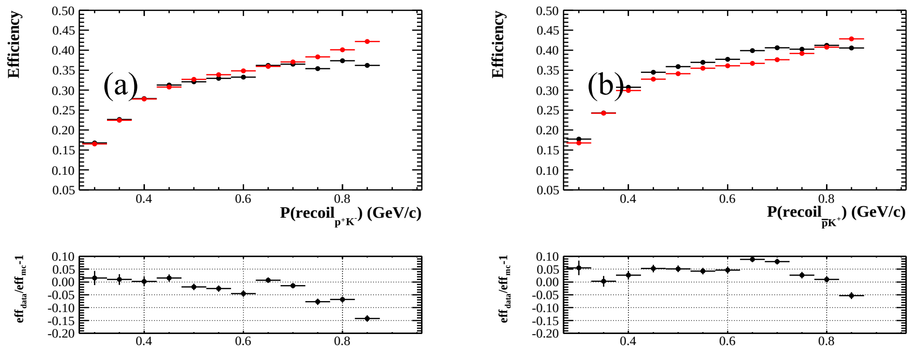

Figure 4.32 Reconstruction efficiency for (a) $\overline{\Lambda}$ and (b) Λ.

differences between the detection efficiency with angular distribution to be $(1 + \cos^2\theta)$ and $(1 - \cos^2\theta)$ as shown in Table 4.9. The uncertainty of angular distribution is 12.65%, 10.81%, and 11.35% for 2.40, 2.80 and 3.08 GeV, respectively. The uncertainty of angular distribution is the largest contribution to the total uncertainty. With the new scan data at BEPCII, which the luminosity will be higher, the angular distribution of Λ can be parameterised and the uncertainty due to angular distribution will be significantly improved.

- Different input lineshape would influence the detection efficiency as well as the ISR correction factor. Since in previous measurement, the lineshape of $\Lambda\overline{\Lambda}$ production is poorly known , there may have very different lineshape for this process. In this analysis, we apply different lineshapes to obtain the product value of detection efficiency and ISR correction factor. The input lineshape is shown in Fig. 4.33. And the difference for the product value and ISR correction factor for two two lineshape is 0.85%, 4.34% and 1.75% for 2.40, 2.80 and 3.08 GeV, respectively.

- The integrated luminosity is measured by analyzing large-angle Bhabha scattering process, and achieve 1.0% in precision.

All systematic uncertainties are summarized in Table 5.5. The total systematic uncertainty of the Born cross section is obtained by summing the individual contributions in quadrature.

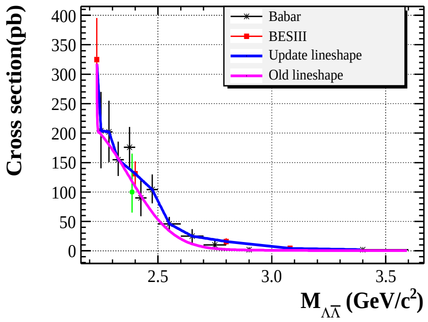

Figure 4.33 The lineshape of $e^+e^- \to \Lambda\overline{\Lambda}$.

Table 4.10 Summary of systematic uncertainties (in %) for the Born cross section σ_{Born}.

Source	2400.0 MeV	2800.0 MeV	3080.0 MeV
Reconstruction of Λ	3.8	3.8	3.8
Reconstruction of $\overline{\Lambda}$	3.4	3.4	3.4
Mass window cut of Λ	2.5	2.5	2.5
Mass window cut of $\overline{\Lambda}$	3.0	3.0	3.0
Angular distribution	12.7	10.8	11.4
Input lineshape	0.9	4.3	1.8
Luminosity	1.0	1.0	1.0
Total	14.3	13.3	13.2

4.3 Conclusion and Discussion

In this analysis, the process of $e^+e^- \to \Lambda\overline{\Lambda}$ near $\Lambda\overline{\Lambda}$ production threshold, 2232.4 MeV, is studied using a 2.63 pb^{-1} data sample. The measurement of cross section of $e^+e^- \to \Lambda\overline{\Lambda}$ by reconstructing $\Lambda/\overline{\Lambda}$ from charged channel and neutral channel give consistent results, which are 324.6 $\pm$ 52.8(stat) $\pm$ 46.4(syst) pb and 306.6 $\pm$ 103.5(stat) $\pm$ 36.5(syst) pb, respectively. The combined result is 319.5 ± 57.6 pb.

The result contradicts the theoretical prediction from Eq.5.1, which implies that the cross section should be almost vanishing at 2232.4 MeV. When taking into account the energy spread, the observed cross section measurement is much larger than the prediction. This result strongly suggests that something more is at play here beyond the expected phase space behavior. It has been speculated that a Coulomb interaction at the constituent quark level could explain this enhancement [3].

Besides the measurement of $e^+e^- \to \Lambda\overline{\Lambda}$ near threshold, we also measured the cross section $e^+e^- \to \Lambda\overline{\Lambda}$ at 2400.0, 2800.0, 3080.0 MeV by reconstructing $\Lambda \to p\pi^-$, $\overline{\Lambda} \to \bar{p}\pi^+$. The results are summarized in Table 4.11. The first uncertainties are statistical, and the second are systematic. For the combined cross section, the uncertainty is the combined uncertainty. Figure 4.344.35 shows comparison of the cross section between our measurement with previous measurements. Good consistence and better precision are achieved in this analysis.

Table 4.11 The Born cross section of $e^+e^- \to \Lambda\overline{\Lambda}$, σ_{Born}.

$\sqrt{s}$ MeV	Reconstruction	σ_{Born} (pb)	$\lvert G\rvert$ ($\times 10^{-2}$)
2232.4	$\Lambda \to p\pi^-, \overline{\Lambda} \to \bar{p}\pi^+$	$325 \pm 53 \pm 46$	
	$\overline{\Lambda} \to \bar{n}\pi^0$	$(3.0 \pm 1.0 \pm 0.4) \times 10^2$	
	combined	320 ± 58	63.4 ± 5.7
2400.0		$133 \pm 20 \pm 19$	$12.93 \pm 0.97 \pm 0.92$
2800.0		$15.3 \pm 5.4 \pm 2.0$	$4.16 \pm 0.73 \pm 0.27$
3080.0		$3.9 \pm 1.1 \pm 0.5$	$2.21 \pm 0.31 \pm 0.14$

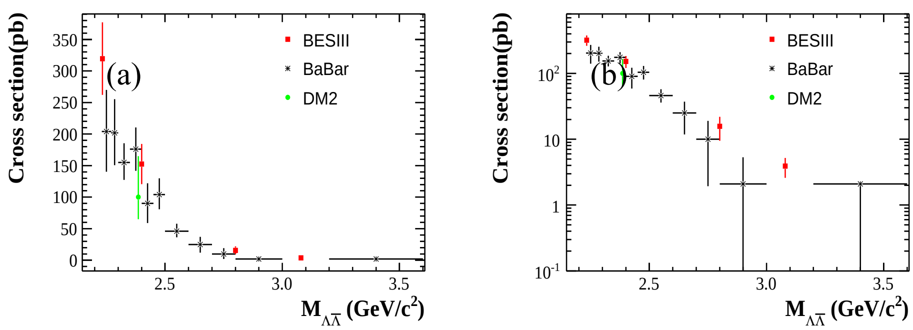

Figure 4.34 Comparison of the results for $\Lambda\overline{\Lambda}$ masses from 2.0 to 3.6 GeV shown on a normal scale (a) and a logarithmic scale (b).

Bibliography

[1] J. Schwinger, *Particle, Sources, and Fields*, Perseus Books Publishing, Massachusetts, 1998, Vol.3.

[2] B. Aubert *et al.* (BaBar Collaboration), Study of $e^+e^- \to \Lambda\bar{\Lambda}$, $\Lambda\bar{\Sigma}^0$, $\Sigma^0\bar{\Sigma}^0$ using initial state radiation with BABAR. Phys. Rev. D **76**, 092006 (2007).

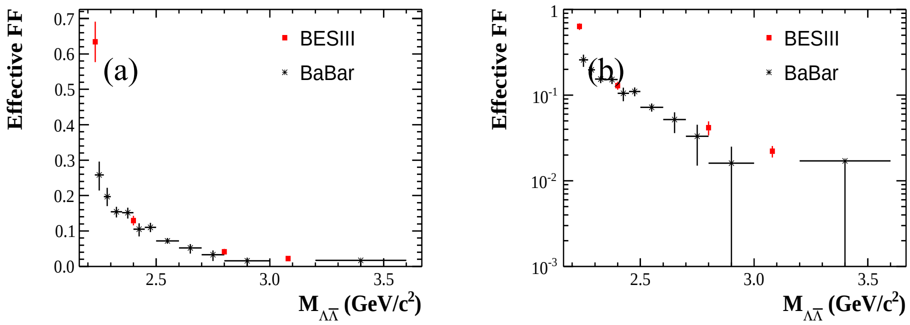

Figure 4.35 Comparison of cross section for $\Lambda\bar{\Lambda}$ masses from 2.0 to 3.6 GeV shown on a normal scale (a) and a logarithmic scale (b).

[3] R. Baldini, S. Pacetti, A. Zallo and A. Zichichi, Unexpected features of $e^+e^- \to p\bar{p}$ and $e^+e^- \to \Lambda\bar{\Lambda}$ cross section near threshold. Eur. Phys. J. A 39, 315 (2009) [arXiv:0711.1725 [hep-ph]].

[4] Zhen Gao, ”Measurement of the integrated luminosities of the data for R-scan at BESIII”, BAM-00157.

[5] N. Berger, K. Zhu, Z. -A. Liu, D. -P. Jin, H. Xu, W. -X. Gong, K. Wang and G. -F. Cao, Trigger efficiencies at BESIII. Chin. Phys. C **34**, 1779 (2010).

[6] D. Bisello *et al.* [DM2 Collaboration], Baryon pair production in e^+e^- annihilation at $\sqrt{s}$ =2.4 GeV. Z. Phys. C **48**, 23 (1990).

Chapter 5

Observation of $J/\psi \to p\bar{p}a_0(980)$

As described in Sec.1.1.2, due to the asymptotic-free nature of QCD, perturbation theory can only be applied at short distances. However, at low-energy region, the growing of the running QCD coupling and the associated confinement of quarks and gluons make it very difficult to perform pQCD. This allowes the development of effective field theory. A chiral unitary coupled channels approach of the Chiral perturbation theory (ChPT) [1–3] is applied in investigation of the four-body decays $J/\psi \to N\bar{N}MM$ process [4] where the N stands for a baryon and the M for a meson. In this approach, the process $J/\psi \to p\bar{p}\pi^0\eta$ is investigated with the $a_0(980)$ meson generated through final state interaction (FSI). The amplitude of this process is calculable except for some coefficients which are not restricted, and its branching fraction varies within a wide range for different coefficients. Therefore, an experimental measurement of the process $J/\psi \to p\bar{p}a_0(980) \to p\bar{p}\pi^0\eta$ is needed for further progress in understanding of the dynamics of the four-body decay processes taking the FSI of mesons into account.

As one of the low-lying scalars, the state $a_0(980)$ has turned out to be mysterious in the quark model scenario. Its production near threshold allows tests of various hypotheses for its structure, including quark-antiquark [5], four quarks [6], $K\bar{K}$ molecule [7] and hybrid states [8]. The measurement of $J/\psi \to p\bar{p}a_0(980)$ is an additional observable constraining any phenomenological models trying to understand the nature of the $a_0(980)$.

In this chapter, we present a measurement of $J/\psi \to p\bar{p}a_0(980)$ with $a_0(980)$

decaying to $\pi^0\eta$ based on 2.25×10^8 J/ψ events [9] collected with the BESIII detector at BEPCII.

In this analysis, the J/ψ resonance is generated by kkmc [10] which is the event generator based on precise predictions of the Electroweak Standard Model for the process $e^+e^- \to f\bar{f} + n\gamma$, where $f = e,\ \mu,\ \tau,\ u,\ d,\ c,\ s,\ b$ and n is an integer number ≥ 0. The subsequent decays are generated with EvtGen [11] with branching fractions being set to the world average values according to the Particle Data Group (PDG) [12] and the remaining unmeasured decays are generated by Lundcharm [13]. A sample of 2.25×10^8 simulated events, corresponding to the luminosity of data, is used to study background processes from J/ψ decays ('inclusive backgrounds'). A signal MC sample with more than 10 times of the observed events in data for the process $J/\psi \to p\bar{p}a_0(980) \to p\bar{p}\pi^0\eta$ is generated, where the shape of the $a_0(980)$ is parameterized with the Flatté formula [14].

5.1 Analysis Strategy

5.1.1 Event Selection

We select the process $J/\psi \to p\bar{p}\pi^0\eta$, with both π^0 and η decaying to two photons, for this analysis.

A good charged track is required to have good quality in the track fitting and be within the polar angle coverage of the MDC, i.e., $|\cos\theta| < 0.93$, and pass within 1 cm of the e^+e^- interaction point in the transverse direction to the beam line and within 10 cm of the interaction point along the beam axis. Fig. 5.1 shows the comparison of the distributions of related variables between data and inclusive MC. The dots with error bars represent data and the histogram represent inclusive MC.

Since the charged track in this process has relatively low transverse momentum, charged particle identification (PID) is only based on the dE/dx information with the confidence level $\mathrm{Prob_{PID}}$(i) calculated for each particle hypothesis i ($i = \pi/K/p$). A charged track with $\mathrm{Prob_{PID}}$(p)>$\mathrm{Prob_{PID}}(K)$ and $\mathrm{Prob_{PID}}$(p)>$\mathrm{Prob_{PID}}(\pi)$ is identified as a proton or an antiproton candidate.

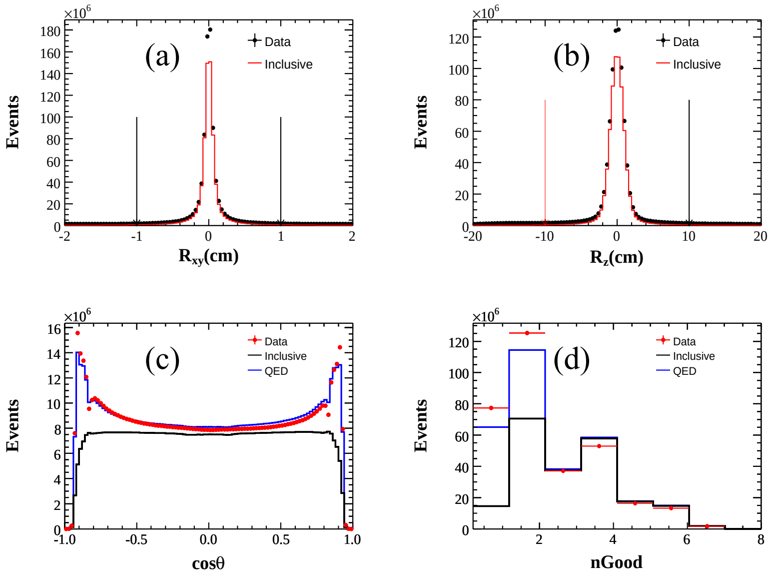

Figure 5.1 Comparison of several distributions for charged tracks.

Photon candidates are required to have a minimum energy deposition of 25 MeV in the barrel ($|\cos\theta|$ <0.8) of the EMC and 50 MeV in the end caps (0.86< $|\cos\theta|$ <0.92) of the EMC. EMC timing requirements ($0 \leq T \leq 14$ in units of 50 ns) are used to suppress electronic noise and to remove showers unrelated to the event. At the event selection level, candidate events are required to have at least two good charged tracks with one proton and one antiproton being identified, and at least four good photons.

We then perform a kinematic fit which imposes energy and momentum conservation at the production vertex to combinations of one proton and one antiproton candidate and four photons. For events with more than four photons, we consider all possible four-photon combinations, and the one giving the smallest χ^2_{4C} for the kinematic fit is selected for further analysis. To improve the signal-to-background ratio, events with χ^2_{4C} <35 are accepted; this optimizes the figure of merit $S/\sqrt{S+B}$, where S and B are the numbers of MC simulated signal and inclusive background events respectively.

The best photons pairing to π^0 and η in the four selected photons are selected by

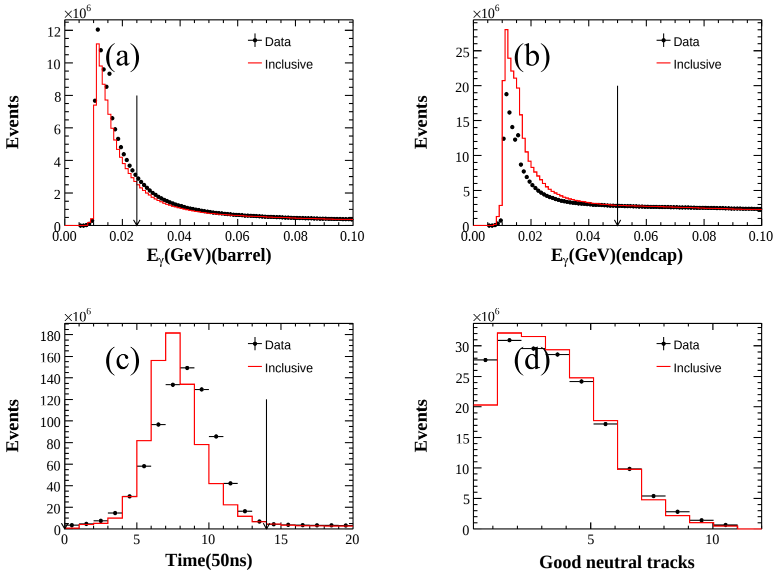

Figure 5.2 Comparison of several distributions for neutral tracks.

choosing the combination that gives the minimum χ^2-like variable

$$\chi^2_{\pi^0\eta} = \frac{(M_{\gamma_1\gamma_2} - M_{\pi^0})^2}{\sigma^2_{\pi^0}} + \frac{(M_{\gamma_3\gamma_4} - M_\eta)^2}{\sigma^2_\eta},$$

where $M_{\gamma\gamma}$ is the invariant mass of two photons after kinematic fit and $M_{\pi^0/\eta}$ is the π^0/η mass from PDG [12]. The mass resolutions for the π^0 and η, σ_{π^0} and σ_η are extracted by fitting the corresponding mass spectra in the signal MC sample as shown in Fig. 5.4. The resolution of π^0 is

$$\sigma_{M_{\pi^0}} = \sqrt{\sigma_1^2 \times f + \sigma_2^2 \times (1-f)} = 5.98MeV/c^2,$$

and the resolution of η is

$$\sigma_{M_{\eta^0}} = \sqrt{\sigma_1^2 \times f + \sigma_2^2 \times (1-f)} = 9.75MeV/c^2.$$

A MC study shows the rate of correct combination of photons is greater than 99% by using the $\chi^2_{\pi^0\eta}$ metric by matching the truth π^0/η with reconstructed π^0/η, and requiring the matching angle less than 20°. Further detail study shows that the mostly wrong

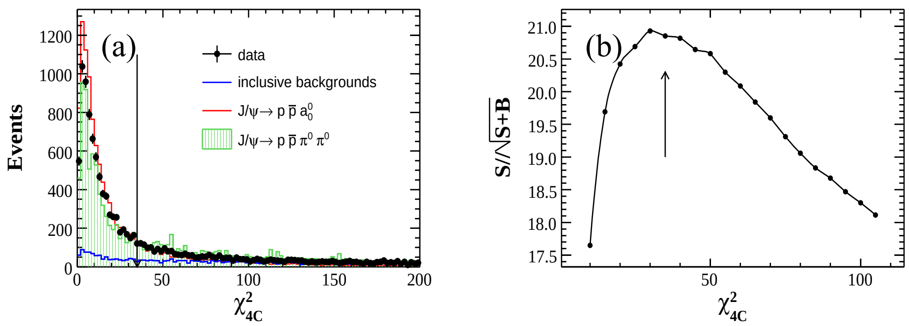

Figure 5.3 (a) Comparison of χ^2 distributions. (b) The signal to background ratio defined as $\frac{S}{\sqrt{(S+B)}}$.

combination events are due to the fake photon.

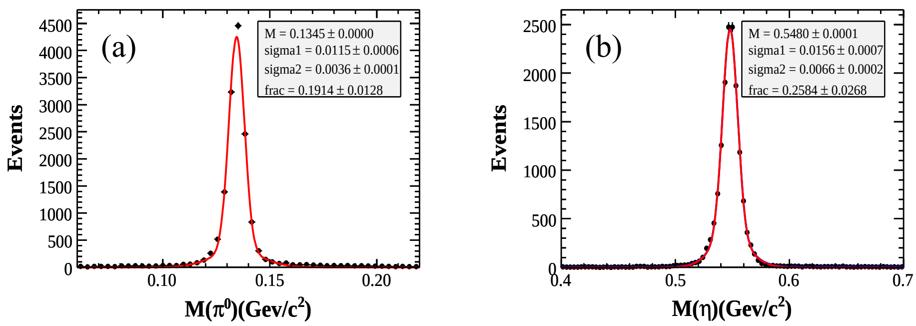

Figure 5.4 (a) π^0 and (b) η mass spectrum from signal MC and fitted with Double-Gaussian function.

To suppress $p\bar{p}\pi^0\pi^0$ final states surviving in the 4C fit, we select two-photon pairs giving a minimum $\chi^2_{\pi^0\pi^0} = \frac{(M_{\gamma_1\gamma_2} - M_{\pi^0})^2}{\sigma^2_{\pi^0}} + \frac{(M_{\gamma_3\gamma_4} - M_{\pi^0})^2}{\sigma^2_{\pi^0}}$ and reject events with $\chi^2_{\pi^0\pi^0}$ less than 100. The requirement removes 17.32% background events while losing 0.91% signal events. Fig. 5.18 shows the comparison of distribution of $\chi^2_{\pi^0\pi^0}$ for data, inclusive MC, signal channel and $J/\psi \to p\bar{p}\pi^0\pi^0$ channel.

Figure 5.6 shows the mass spectra of selected $\gamma\gamma$ pairs for data and MC, where $\gamma_1\gamma_2$ indicates π^0 candidates and $\gamma_3\gamma_4$ indicates η candidates. The hatched histograms represent MC shapes from backgrounds and signal, where the background shapes are

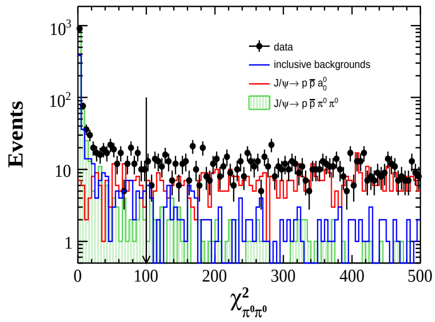

Figure 5.5 The comparison of the distribution $\chi^2_{\pi^0\pi^0}$, plotted in log-scale.

normalized based on their branching fractions and the signal shape is normalized to the rest area of the histogram of the data. We then require the mass of π^0 and η candidates to be within a 3σ window around their mean values.

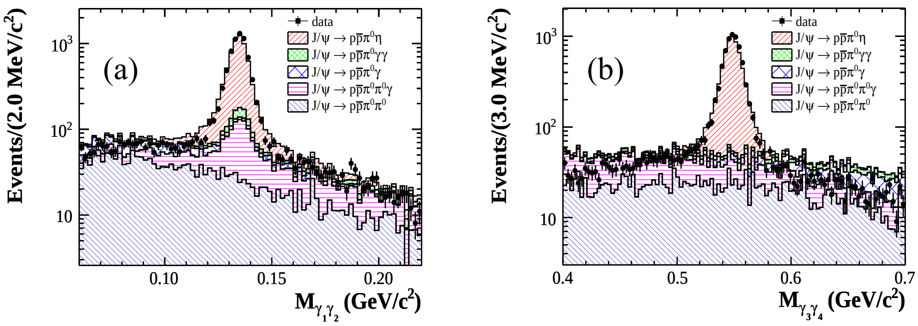

Figure 5.6 The invariant mass distribution of (a) π^0 candidates and (b) η candidates.

5.1.2 Background Analysis

The backgrounds contaminating the selected $J/\psi \to p\bar{p}\pi^0\eta$ candidates arise mainly from events with the same topology ($p\bar{p}\gamma\gamma\gamma\gamma$), events with an additional undetected photon ($p\bar{p}\gamma\gamma\gamma\gamma\gamma$), and events with a fake photon being reconstructed ($p\bar{p}\gamma\gamma\gamma$). The potential final states of background are categorized into four kinds: $p\bar{p}\pi^0\pi^0$, $p\bar{p}\pi^0\pi^0\gamma$, $p\bar{p}\pi^0\gamma$ and $p\bar{p}\pi^0\gamma\gamma$, where the $p\pi^0$ can be produced from intermediate states Σ or Δ, and $\gamma\pi^0$ can be produced from ω.

Since the branching fractions for the exclusive background processes $J/\psi \to \Sigma^+\Sigma^-(\gamma)/\Delta^+\Delta^-(\gamma)/p\bar{p}\omega(n\gamma)$ have not yet been measured, we determine them from the same J/ψ data sample. The measurements are performed by requiring different numbers of photon candidates in one event and selecting the combination of $p\pi^0$ with invariant mass closest to the mass of Σ or Δ, or selecting the combination of $\gamma\pi^0$ closest to the mass of ω. The measured branching fractions are shown in Table 5.1, , where Br is the branching fraction of each channel, with statistical error only, ε^{sel}_{MC} is the selected efficiency of each channel determined with 50k MC sample, and N^{Norm} is the number of background events normalized to the total J/ψ data. With the detection efficiency correction for the exclusive background satisfying the $p\bar{p}\pi^0\eta$ selection criteria, the contribution of the exclusive backgrounds is calculated to be 290 ± 19, which accounts for 4.3% of the surviving events found in data.

The distributions of $M_{\pi^0\eta}$ for data and backgrounds after normalization are presented in Fig. 5.7. A structure around 1.0 GeV (Fig. 5.7(a)) in data is clearly visible, but is not seen significantly in the corresponding distribution of the exclusive backgrounds (Fig. 5.7(b)).

Table 5.1 Backgrounds of the final states with $p\bar{p}\pi^0\pi^0$, $p\bar{p}\pi^0\pi^0\gamma$, $p\bar{p}\pi^0\gamma$ and $p\bar{p}\pi^0\gamma\gamma$.

Channel($J/\psi \to$)	Br	ε^{sel}_{MC}	N^{Norm}
$p\bar{p}\pi^0\pi^0$	$(1.60 \pm 0.26) \times 10^{-3}$	1.68×10^{-4}	61 ± 10
$\Sigma^+\Sigma^- \to p\pi^0\bar{p}\pi^0$	$(2.77 \pm 0.03) \times 10^{-4}$	1.26×10^{-4}	8 ± 0
$\Delta^+\Delta^- \to p\pi^0\bar{p}\pi^0$	$(2.30 \pm 0.07) \times 10^{-4}$	1.76×10^{-4}	9 ± 0
$p\pi^0\Delta^- + c.c \to p\pi^0\bar{p}\pi^0$	$(2.04 \pm 0.06) \times 10^{-4}$	1.76×10^{-4}	8 ± 0
$\gamma\Sigma^+\Sigma^- \to \gamma p\pi^0\bar{p}\pi^0$	$(3.31 \pm 0.12) \times 10^{-5}$	2.98×10^{-3}	23 ± 1
$\gamma\Delta^+\Delta^- \to \gamma p\pi^0\bar{p}\pi^0$	$(5.40 \pm 0.50) \times 10^{-5}$	2.86×10^{-3}	35 ± 3
$\gamma p\pi^0\Delta^- + c.c \to \gamma p\pi^0\bar{p}\pi^0$	$(14.40 \pm 2.80) \times 10^{-5}$	2.44×10^{-3}	78 ± 15
$p\bar{p}\omega \to p\bar{p}\gamma\pi^0$	$(9.11 \pm 1.27) \times 10^{-5}$	1.59×10^{-3}	33 ± 5
$\gamma p\bar{p}\omega \to \gamma p\bar{p}\gamma\pi^0$	$(1.28 \pm 0.07) \times 10^{-5}$	1.14×10^{-2}	33 ± 2
$J/\psi \to p\bar{p}\eta', \eta' \to \gamma\omega, \omega \to \gamma\pi^0$	$(4.78 \pm 0.99) \times 10^{-7}$	1.80×10^{-2}	2 ± 0
Total			290 ± 19

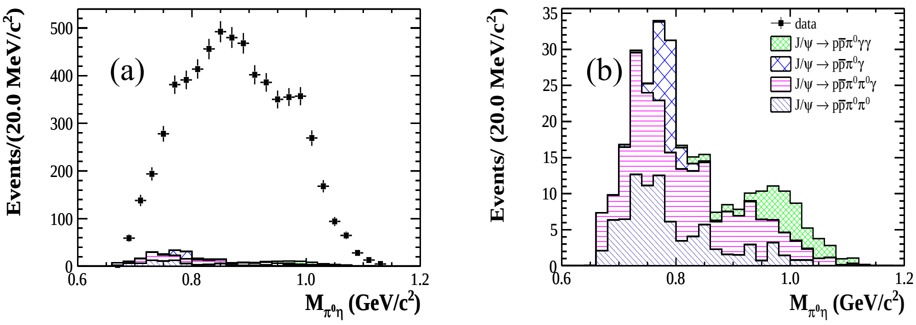

Figure 5.7 (a) The mass spectrum of $\pi^0\eta$ for data and exclusive backgrounds (a) and for exclusive backgrounds (b).

The studies of the mass spectra of $M_{p\pi^0}$ and $M_{p\eta}$ show that the processes with intermediate states of $N(1440)$, $N(1535)$ and $N(1650)$ are the dominant contributions to $J/\psi \to p\bar{p}\pi^0\eta$ where $N(1440)$ decays to $p\pi^0$, $N(1535)$ decays to $p\pi^0$ or $p\eta$, and $N(1650)$ decays to $p\eta$, with the charge-conjugate modes being implied.

A simple partial wave analysis (PWA) by calculating the amplitudes of these processes according to their Feynman Diagrams [15] is applied to the surviving events in data which can be find in Appendix. **??** for detail. The maximum likelihood method is used to fit the branching fraction of these intermediate states and their interferences. Figure 5.8(a) shows the scatter plot of $M^2_{p\pi^0}$ versus $M^2_{\bar{p}\eta}$ in data, which is consistent with the scatter plot of $M^2_{p\pi^0}$ versus $M^2_{\bar{p}\eta}$ of the best fit result shown in Fig. 5.8(b). The interference between the processes with N^* and the $p\bar{p}a_0(980)$ is found to be very small and is neglected in the following. The yield of $J/\psi \to p\bar{p}a_0(980) \to p\bar{p}\pi^0\eta$ obtained by the PWA is within 1σ statistical deviation of that obtained by fitting the mass spectrum of $\pi^0\eta$ described below. When applying the PWA without the component $J/\psi \to p\bar{p}a_0(980)$, no enhancement around 1.0 GeV is observed in the MC projection of $\pi^0\eta$ mass spectrum, which indicates that the enhancement seen in data is not from the processes with N^* intermediate states or their interferences.

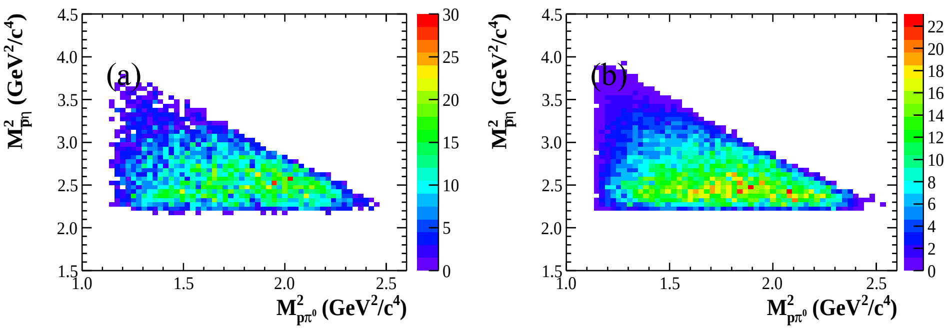

Figure 5.8 The scatter plot of $M^2_{p\pi^0}$ versus $M^2_{\bar{p}\eta}$ from data (a), from MC projection of all intermediate states superimposed (b).

5.1.3 Fitting on $M_{\pi^0\eta}$

An unbinned extended maximum likelihood fit is performed on the $\pi^0\eta$ mass spectrum. The probability density function (PDF) is

$$F(m) = f_{\text{sig}}\,\sigma(m) \otimes (\varepsilon(m) \times \hat{T}(m)) + (1 - f_{\text{sig}})\,B(m).$$

Here, f_{sig} is the fraction of $p\bar{p}a_0(980)$ signal events. The signal shape of $a_0(980)$ is described as an efficiency-weighted Flatté formula ($\varepsilon(m) \times \hat{T}(m)$) convoluted with a resolution function $\sigma(m)$. The resolution function $\sigma(m)$ is determined by fitting the reconstructed $a_0(980)$ signal with a double-gaussian of MC sample $J/\psi \to p\bar{p}a_0(980)$, $a_0(980) \to \pi^0\eta$ as shown in Fig. 5.9, where the input width of $a_0(980)$ is set to be 0.

The $\varepsilon(m)$ is the efficiency curve of $M_{\pi^0\eta}$ as shown in Fig. 5.10, which is studied using 500k PHSP MC sample of $J/\psi \to p\bar{p}\pi^0\eta$. The efficiency dependence on $M_{\pi^0\eta}$ is obtained by divide the number of generated events by that of the survived ones in each $M_{\pi^0\eta}$ bin. The efficiency changes slightly and smoothly. In the (0.95,1.05) GeV/c^2 region, the efficiency changes about 7%, hence the efficiency correction should be taken into consideration in fitting the $\pi^0\eta$ distribution.

The non-$a_0(980)$ background shape, expressed by $B(m)$, is described by a third-order Chebychev polynomial function. The Flatté formula [14] is used to parameterize the $a_0(980)$ amplitudes coupling to $\pi^0\eta$ and $K\bar{K}$ by a two-channel resonance expressed

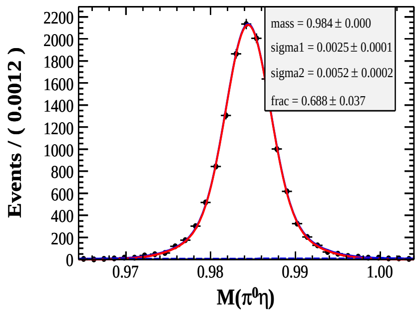

Figure 5.9 Invariant mass spectrum of $\pi^0\eta$ on signal MC with 0-width $a_0(980)$, fitted with Double-Gaussian function.

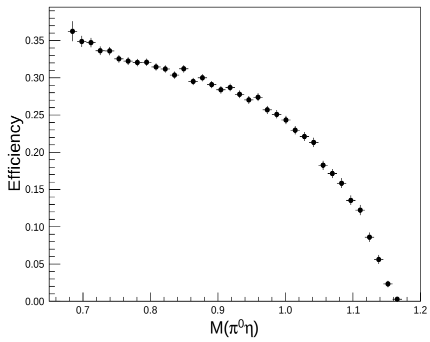

Figure 5.10 The selecting efficiency dependence on $M_{\pi^0\eta}$.

as

$$\hat{T}(m) \propto \frac{1}{(m_{a_0}^2 - m^2)^2 + (\rho_{\pi^0\eta} g_{a_0\eta\pi^0}^2 + \rho_{K\bar{K}} g_{a_0K\bar{K}}^2)^2},$$

where $\rho_{\pi^0\eta}$ and $\rho_{K\bar{K}}$ are the decay momenta of the π^0 or K in the $\pi^0\eta$ or $K\bar{K}$ rest frame, respectively.

The two coupling constants $g_{a_0\pi^0\eta}$ and $g_{a_0K\bar{K}}$ stand for $a_0(980)$ resonance coupling to $\pi^0\eta$ and $K\bar{K}$, respectively. Table 5.2 shows the previous experimental results of the a_0 coupling constants. The average values of the coupling constants are calculated with the weighted mean method, which is $\bar{x} = \Sigma_i \frac{x_i}{\sigma_i^2} / \Sigma_i \frac{1}{\sigma_i^2}$, $\sigma_{\bar{x}}^2 = 1/\Sigma_i \frac{1}{\sigma_i^2}$, to be $g_{a_0\pi^0\eta} = 2.83 \pm 0.05$ and $g_{a_0K\bar{K}} = 2.11 \pm 0.06$. In the fit, the two coupling constants $g_{a_0\pi^0\eta}$ and

Table 5.2 Previous experimental results of a_0 coupling constants and they gives consistent results.

Experiment	$g_{a_0\pi^0\eta}$	$g_{a_0K\bar{K}}$	$g_{a_0\pi^0\eta}/g_{a_0K\bar{K}}$
SND [16]	$3.11^{+2.61}_{-0.40}$	$4.20^{+14.01}_{-1.35}$	$0.75^{+0.52}_{-0.32}$
KLOE [17]	3.02 ± 0.25	2.24 ± 0.11	1.35 ± 0.09
BNL [18]	2.47 ± 0.76	1.67 ± 0.29	1.48 ± 0.08
CB [19]	3.33 ± 0.15	2.54 ± 0.23	1.31 ± 0.10
KLOE(new) [20]	$2.82 \pm 0.03 \pm 0.04$	$2.15 \pm 0.06 \pm 0.06$	$1.31 \pm 0.03 \pm 0.06$
CB(new) [21]	$2.87 \pm 0.06 \pm 0.09$	$2.09 \pm 0.06 \pm 0.09$	$1.38 \pm 0.05 \pm 0.04$

$g_{a_0K\bar{K}}$ are fixed to 2.83 and 2.11, respectively.

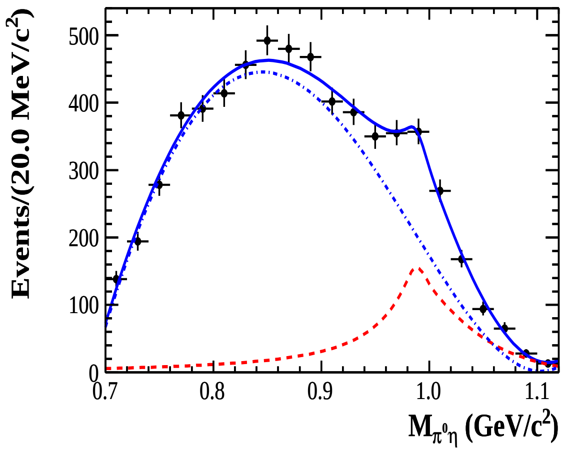

Figure 5.11 The results of fitting the mass spectrum for $\pi^0\eta$.

In the fit, the signal fraction f_{sig}, the $a_0(980)$ mass, and the parameters of the background polynomial are allowed to vary. The fit result of $M_{\pi^0\eta}$ is shown in Fig. 5.11. The yield of $a_0(980)$ events is 849 ± 144, with a statistical significance of 6.5σ which is calculated from the log-likelihood difference between fits with and without the $a_0(980)$ signal component. The fit mass is 1.012 ± 0.007 GeV/c^2, which is slightly higher than the PDG value [12]. The product branching fraction $Br(J/\psi \to p\bar{p}a_0(980) \to p\bar{p}\pi^0\eta)$ is calculated to be $(6.8 \pm 1.2) \times 10^{-5}$, where the uncertainty is statistical only.

5.1.4 Input/Output Check

The robustness of this result has been validated with a toy MC study. Different signal MC samples of $J/\psi \to p\bar{p}a_0(980), a_0(980) \to \pi^0\eta$ are generated with different mass and width of the $a_0(980)$. Background events are randomly sampled according to the background shapes. The fitted mass of $a_0(980)$ is compared with the input one in two cases, randomly sampling only signal events and randomly sampling both signal and background events. The fluctuation of the mass difference is plotted as a histogram and fitted by a gaussian function as shown in Fig. 5.12. In the first case, the mass deviation is -0.77 MeV/c^2 with a resolution of 1.97 MeV/c^2. In the second case, the mass deviation is -0.88 MeV/c^2 with a resolution of 3.19 MeV/c^2. In both cases, the fit value of the $a_0(980)$ mass is found to be consistent with the input value within statistical uncertainties.

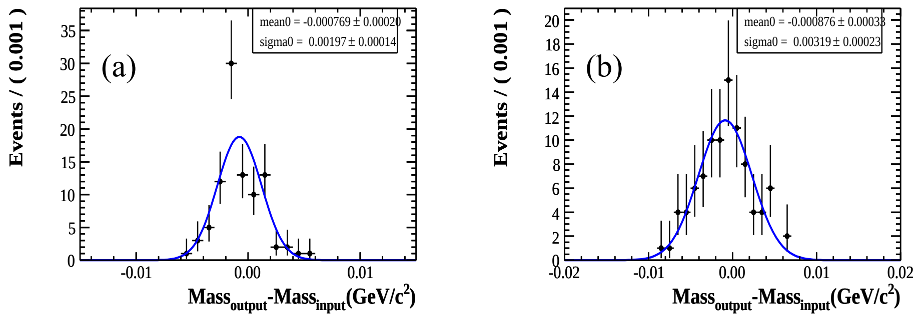

Figure 5.12 (a)The difference between fitted mass and input mass by varying the signal events only (a), by varying both signal and background events (b).

5.1.5 Feynman Diagram Calculation Analysis

5.1.5.1 Introduction of FDC

FDC is short for Feynman Diagram Calculation which is developed by Prof.Wang JianXiong. It can build the corresponding Feynman Diagram according to the physics model. And calculate the amplitude analytically. It is a useful tool for partial wave analysis especially for hadronic physics.

In our analysis of $J/\psi \to p\bar{p}\pi^0\eta$, we add 6 resonances. The information of these resonances are shown in Table 5.3. The resonance P11[1440] and S11[1535] can decay to $p\pi^0$ and $p\eta$. The P11[940] is treated as the off-shell nucleon which has a relatively large width. Since the FDC is not precisely for the 3-body decay, for the $J/\psi \to p\bar{p}a_0(980)$ process, we treat the $p\bar{p}$ decays from a wide resonance named X[1880]. This is a simplify of the real physics figure and the mass and angular distribution between $J/\psi \to X[1880]a_0(980)$ and $J/\psi \to p\bar{p}a_0(980)$ is consistent well.

Table 5.3 The vertex information of each particle involved in the decay process.

name	spin	parity	c	isospin	G	Strange	Baryon	Charge	Mass	Width
P11[940]	1/2	+1	X	1/2	X	0	1	1	1.10	0.5
P11[1440]	1/2	+1	X	1/2	X	0	1	1	1.440	0.3
S11[1535]	1/2	-1	X	1/2	X	0	1	1	1.535	0.15
X[1880]	1	-1	-1	1	1	0	0	0	1.88	0.5
a0[980]	0	+1	+1	1	-1	0	0	0	1.00	0.06
S11[1650]	1/2	-1	X	1/2	X	0	1	1	1.650	0.150

There are 11 Feynman diagram as shown in Fig. 5.13.

Diag. 1 is the process $J/\psi \to p\bar{p}a_0(980)$ where the $p\bar{p}$ is assumed to be decayed from a wide resonance, noted as mode 1.

Diag. 2 and 4 are the process $J/\psi \to N(1440)\bar{N}(1650) + c.c$, noted as mode 2.

Diag. 3 and 5 are the process $J/\psi \to N(1650)\bar{N}(940) + c.c$ where the N(940) is the off-shell resonance, noted as mode 3.

Diag. 6 and 9 are the process $J/\psi \to N(1535)\bar{N}(1535)$, noted as mode 4.

Diag. 7 and 10 are the process $J/\psi \to N(1535)\bar{N}(1440) + c.c$, noted as mode 5.

Diag. 8 and 11 are the process $J/\psi \to N(1535)\bar{N}(940) + c.c$, noted as mode 6.

5.1.5.2 Modification of the FDC

In FDC, when the vertices in the Table 5.13 are added, the corresponding PDF are evaluated in the $fff.f$ file. For the process shown diagram 1 in Fig. 5.13. The PDF

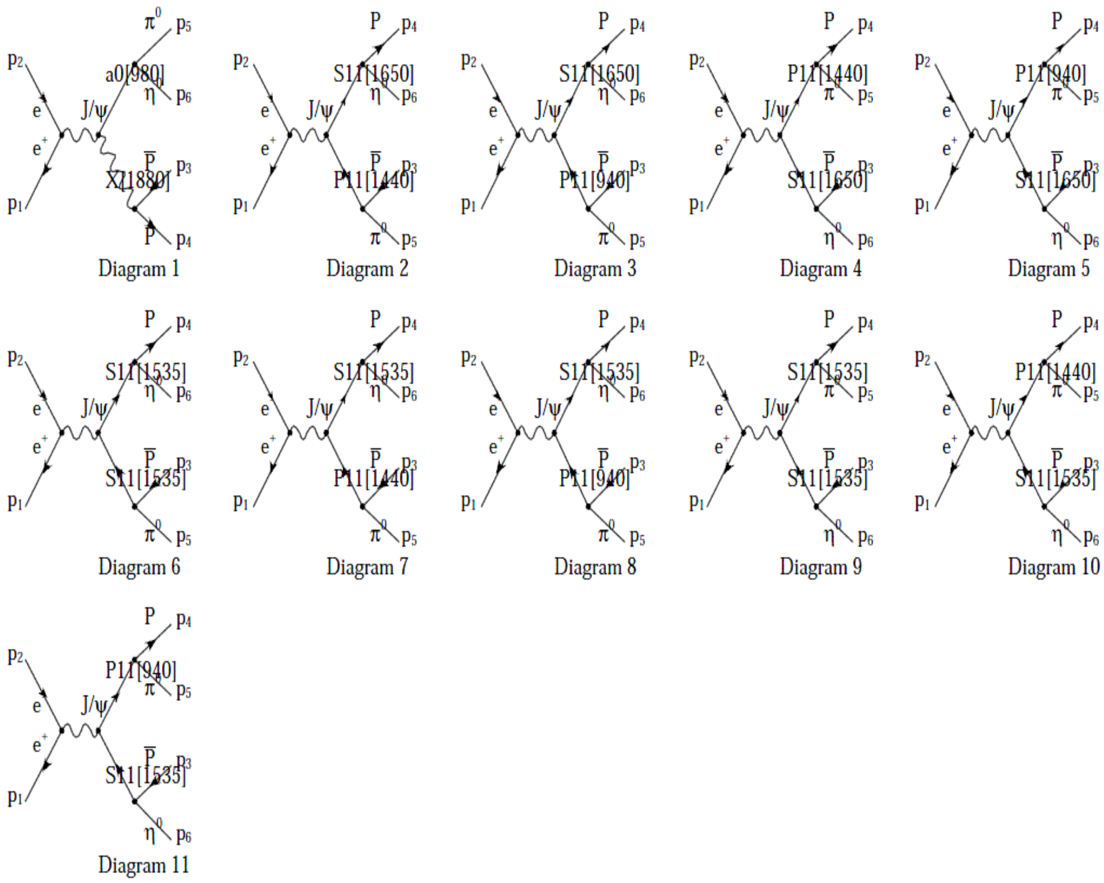

Figure 5.13 The Feynman Diagram of process $J/\psi \to p\bar{p}\pi^0\eta$.

given in $fff.f$ is shown as:

$$s(1) = c1 \times BW(m_{J/\psi}) \times BW(m_{X(1880)}) \times BW(m_{a0(980)}). \tag{5.1}$$

In our analysis, using the Breit-Wigner Formulation for the $X(1880) \to p\bar{p}$ is not appropriate since a Breit-Wigner Formulation gives a strong physics interpretation on X(1880) resonance. In this analysis, we just "borrow" the X(1880) to generator the Feynman diagram and the $p\bar{p}$ cannot be treated as from a resonance decay. So we should replace the $BW(m_{X(1880)})$ into a physics independent polynomial function. Fig. 3.4 shows the fitting result of the $M_{p\bar{p}}$ distribution, we used a exponential function to fit it.

The fitting function is :

$$P = e^{-0.5(\frac{m_{p\bar{p}}-2.02}{0.0696})^2}. \tag{5.2}$$

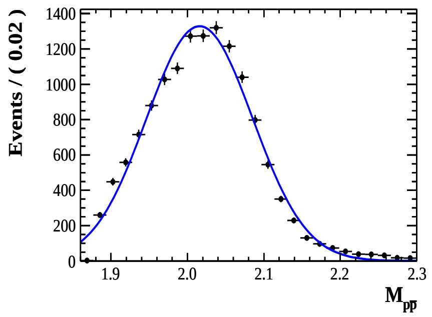

Figure 5.14 The fitting results of $M_{p\bar{p}}$ for signal MC with an exponential function.

On the other hand, the $BW(a_0(980))$ also need to be modified to $flatt\acute{e}$ formulism shown as:

$$T = \frac{1}{m^2_{\pi^0\eta} - m^2_{a0(980)} + i(\rho_1 g^2_{a_0\pi^0\eta} + \rho_2 g^2_{a_0K\bar{K}})}. \tag{5.3}$$

We add the $flatt\acute{e}$ formulism in the $abc.f$ file and then refer this function in $fff.f$ file. The coupling constants $g_{a_0\pi^0\eta}$ and $g^2_{a_0K\bar{K}}$ are fixed to be 2.83 and 2.11, respectively.

5.1.5.3 Analysis on $J/\psi \to p\bar{p}\pi^0\eta$

In the analysis, we use 6246 Data and 240000 MC event to do the fit. There MC are generated in Phase space. We do the iteration and find the minimum likelihood value. The spectrum used for the fitting is $\cos\theta_p$, $\cos\theta_{\pi^0}$, $M_{p\bar{p}}$, $M_{\pi^0\eta}$ and the scatter plot $M^2_{p\pi^0}$ versus $M^2_{\bar{p}\eta}$.

Fig. 5.15 shows the global fitting result. The data and the fitting result consistent with each other well. The scatter plot is shown in Fig. 5.8.

Here we define:

$$\chi^2 = \sum_{i=1}^{N} \frac{(n_i - \nu_i)^2}{\nu_i}, \tag{5.4}$$

where n_i and ν_i are the number of events in the data and fitting result for each bin. We got the $\chi^2/nbin$ for each distribution is:

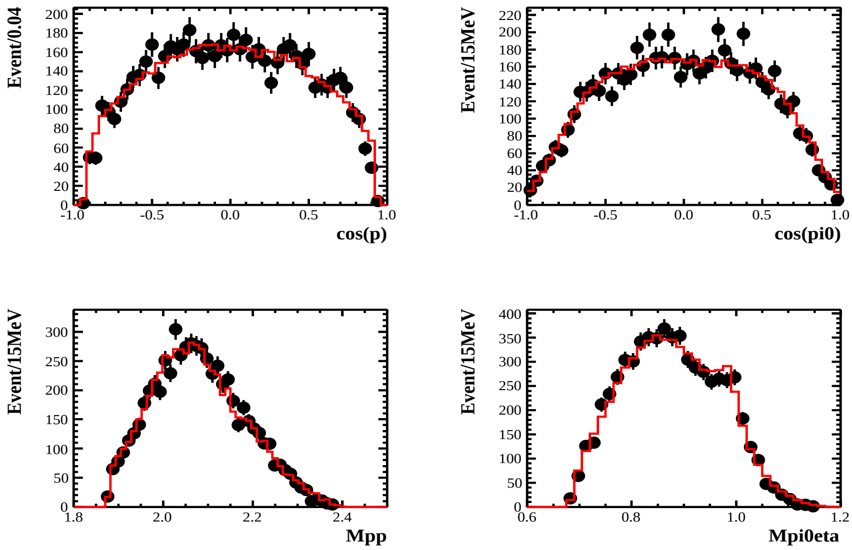

Figure 5.15 The global fitting results for several distributions. The dots represent data and the red histogram represents the fitting result.

	$\cos_{\pi^0}$	$\cos_p$	$M_{p\bar{p}}$	$M_{\pi^0\eta}$
$\chi^2/nbins$	1.514	1.343	0.904	1.275

In the FDC analysis, we didn't scan the mass and width of these resonance. We take the resonance parameters in PDG which were measured by $J/\psi \to p\bar{p}\eta$ and $J/\psi \to p\bar{p}\pi^0$ analysis. The likelihood with $J/\psi \to p\bar{p}a_0(980)$ process is -1505.13 while the likelihood value without this process is -1102.69.

Table 5.4 shows the branching ratio of each intermediate states and there interference. The value in the diagonal is the branching fraction of each component and the value in other place is the branching fraction of the interference. The branching ratio of $J/\psi \to p\bar{p}a_0(980)$ is 0.115 which is corresponding to 718 events. The nominal fit without considering the interference is 849 ± 144. They are consistent within statistical error.

Table 5.4 Summary of the branching fraction in the best fit and there interference.

Component	mode 1	mode 2	mode 3	mode 4	mode 5	mode 6
mode 1	0.115					
mode 2	0.0443	2.320				
mode 3	-0.00451	-2.703	1.106			
mode 4	0.00171	0.916	-0.0006	0.896		
mode 5	-0.00101	-3.085	1.636	-0.890	1.437	
mode 6	-0.0002	1.851	-1.609	-0.389	-1.504	0.875

5.2 Systematic Uncertainty

The systematic uncertainties of $Br(J/\psi \to p\bar{p}a_0(980) \to p\bar{p}\pi^0\eta)$ are mainly from uncertainties due to imperfect modelling of the data by the simulation, such as tracking and PID efficiency, photon detection efficiency, the kinematic fit and the $\pi^0\pi^0$ veto metric, and uncertainties from fitting method, total number of J/ψ.

- The systematic uncertainty associated with the tracking efficiency as a function of transverse momentum and the uncertainty due to the PID efficiency of proton/antiproton have been studied by a control sample of $J/\psi \to p\bar{p}\pi^+\pi^-$ decays using a technique similar to that discussed in Ref. [22]. In the analysis of $J/\psi \to p\bar{p}a_0(980)$, due to the low transverse momentum of proton and antiproton, the uncertainty of tracking efficiency is determined by the weighted uncertainty $\Sigma_i\varepsilon_i r_i$, where ε_i represents the data/MC difference in each transverse momentum bin [22] and r_i represents the proportion of each transverse momentum bin in data. The systematic uncertainty due to the tracking efficiency is estimated to be 4.0% per proton and 5.0% per antiproton, respectively. The large uncertainty of tracking efficiency is because of limited statistics in control sample and improper simulation of interactions with material for low momentum proton and antiproton. The uncertainty due to PID efficiency is 2.0% per proton or antiproton.

- The systematic uncertainty due to photon detection is 1.0% per photon. This is determined from studies of the photon detection efficiency in the control sample

$J/\psi \to \rho^0\pi^0$ [22].

- To estimate the uncertainty from the kinematic fit, the efficiency of the selection on the χ^2_{4C} of the kinematic fit is studied using events of the decay $J/\psi \to p\bar{p}\eta$, $\eta \to \pi^0\pi^0\pi^0$:
  - Event selection
    * For photon and good charged tracks, the selection criteria are the same as that for $J/\psi \to p\bar{p}a_0$.
    * Selected events are required to have 2 good charged tracks and at least six good photons. The two charged tracks are identified as proton and anti-proton.
    * The π^0 candidates are reconstructed from the decay mode $\pi^0 \to \gamma\gamma$ by requiring the $\gamma\gamma$ invariant mass to be 0.075 GeV/c^2 $<$ $M_{\gamma\gamma}$ <0.175 GeV/c^2. Then a 1C kinematic fit to the $\gamma\gamma$ pair constrained to the π^0 mass is performed and the χ^2 value of the fit is requested to be less than 25. At least 3 good π^0 candidates are required in one event.
    * To veto the background from $J/\psi \to p\bar{p}\eta, \eta \to \gamma\gamma$, the invariant mass of any $\gamma\gamma$ combination should be less than 0.5 GeV/c^2.
    * After the pre-selection, the purity of $J/\psi \to p\bar{p}\eta$ in inclusive MC is 79.76%. And the background in recoil mass spectrum of $p\bar{p}$ can be described with a polynomial function.
  - The efficiency of kinematic fit
    The efficiency of kinematic fit is defined as $\frac{N_{with\chi^2_{4C}\leq X}}{N_{without4Cfit}}$. The $N_{with\chi^2_{4C}\leq X}$ is obtained by fitting the recoil mass spectrum of $p\bar{p}$ after applying 4C kinematic fit and require χ^2_{4C} less than X. The $N_{without4Cfit}$ is obtained by fitting the recoil mass spectrum of $p\bar{p}$ without 4C kinematic fit. The comparison of the efficiency of kinematic fit between data and MC is shown in Fig. 5.16 (a) and the difference is shown in Fig. 5.16 (b). The uncertainty of kinematic fit and $\chi^2 < 35$ is determined to be 3.2%.

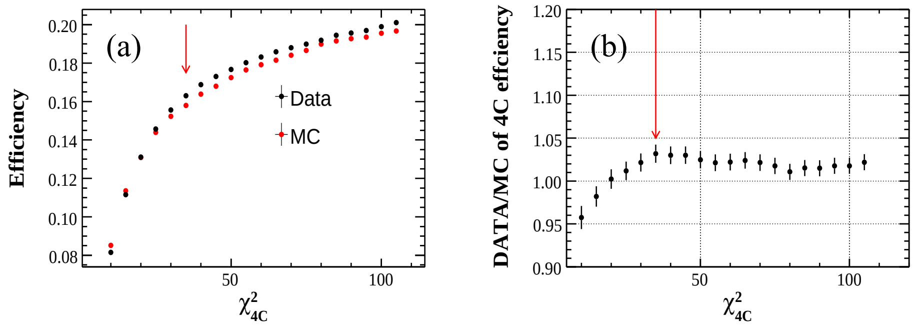

Figure 5.16 (a) Kinematic fit efficiency between data and MC from control sample. (b) The difference of the efficiency between data and MC.

- The systematic uncertainty arising from the $\pi^0\pi^0$ veto metric ($\chi^2_{\pi^0\pi^0} > 100$) is studied by a control sample $J/\psi \to \omega\eta \to \pi^+\pi^-\pi^0\eta$. The control sample is selected due to its similar final states to signal, high statistics, and narrow ω/η signals to extract the efficiency precisely. The purity of control sample is about 98.8% by a study on the inclusive MC sample.

  The $\chi^2_{\pi^0\pi^0}$ distributions of MC sample for the control sample and the interested process $J/\psi \to p\bar{p}a_0(980) \to p\bar{p}\pi^0\eta$ are shown in Fig. 5.17(a) (b), respectively. And the distributions are found to be very different. To better model the signal process $J/\psi \to p\bar{p}a_0(980) \to p\bar{p}\pi^0\eta$, the $\chi^2_{\pi^0\pi^0}$ distribution of control sample is weighted to that of signal process, where the weight are identical for the data and MC sample, and is the ratio of $\chi^2_{\pi^0\pi^0}$ distribution of the interested process to that of control sample (from MC sample), as shown in Fig. 5.18 (a). The event number of control sample is extracted by fitting invariant mass of $\pi^+\pi^-\pi^0$ with a double Gaussian function, and the efficiency for $\chi^2_{\pi^0\pi^0}$ requirement is ratio of the number of events that with and without veto metric, to be $(97.4 \pm 1.0)\%$ and $(97.6 \pm 0.4)\%$ for data and MC, respectively, where the errors are statistical only. Conservatively, the systematic uncertainty of $\chi^2_{\pi^0\pi^0}$ veto metric is estimated to be 1.3%.

- The systematic uncertainty due to the signal shape is determined by varying the

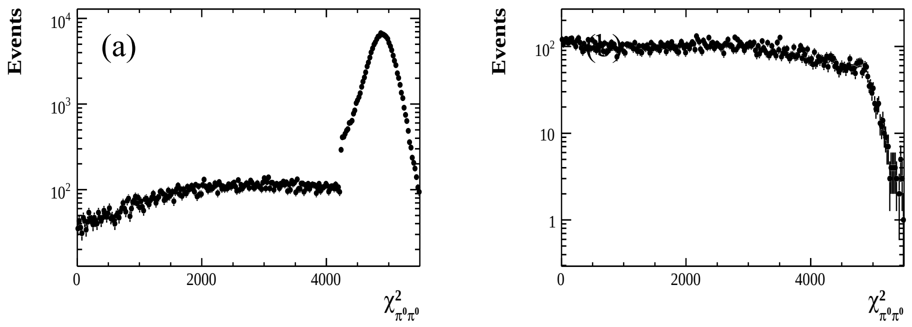

Figure 5.17 The distribution of $\chi^2_{\pi^0\pi^0}$, (a) MC of process $J/\psi \to \omega\eta \to \pi^+\pi^-\eta\pi^0$ and (b) MC of process $J/\psi \to p\bar{p}a_0(980) \to p\bar{p}\eta\pi^0$.

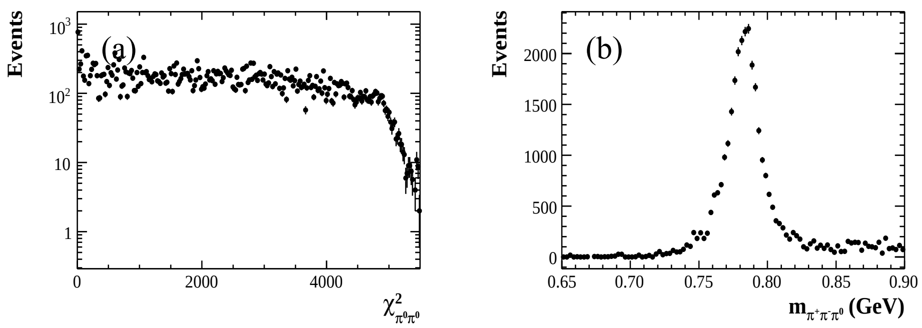

Figure 5.18 The distribution in data of process $J/\psi \to \omega\eta \to \pi^+\pi^-\eta\pi^0$ after weighting, (a) $\chi^2_{\pi^0\pi^0}$ and (b) $m_{\pi^+\pi^-\pi^0}$.

coupling constants by 1σ within their center values for $g_{a_0\pi^0\eta}$ and $g_{a_0K\bar{K}}$ separately. The largest difference is taken as the uncertainty.

- To study the uncertainty from background, alternative background shapes are obtained by varying the fitting range from [0.7, 1.12] GeV/c^2 to [0.73, 1.12] GeV/c^2 and changing order of Chebychev polynomial from third-order to fourth-order, which introduce uncertainties of 9.2% and 12.6%, respectively.

- The systematic uncertainty of the total number of J/ψ events is obtained by studying inclusive hadronic J/ψ decays [9] to be 1.2%.

The systematic uncertainties on the measurement of $Br(J/\psi \to p\bar{p}a_0(980) \to p\bar{p}\pi^0\eta)$ are summarized in Table 5.5. We treat all the sources of systematic uncertainties as uncorrelated and sum them in quadrature to obtain the total systematic uncertainty.

Table 5.5 Summary of systematic uncertainties on $Br(J/\psi \to p\bar{p}a_0(980) \to p\bar{p}\pi^0\eta)$.

Source	Uncertainty
Tracking	9.0%
Particle identification	4.0%
Photon detection	4.0%
4C kinematic fitting	3.2%
$\chi^2_{\pi^0\pi^0}$ cut	1.3%
Coupling constants	3.8%
Fit range	9.2%
Background shape	12.6%
Number of J/ψ events	1.2%
Total	19.6%

5.3 Conclusion and Discussion

Based on 2.25×10^8 J/ψ events collected with the BESIII detector at BEPCII, we observe $J/\psi \to p\bar{p}a_0(980)$, $a_0(980) \to \pi^0\eta$ for the first time with a statistical significance of 6.5σ. Taking the systematic uncertainty into account, the significance is 3.2σ. Without considering the interference between the signal channel and the same final states with intermediate N^* states, the branching fraction is measured to be

$$Br(J/\psi \to p\bar{p}a_0(980) \to p\bar{p}\pi^0\eta) = (6.8 \pm 1.2 \pm 1.3) \times 10^{-5},$$

where the first uncertainty is statistical and the second is systematic.

Our measurement provides a quantitative comparison with the chiral unitary approach [4]. This approximation uses several coefficients in the parametrization of meson-meson amplitudes. One of them, namely r_4 in [4], is constrained by fitting the $\pi^+\pi^-$ invariant mass distribution in the decay $J/\psi \to p\bar{p}\pi^+\pi^-$; the fit suggests two equally possible values, $r_4 = 0.2$ and $r_4 = -0.27$. The theory also predicts that the branching fractions of $J/\psi \to p\bar{p}a_0(980)$ and $J/\psi \to p\bar{p}\pi^+\pi^-$ are comparable for $r_4 = -0.27$, while the branching fraction of the former is one or two orders of magnitude lower than that of the latter for $r_4 = 0.2$. Taking the branching fraction of $J/\psi \to p\bar{p}\pi^+\pi^-$ from

PDG [12], the ratio of $Br(J/\psi \to p\bar{p}a_0(980) \to p\bar{p}\pi^0\eta)$ to $Br(J/\psi \to p\bar{p}\pi^+\pi^-)$ is found to be about 10^{-2}, which shows preference to $r_4 = 0.2$.

Bibliography

[1] S. Weinberg, Phenomenological Lagrangians. Physica A **96**, 327 (1979).

[2] V. Bernard, N. Kaiser and U.-G. Meissner, Chiral dynamics in nucleons and nuclei. Int. J. Mod. Phys. E **4**, 193 (1995).

[3] A. Pich, Chiral perturbation theory. Rept. Prog. Phys. **58**, 563 (1995).

[4] C. B. Li, E. Oset, and M. J. Vicente Vacas, Light scalar mesons in $J/\psi \to$ N anti-N meson meson decays in a chiral unitary approach. Phys. ReV. C **69**, 015201 (2004).

[5] N. N. Achasov and V. N. Ivanchenko, On a Search for Four Quark States in Radiative Decays of phi Meson. Nucl. Phys. B **315**, 465 (1989).

[6] J. Weinstein and N. Isgur, The $qq\bar{q}\bar{q}$ System in a Potential Model. Phys. Rev. D **27**, 588 (1983).

[7] J. Weinstein and N. Isgur, $K\bar{K}$ Molecules. Phys. Rev. D **41**, 2236 (1990).

[8] S. Ishida $et\ al.$, Possibility of $a_0(980)$ and $f_0(980)$ as hybrid mesons with a massive constituent gluon. the 6th International conference on Hadron Spectroscopy, 1995.

[9] M. Ablikim *et al.* (BESIII Collaboration), Determination of the number of J/ψ events with $J/\psi \to inclusive$ decays. Chin. Phys. C **36**, 915 (2012).

[10] S. Jadach, B. F. L. Ward and Z. Was, Coherent exclusive exponentiation for precision Monte Carlo calculations. Phys. Rev. D **63**, 113009 (2001).

[11] R. G. Ping, Event generaters at BESIII. Chin. Phys. C **32**, 599 (2008);
D. J. Lange, The EvtGen particle decay simulation package. Nucl. Instr. Meth. A **462**, 152 (2001).

[12] J. Beringer $et\ al.$ (Particle Data Group), Review of Particle Physics (RPP). Phys. Rev. D **86**, 010001 (2012).

[13] J. C. Chen $et\ al.$, Event generator for J/ψ and $\psi(2S)$ decay. Phys. Rev. D **62**, 034003 (2000).

[14] S. M. Flatté, Coupled-Channel Analysis of the $\pi\eta$ and $K\bar{K}$ Systems Near $K\bar{K}$ Threshold. Phys. Lett. B **63**, 224 (1976).

[15] J. X. Wang, Progree in FDC project. Nucl. Instrum. Meth. A **534**, 241 (2004).

[16] M. N. Achasov, $et\ al.$, The $\phi(1020) \to \pi^0\pi^0\gamma$ decay. Phys. Lett. B **485**, 349 (2000).

[17] A. Aloisio, $et\ al.$, (KLOE Collaboration) Study of the decay $\phi \to \pi^0\pi^0\gamma$ with the KLOE detector. Phys. Lett. B **537**, 21 (2002).

[18] S. Teige, $et\ al.$, (E852 Collaboration), Properties of the $a_0(980)$ meson. Phys. Rev. D **59**, 012001 (1999).

[19] D. V. Bugg, V . V. Anisovich, A. V. Sarantsev and B. S. Zou, Coupled channel analysis of data on $\bar{p}p \to 3\pi^0$, $\eta\eta\pi^0$, and $\eta\pi^0\pi^0$ at rest, with the N/D method. Phys. Rev. D **50**, 4412 (1994).

[20] F. Ambrosina, $et\ al.$, (KLOE Collaboration), Study of the $a_0(980)$ meson via the radiative decay $\pi \to \eta\pi^0\gamma$ with the KLOE detector. Phys. Lett. B **681**, 5 (2009).

[21] D. V. Bugg, Re-analysis of data on $a_0(1450)$ and $a_0(980)$. Phys. Rev. D **78**, 074023 (2008).

[22] M. Ablikim $et\ al.$ (BESIII Collaboration), Study of χ_{cJ} radiative decays into a vector meson. Phys. Rev. D **83**, 112005 (2011).

Chapter 6

Summary and Prospect

In this thesis, I present my analysis work on BESIII, which can be categorized into two parts: measurement of the baryon pair production cross section and effective FF, and the first observation of process $J/\psi \to p\bar{p}a_0(980)$.

The baryon pair production cross section and effective FF are measured for $p\bar{p}$ (in Chap. 3), and $\Lambda\overline{\Lambda}$ (in Chap. 4). Besides, in Appendix, we present the preliminary study on $e^+e^- \to \Lambda_c^+\bar{\Lambda}_c^-$ (in Append. A) and $e^+e^- \to n\bar{n}$ (in Append. B). The cross sections of $e^+e^- \to p\bar{p}$ and effective FFs are measured at 14 c.m. energies from 2232.4 to 3671.0 MeV. The effective FFs, which quantitatively describe how much the experimental cross section differs from a point-like one, are extracted under the assumption that electromagnetic FFs are equal ($|G_E| = |G_M|$). The results are well consistent with the BaBar results which were the best precision measurement. The precision of Born cross sections with $\sqrt{s} \leq 3.08$ GeV are between 6.0% and 18.9% which are much improved comparing with BaBar results (9.4% and 26.9%). The precisions are comparable with previous results at $\sqrt{s} > 3.08$ GeV. Moreover, the ratio of electric to magnetic FFs, $|G_E/G_M|$, are extracted by fitting the distribution of the polar angle of the proton at $\sqrt{s} = 2232.4$, 2400.0 MeV and a combined data sample with $\sqrt{s} = 3050.0$, 3060.0 and 3080.0 MeV. The results are close to unity and consistent with BaBar results at the same q^2 region.

The precision of $|G_E/G_M|$ of proton is limited by statistical, between 25% and 50%. From a toy MC study, we can predict the expected luminosity for different $|G_E/G_M|$ precision requirement at $\sqrt{s}$=2232.4 MeV, as shown in Table 6.1, where N_{sig} is the number of MC events to extract the Born cross section or $|G_E/G_M|$ ratio, $\delta_{R_{em}}$ and δ_σ are the statistical uncertainties of $|G_E/G_M|$ ratio and cross section, respectively. N_{orig} is the number of MC event after detection efficiency correction. The expected luminosity can be calculated by N_{orig}/σ_{Born}.

Table 6.1 Prediction of the expected luminosity for a required precision of $|G_E/G_M|$ form MC study.

N_{sig}	$\delta_{R_{em}}/R_{em}$ (%)	δ_σ/σ (%)	N_{orig}	Expect Lumi. (pb^{-1})
769 ± 28	18	3.6	1165	3.295
1535 ± 39	15	2.5	2324	6.573
2326 ± 48	12	2.1	3524	9.967
3110 ± 56	11	1.8	4712	13.326
3881 ± 62	9.4	1.6	5880	16.630
7856 ± 89	6.7	1.1	11903	33.662
15652 ± 125	4.6	0.8	23715	67.068
23572 ± 154	3.7	0.65	35715	101.004
31286 ± 177	3.2	0.57	47403	134.058
39085 ± 198	2.9	0.51	59219	167.466
78116 ± 279	2.0	0.36	118358	334.722
156253 ± 395	1.4	0.25	236747	669.533

Besides the proton FF measurement, we also present the study of $e^+e^- \to \Lambda\overline{\Lambda}$. The highlight of this work is a non-zero cross section near $\Lambda\overline{\Lambda}$ production threshold at $\sqrt{s} = 2232.4$ MeV is observed. The combined cross section is obtained, by reconstructing charged decay channel of $\Lambda/\overline{\Lambda}$ and reconstructing neutral decay channel of $\overline{\Lambda}$ respectively, to be 320 ± 58 pb, where the error here is the combine error of statistical and systematic. This result is surprising, since the cross section of neutral baryon pair production at threshold is expected to be 0 from theoretical prediction. When taking into account the energy spread, the measured cross section here is still much larger than the prediction. The result indicates there are something beyond phase space factor is at play near threshold. We also measured the Born cross section of $e^+e^- \to \Lambda\overline{\Lambda}$ at 2400.0, 2800.0 and 3080.0 MeV, as well as the effective FF of Λ. The precision of the Born cross section is between 20.9% and 33.3% while the precision from BaBar experiment in this energy region is between 32.2% and 100.0%. The uncertainty is dominant by statistics. The dominant systematic source is the angular distribution of Λ. With a large statistical, the angular distribution of Λ can be parameterised and the uncertainty source of this term will be significantly improved.

At BEPCII, a new scan with c.m. energy ranging between 2.0 GeV and 3.1 GeV is ongoing with higher integrated luminosity. The measurement on proton FF ratio and hyperon FFs with improved precision is foreseen with the new scan data. Table 6.2 shows the energy points of data taken, proposed integral luminosity and the online integral luminosity. Besides, we also present the preliminary result of $|G_E/G_M|$ ratio with statistical uncertainty only, which is based on the preliminary selection efficiency of process $e^+e^- \to p\bar{p}$, $\varepsilon'_{p\bar{p}}$, with the ISR correction applied, as well as the reconstructed $p\bar{p}$ events in data, $N_{p\bar{p}}$. The precision of $|G_E/G_M|$ ratio is expected to be less than 10.0% at low c.m.enegies, which will not only improve the accuracy of $|G_E/G_M|$ ratio, but also help reveal the inconsistence between results from BaBar and PS170 experiments. With the new scan data, we also present the preliminary results of cross sections. The line-shape near 2.25 and 3.0 GeV will be measured with high precision, and the results will reveal the two rapid decreases in these two regions are from physical structures or statistical fluctuations.

Table 6.2 Data taking plan in 2.0 - 3.1 GeV at BEPCII.

E_{cm} (MeV)	L_{Needed} (pb^{-1})	L_{online} (pb^{-1})	$\varepsilon'_{p\bar{p}}$ (%)	$N_{p\bar{p}}$	R_{em} (%)	σ (pb)
2200.0	13	13.0	53.1	2582	1.46 ± 0.13	372.4 ± 7.4
2386.4	20	22.1	58.5	1474	0.73 ± 0.16	113.6 ± 3.0
2396.0	$\geq$64	64.8	58.5	4295	0.97 ± 0.09	113.0 ± 1.7
2500.0	0.4895	1.04	59.4	45	-	72.8 ± 10.9
2644.4	65	32.5	59.9	521	1.22 ± 0.19	37.0 ± 1.4
2646.4	-	33.7	59.9	717		25.9 ± 1.1
2700.0	0.5542	0.987	59.7	21	-	35.5 ± 7.8
2800.0	0.6136	0.965	60.0	14	-	24.3 ± 6.5
2900.0	100	102	59.7	894	0.84 ± 0.26	15.4 ± 0.5
2950.0	15	15.7	59.3	99	-	11.3 ± 1.1
2981.0	15	15.4	59.4	104	-	12.0 ± 1.2
3000.0	15	15.3	59.7	79	-	9.2 ± 1.0
3020.0	15	16.6	59.5	84	-	8.9 ± 1.0
3080.0	120	123	59.0	578	0.64 ± 0.41	8.4 ± 0.4

Apart from proton FFs, the hyperon process produced from electron positron annihilation, such as $\Lambda\overline{\Lambda}$, $\Sigma^0\overline{\Lambda}$, $\Sigma\overline{\Sigma}$, $\Xi\overline{\Xi}$ and so on, as well as hyperon FFs, can also be studied with improved precision with the new scan data. For the $\Lambda\overline{\Lambda}$ process, by analyzing the helicity angle of proton from $\Lambda \to p\pi^+$ process, the polarization of Λ can be measured, in such way, we can measure the phases difference of G_E and G_M of Λ. From Table 6.2, the integral luminosity is 11.2 pb^{-1} at $\sqrt{s}$ =2232.4 GeV, which is over four times of the previous data set. Therefore, the precision of cross section of $e^+e^- \to \Lambda\overline{\Lambda}$ near threshold will be significantly improved. The data samples collected at $\sqrt{s}$ =2309.4, 2386.4, 2396.0, 2644.4 MeV are just 1.0 - 2.0 MeV above the production threshold of $\Sigma^0\overline{\Lambda}$, $\Sigma^0\bar{\Sigma}^0$, $\Sigma^-\bar{\Sigma}^+$, $\Xi^-\bar{\Xi}^+$, respectively. The measurement of baryon pair production near threshold can provide a series of experimental results, which can help resolve the strange structure on $p\bar{p}$ and $\Lambda\overline{\Lambda}$ threshold behaviors.

With 225 M J/ψ data collected at BESIII, we studied the process $J/\psi \to p\bar{p}a_0(980)$. The first observation of $a_0(980)$ production near threshold coupling with proton antiproton pair provides information of the low-lying scalar meson, $a_0(980)$. Besides, we find rich dynamics in this process, such as the $N(1440)$, $N(1535)$ and $N(1650)$ resonances lying in the mass spectra of $M_{p\pi^0}$ and $M_{p\eta}$. The branching fraction of $J/\psi \to p\bar{p}a_0(980) \to p\bar{p}\pi^0\eta$ is measured without considering the interference between the signal channel and these same final state with intermediate N^* states, to be $(6.8\pm1.2\pm1.3)\times10^{-5}$. The yield of signal by a simple PWA which considers the interference between these final states gives a consist result within 1σ statistical deviation. The four-body decay of J/ψ into two baryon pair and two mesons is investigated in the ChPT, and the experimental measurement of process $J/\psi \to p\bar{p}\pi^0\eta$ is is needed to restrict several free coefficients in meson-meson amplitude calculation. The measurement of $J/\psi \to p\bar{p}a_0(980)$ at BESIII can fill the experimental blank to a certain degree and settle the free parameter by comparing the branching fraction with $J/\psi \to p\bar{p}\pi^+\pi^-$.

Appendix A

Preliminary Study of $e^+e^- \to \Lambda_c^+\overline{\Lambda}_c^-$ Near Production Threshold

In this chapter, the process $e^+e^- \to \Lambda_c^+\overline{\Lambda}_c^-$ is studied by using data taking with the BESIII detector. The information of the data sets is listed in Table A.1. The process of $e^+e^- \to \Lambda_c^+\overline{\Lambda}_c^-$ is produced with KKMC. For the subsequent decay, $\Lambda_c^+ \to pK^-\pi^+$ is generated based on preliminary PWA results, while the other decay modes of Λ_c^+ are generated by sampling the phase space according to the mass spectrum. The decay modes used for tagging Λ_c^+ are listed in Table A.2. By default, tagging $\overline{\Lambda}_c^-$ is also applied.

Table A.1 The c.m.s energy and luminosity of the data sets.

$\sqrt{s}$ (GeV)	Luminosity (pb^{-1})
4.575	47.74
4.58	8.516
4.59	8.110
4.60	567.6

Table A.2 The tagged decay modes of Λ_c^+ in this analysis.

Decay modes	BR(modeN)/BR(mode1)	BR
1. $\Lambda_c^+ \to pK^-\pi^+$	1	(6.84 ± 0.24)% [1]
2. $\Lambda_c^+ \to pK_s^0, K_s^0 \to \pi^+\pi^-$	$(0.47 \pm 0.04) \cdot 50.0\% \cdot 69.2\%$	(1.11 ± 0.11)%
3. $\Lambda_c^+ \to \Lambda\pi^+, \Lambda \to p\pi^-$	$(0.20 \pm 0.02) \cdot 63.9\%$	(0.87 ± 0.10)%
4. $\Lambda_c^+ \to pK^-\pi^+\pi^0, \pi^0 \to \gamma\gamma$	$(0.67 \pm 0.12) \cdot 98.8\%$	(4.53 ± 0.84)%
5. $\Lambda_c^+ \to pK_s^0\pi^0, K_s^0 \to \pi^+\pi^-, \pi^0 \to \gamma\gamma$	$(0.66 \pm 0.09) \cdot 50.0\% \cdot 69.2\% \cdot 98.8\%$	(1.54 ± 0.23)%
6. $\Lambda_c^+ \to \Lambda\pi^+\pi^0, \Lambda \to p\pi^-, \pi^0 \to \gamma\gamma$	$(0.73 \pm 0.18) \cdot 63.9\% \cdot 98.8\%$	(3.15 ± 0.79)%
7. $\Lambda_c^+ \to pK_s^0\pi^+\pi^-, K_s^0 \to \pi^+\pi^-$	$(0.51 \pm 0.06) \cdot 50.0\% \cdot 69.2\%$	(1.21 ± 0.16)%
8. $\Lambda_c^+ \to \Lambda\pi^+\pi^+\pi^-, \Lambda \to p\pi^-$	$(0.52 \pm 0.03) \cdot 63.9\%$	(2.27 ± 0.18)%
9. $\Lambda_c^+ \to \Sigma^0\pi^+, \Sigma^0 \to \Lambda\gamma, \Lambda \to p\pi^-$	$(0.20 \pm 0.04) \cdot 63.9\%$	(0.87 ± 0.18)%
10.$\Lambda_c^+ \to \Sigma^+\pi^+\pi^-, \Sigma^+ \to p\pi^0, \pi^0 \to \gamma\gamma$	$(0.69 \pm 0.08) \cdot 51.6\% \cdot 98.8\%$	(2.41 ± 0.31)%

A.1 Analysis Strategy

A.1.1 Event Selection

Each charged track is required to be within the polar angle coverage of the MDC, which means that $|\cos\theta|$ <0.93, and passes within 1 cm of the e^+e^- interaction point in the transverse direction to the beam line and within 10 cm of the interaction point along the beam axis. Information from dE/dx and TOF are combined to calculate the particle identification (PID) probability under the hypothesis that the track is a pion, kaon or proton. Each charged track is assigned a particle type with the highest probability.

Photon candidates are required to have a minimum energy deposition of 25 MeV in the barrel ($|\cos\theta|$ <0.8) of the EMC and 50 MeV in the end caps (0.86< $|\cos\theta|$ <0.92) of the EMC. EMC timing requirements ($0 \leq T \leq 14$ in unit of 50 ns) are used to suppress electronic noise and to remove shower unrelated to physics.

The π^0 candidates are selected from pairs of photons, and the mass window is applied as $0.095\,\mathrm{GeV}/c^2 < m_{\gamma\gamma} < 0.195\,\mathrm{GeV}/c^2$ to constraint the invariant mass of each photon pair to the nominal π^0 mass, and a require $\chi^2_{1C} < 50$ is also used to decrease background. In order to remove background events further, a cut on the energy asymmetry $|E_{\gamma 1} - E_{\gamma 2}|/p_{\pi^0}$ is required to be less than 0.95.

The K_S^0 and Λ candidates are reconstructed via the processes $K_s^0 \to \pi^+\pi^-$ and $\Lambda \to p\pi^-$, performing a vertex-constrained fit to all oppositely charged track pairs, without particle identification requirements. A second vertex fit is also performed for the K_S^0 and Λ. The flight length, L, obtained from this fit must satisfy $L/\sigma_L > 2$, where σ_L is the estimated error of L.

The two variables beam-constrained mass M_{bc} and energy difference δ_E are used to identify the signals, which are defined as follows:

$$M_{bc} = \sqrt{E_{\text{beam}}^2/c^4 - |\overrightarrow{p}_{\Lambda_c^+}|^2/c^2}$$

$$\delta_E = E_{\Lambda_c^+} - E_{\text{beam}}$$

where $\overrightarrow{p}$ and $E_{\Box_c^+}$ are the total momentum and energy of the Λ_c^+ candidate, and E_{beam} is the beam energy. The δ_E is fitted with a Gaussian or double-Gaussian function in data. Range of δ_E requirements at each c.m.s. energy are set at $(-3\sigma, 3\sigma)$.

After applying δ_E requirement, the intermediate states in Λ_c^+ decay modes from data at $\sqrt{s} = 4.6$ GeV, are shown in Fig. A.1. A mass window with the range $(-3\sigma, 3\sigma)$ is applied for each intermediate state, where σ is the resolution of the mass spectrum.

A.1.2 Background Analysis

506 pb^{-1} inclusive MC samples generated at $\sqrt{s} = 4.6$ GeV are used to estimate the remaining background channels. It is found that the main background is from events with hadronic final states. Fig. A.2 shows the distribution of M_{bc} for these background channels. No enhancement around Λ_c^+ signal region is observed.

A.2 Cross Section Measurement

After event selection, signal is extracted by fitting the M_{bc} in data for each mode, where the signal is described by a Monte Carlo shape convoluted with Gaussian function. The background is described with a third-order or second-order polynomial. At $\sqrt{s} = 4.6$ GeV, the parameters of the polynomial are float, and for the other c.m. energy points, the parameters of the polynomial are fixed with the values obtained from fitting the M_{bc} at $\sqrt{s} = 4.6$ GeV. Figure A.3 shows the fit result of each mode by tagging

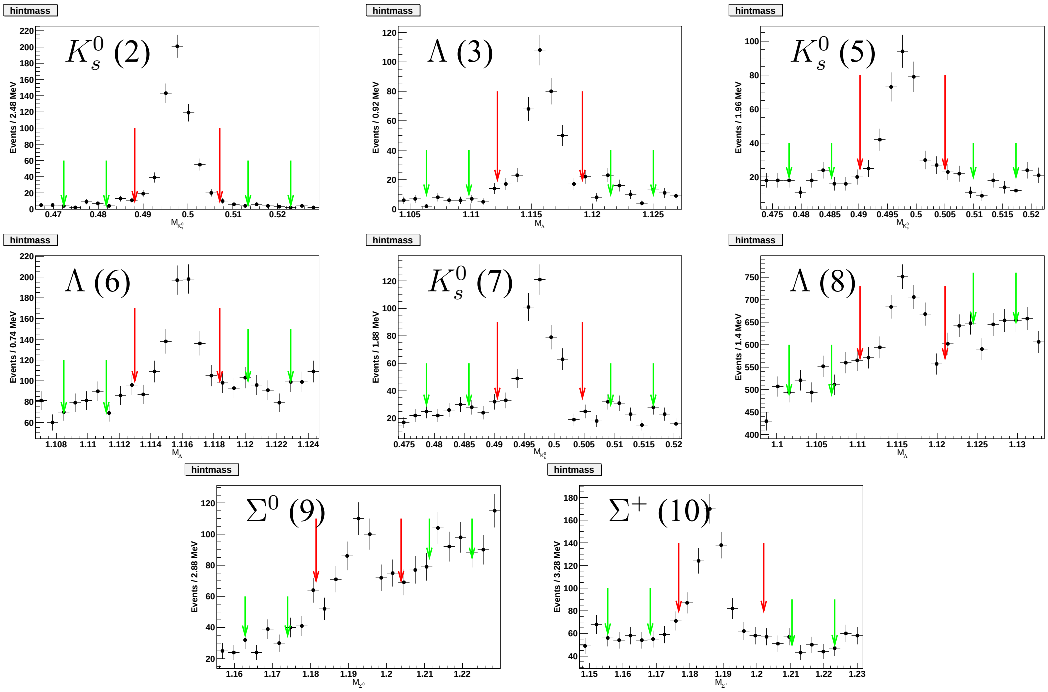

Figure A.1 The invariant mass distribution of intermediated states. The number after each intermediate state indicates the mode.

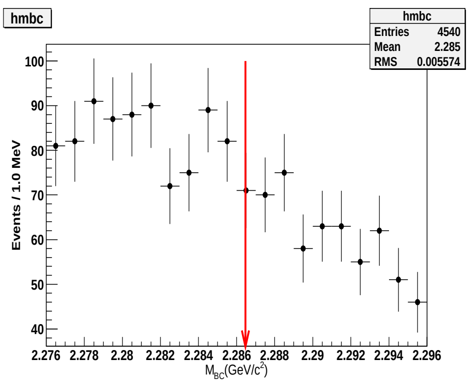

Figure A.2 The distribution of M_{bc} from inclusive background at $\sqrt{s} = 4.6$ GeV.

Λ_c^+ at $\sqrt{s}$=4.60 GeV. The fitting results by tagging Λ_c^+ at other c.m.s energy points are shown in Fig. A.4 A.5 A.6.

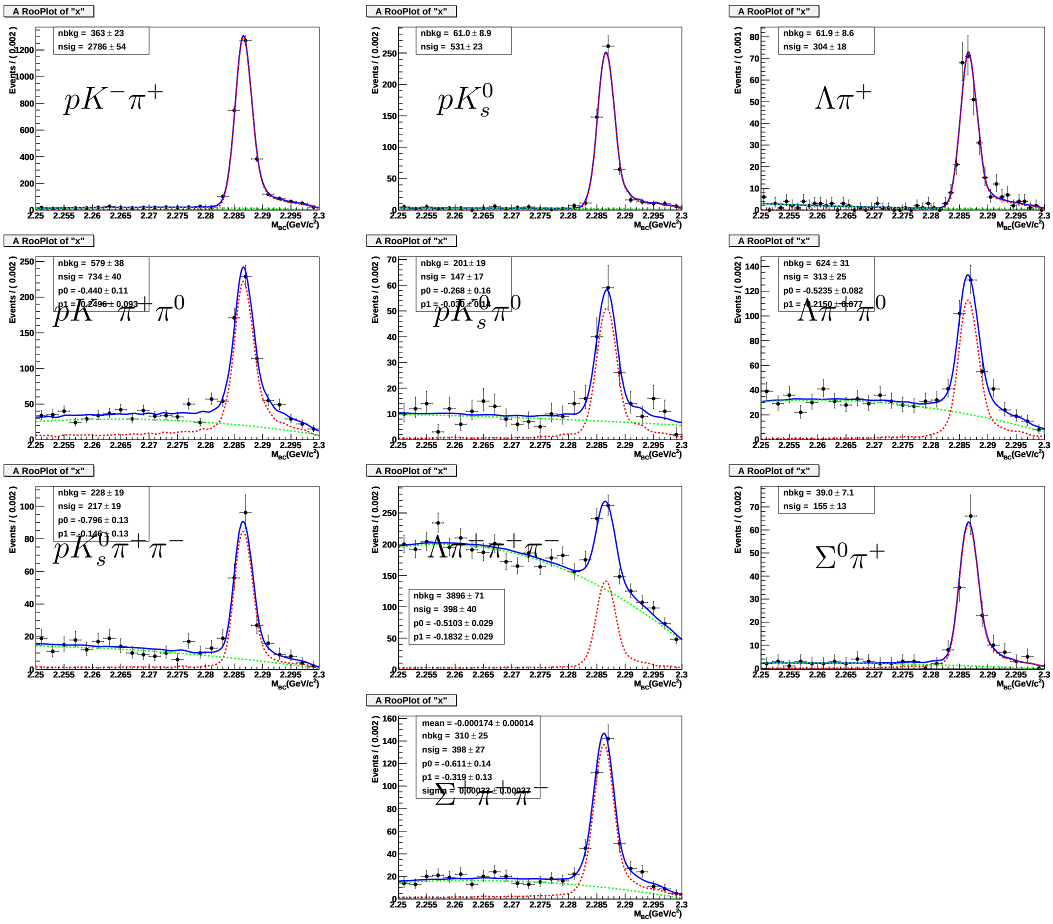

Figure A.3 The fit result of each mode by tagging Λ_c^+ at $\sqrt{s}$=4.60 GeV.

The Born cross section is calculated according to the formula

$$\sigma^i_{Born} = \frac{N_i \pm \Delta N_i}{L \cdot \varepsilon_i \cdot f_{VP} \cdot f_{ISR} \cdot BR_i} \tag{A.1}$$

where the superscript i denotes the $i-$th mode, and N_i is the number of signal events of mode i; The ε_i is the selection efficiency of mode i, which is obtained from the Monte Carlo sample; The $f_{VP} = 1.06$ is the vacuum polarization correction factor [**?**]. The BR_i is the absolute branching fraction of mode i. The factor f_{ISR} is ISR correction factor which is defined as $\sigma^{obs}/\sigma^{Born}$. The cross sections of $e^+e^- \to \Lambda_c^+\overline{\Lambda}_c^{-1}$ calculated

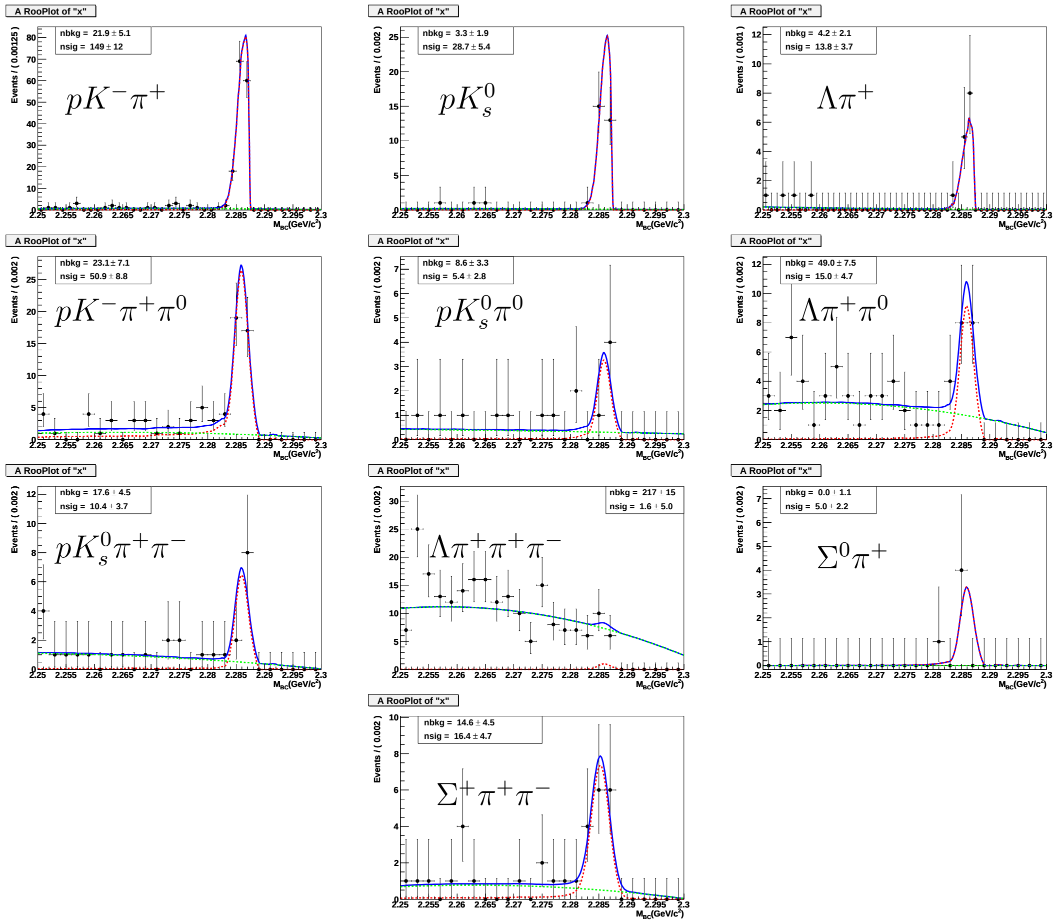

Figure A.4 The fit result of each mode by tagging Λ_c^+ at $\sqrt{s}$=4.575 GeV.

with tagging these multiple decay modes at 4.60 GeV are shown in the Table A.3, where the uncertainty is statistical only.

A.3 Systematic Uncertainty

The source of systematic uncertainty includes the uncertainties from tracking, PID, reconstruction of intermediate states, δ_E requirement, mass window for intermediate states, fitting method of M_{bc}, background shape, and luminosity.

The tracking and PID uncertainty for pion, kaon are assigned to be 1% per track, while for the proton and anti-proton, the systematic uncertainty for tracking and PID is

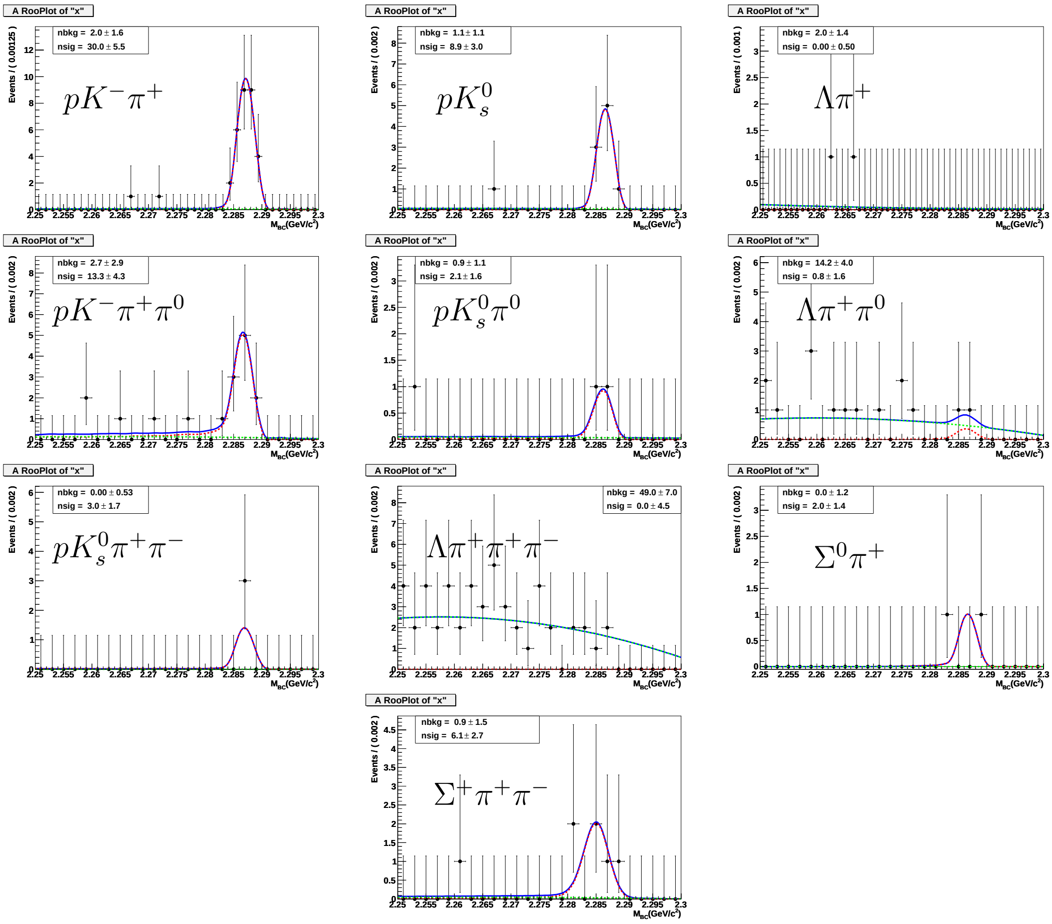

Figure A.5 The fit result of each mode by tagging Λ_c^+ at $\sqrt{s}$=4.58 GeV.

Table A.3 The calculated cross section for each mode by tagging Λ_c^+ at $\sqrt{s} = 4.6$ GeV.

Mode	$N_{\Lambda_c^+}^{data}$	$\varepsilon_{\Lambda_c^+}$ (%)	BR(%)	$\sigma_{\Lambda_c^+}^{Born}$ (pb)
$pK^-\pi^+$	2786.9 ± 54.4	47.6	6.84 ± 0.24	194.1 ± 3.8
pK_s^0	531.0 ± 23.4	48.0	1.11 ± 0.11	226.1 ± 10.0
$\Lambda\pi^+$	304.1 ± 17.8	34.2	0.87 ± 0.10	231.7 ± 13.5
$pK^-\pi^+\pi^0$	733.9 ± 40.0	15.7	4.53 ± 0.84	233.5 ± 12.7
$pK_s^0\pi^0$	146.8 ± 17.0	11.9	1.54 ± 0.23	180.8 ± 21.0
$\Lambda\pi^+\pi^0$	313.0 ± 25.0	5.6	3.15 ± 0.79	401.4 ± 32.0
$pK_s^0\pi^+\pi^-$	217.5 ± 18.8	18.4	1.21 ± 0.16	221.4 ± 19.1
$\Lambda\pi^+\pi^+\pi^-$	398.0 ± 40.1	11.6	2.27 ± 0.18	341.4 ± 34.4
$\Sigma^0\pi^+$	155.0 ± 12.9	17.9	0.87 ± 0.18	225.5 ± 18.8
$\Sigma^+\pi^+\pi^-$	397.8 ± 26.5	15.4	2.41 ± 0.31	243.4 ± 16.2

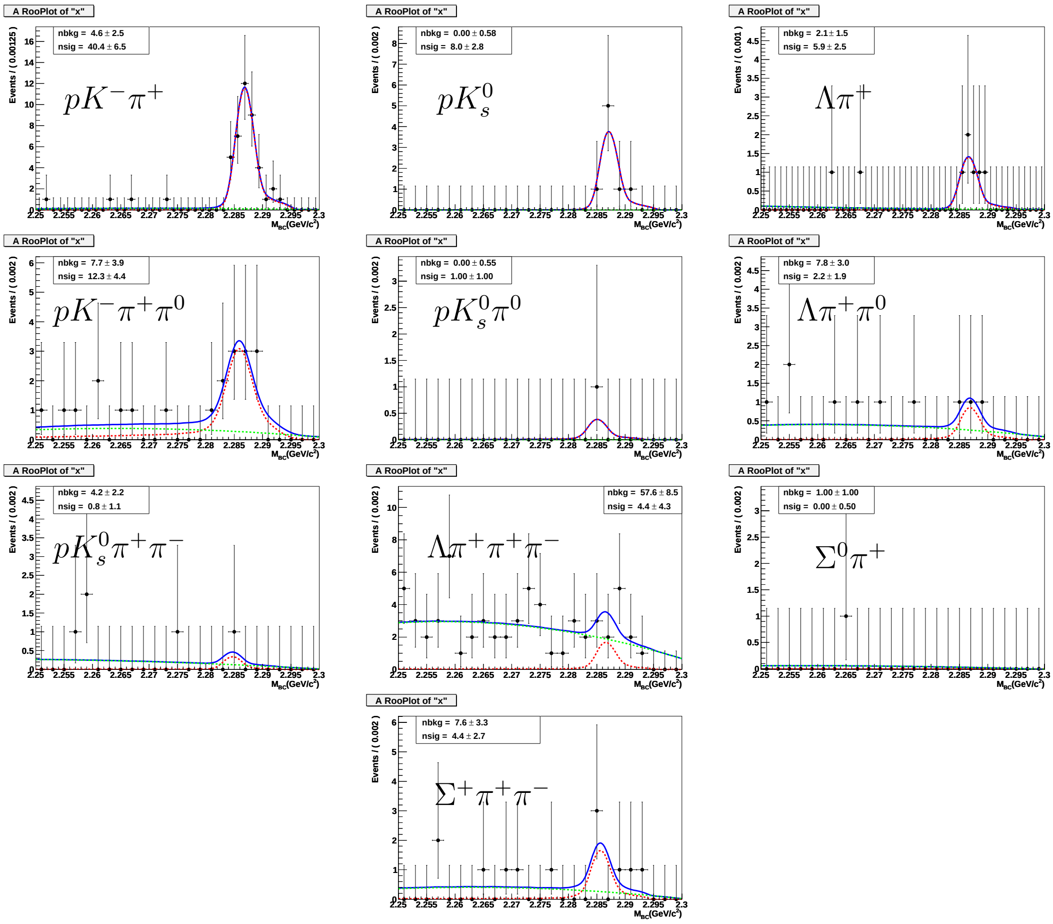

Figure A.6 The fit result of each mode by tagging Λ_c^+ at $\sqrt{s}$=4.590 GeV.

2% per track. We take 3.5% and 2.5% as the systematic uncertainties of reconstruction of the intermediate states K_S^0 and Λ, respectively, for the sake of conservative. The uncertainty for reconstructing the π^0 is 2.0%.

The uncertainty of δ_E is estimated by varying the requirement on δ_E. The uncertainty of the mass window of the intermediate states is estimated by varying the absolute value of mass window from 3σ, 4σ, and 5σ. The largest difference to the nominal results is taken as the uncertainty.

The uncertainty of the fit of M_{bc} is studied from two aspects, one is by changing the fit range of M_{bc} from (2.25, 2.3) to (2.27, 2.3) GeV, and the second is by changing the order of polynomial which is used for describing the background shape.

The uncertainty of luminosity is 1.0%, which is measured by analyzing large-angle Bhabha scattering process. Table A.4 shows the summary of the uncertainties for tagging Λ_c^+ at each decay mode at $\sqrt{s} = 4.6$ GeV. The combined result for Born cross section $e^+e^- \to \Lambda_c^+\overline{\Lambda}_c^-$ by the weighted least square method. The result are summarized in Table A.5.

Table A.4 The systematic uncertainty for each decay mode of Λ_c^+ at $\sqrt{s} = 4.6$ GeV (%).

Mode	TrK	PID	K_S^0	Λ	π^0	δ_E	mass win.	fit range	bkg. shape	Lum.	Total
1. $pK^-\pi^+$	4	4	–	–	–	0.1	–	0.6	0.3	1	5.8
2. pK_s^0	2	2	3.5	–	–	0.8	1.1	0.9	0.2	1	4.9
3. $\Lambda\pi^+$	1	1	–	2.5	–	1.1	1.7	0.2	1.0	1	3.8
4. $pK^-\pi^+\pi^0$	4	4	–	–	2	0.5	–	3.1	3.2	1	7.6
5. $pK_s^0\pi^0$	2	2	3.5	–	2	4.0	3.5	3.2	4.8	1	9.3
6. $\Lambda\pi^+\pi^+\pi^-$	1	1	–	2.5	2	2.7	0.8	3.2	5.1	1	7.6
7. $pK_s^0\pi^+\pi^-$	4	4	3.5	–	–	1.6	2.9	1.7	3.2	1	8.4
8. $\Lambda\pi^+\pi^+\pi^-$	3	3	–	2.5	–	2.9	5.7	0.6	6.8	1	10.6
9. $\Sigma^0\pi^+$	1	1	–	2.5	–	4.3	0.2	1.0	1.3	1	5.5
10.$\Sigma^+\pi^+\pi^-$	4	4	–	–	2	1.8	1.4	0.1	1.3	1	6.6

Table A.5 The weighted average of the Born cross section of each energy point.

$\sqrt{s}$(GeV)	f_{ISR}	$\sigma^{Born}_{\Lambda_c^+}$ (pb)	$\sigma^{Born}_{\overline{\Lambda}_c^-}$ (pb)	$\overline{\sigma^{Born}}$ (pb)
4.575	0.40	$218 \pm 15 \pm 13$	$211 \pm 15 \pm 13$	$214 \pm 10 \pm 13$
4.58	0.64	$184 \pm 26 \pm 12$	$215 \pm 27 \pm 13$	$198 \pm 19 \pm 12$
4.59	0.69	$201 \pm 26 \pm 12$	$193 \pm 25 \pm 12$	$197 \pm 18 \pm 12$
4.60	0.73	$205 \pm 3 \pm 12$	$214 \pm 3 \pm 12$	$207 \pm 3 \pm 12$

A.4 Discussion of the Results

A.4.1 Extraction of $|G_E/G_M|$ Ratio

The angular distribution is measured at $\sqrt{s} = 4.575$ GeV and $\sqrt{s} = 4.6$ GeV. The angular distribution of Λ_c^+ and $\overline{\Lambda}^-$ is obtained by fitting M_{bc} in different $\cos\theta_{\Lambda_c^+}$ and $\cos\theta_{\overline{\Lambda}^-}$ bins, respectively. The angular distribution is shown in Fig. A.7 and we fit them with the function $1 + \alpha\cos^2\theta$. The $|G_E/G_M|$ ratio can be extracted according to the formula:

$$|G_E/G_M|^2 = (1-\alpha)/(\frac{4m^2_{\Lambda_c^+}}{s}\alpha + \frac{4m^2_{Lambda_c^+}}{s}) \tag{A.2}$$

The fit parameters and calculated $|G_E/G_M|$ ratio are summarized in Table A.6.

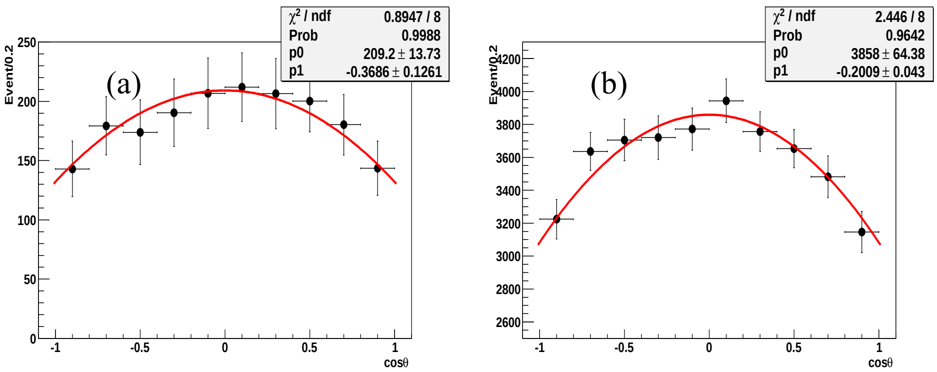

Figure A.7 The fitting on angular distribution. (a) At $\sqrt{s}$=4.575 GeV; (b) At $\sqrt{s}$=4.60 GeV.

Table A.6 The fit parameter of the angular distribution and the calculated $|G_E/G_M|$ ratio at $\sqrt{s} = 4.575,\ 4.6$ GeV.

$\sqrt{s}$ (GeV)	α	$\lvert G_E/G_M \rvert$
4.575	-0.369 ± 0.126	1.473 ± 0.215
4.6	-0.201 ± 0.043	1.226 ± 0.055

A.4.2 Fit the Born Cross Section Line-shape

The Born cross section line-shape is fitted with the non-resonance contribution function which can be parameterized as:

$$\sigma_{f\bar{f}}(q) = \frac{4\pi\alpha^2 C\beta}{3q^2} \cdot |G_M(q)|^2 \cdot [1 + \frac{1}{2\tau}|\frac{G_E(q)}{G_M(q)}|^2] \tag{A.3}$$

where α is QED coupling constant, and $\beta = \sqrt{1 - 4m^2_{\Lambda_c^+}/q^2}$, $\tau = q^2/4m^2_{\Lambda_c^+}$. The Coulomb factor C is defined as $C = \varepsilon \times R$, where $\varepsilon = \pi\alpha/\beta$ is the enhancement factor, and the R is the resummation factor which used to be parameterized as $1/(1 - e^{-\pi\alpha/\beta})$. In this analysis, the fitting on the line-shape can also be performed with the assumption

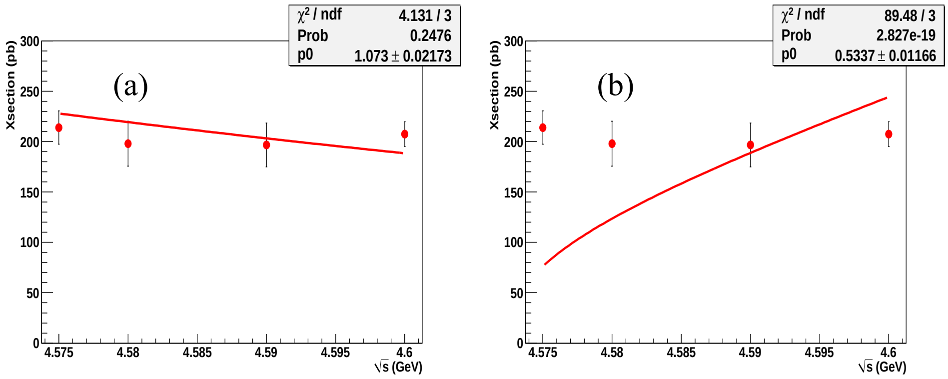

Figure A.8 The fit result of the line-shape from $\sqrt{s}$=4.575 GeV to $\sqrt{s}$=4.60 GeV, (a) with the updated Coulomb correction factor; (b) with the traditional Coulomb correction factor.

that the gluon exchange exists, i.e., the strong interaction between this two charged outgoing baryon works. In this case the resummation factor R is turned to be $R_s = \sqrt{1-\beta^2}/(1-e^{-\pi\alpha_s/\beta})$, where $\alpha_s \simeq 0.5$ is the typical coupling constant of strong interaction.

Assuming $|G_E|$ is an unknown constant near the production threshold of Λ_c^+. We can fit the cross section line-shape under the two assumption: *i)* the updated Coulomb correction factor $C = \varepsilon \times R_s$ and *ii)* the traditional Coulomb correction factor $C = \varepsilon \times R$. The fitting results are shown in Fig. A.8. The goodness of the fit with updated Coulomb correction factor is better than that with traditional one. The yield magnetic form factor $|G_M|$ is 1.073 ± 0.022 for the updated Coulomb correction factor and 0.534 ± 0.012 for the traditional Coulomb factor.

A.5 Conclusion

The cross sections of $e^+e^- \to \Lambda_c^+\overline{\Lambda}_c^-$ at the certer-of-mass energies of 4.575, 4.58, 4.59 and 4.60 GeV with the highest precision by reconstructing Λ_c^+ and $\overline{\Lambda}_c^-$, respectively. The results are listed in Table A.7, where the first uncertainty is statistical, and the second one is systematic, the third is the uncertainty associated with absolute branch fraction. Fig. A.9 shows the comparison of the cross section between this analysis and previous results. The $|G_E/G_M|$ ratio at 4.575 and 4.60 GeV is measured by fitting the angular distribution of Λ_c^+ and $\overline{\Lambda}_c^-$, to be 1.473 ± 0.215 at 4.575 GeV and 1.226 ± 0.055 at 4.60 GeV, where the uncertainties are statistical only.

Table A.7 The weighted average of the Born cross section of each energy point.

$\sqrt{s}$(GeV)	f_{ISR}	$\overline{\sigma^{Born}}$ (pb)
4.575	0.40	$214 \pm 10 \pm 10 \pm 8$
4.58	0.64	$198 \pm 19 \pm 10 \pm 7$
4.59	0.69	$197 \pm 18 \pm 10 \pm 7$
4.60	0.73	$207 \pm 3 \pm 10 \pm 7$

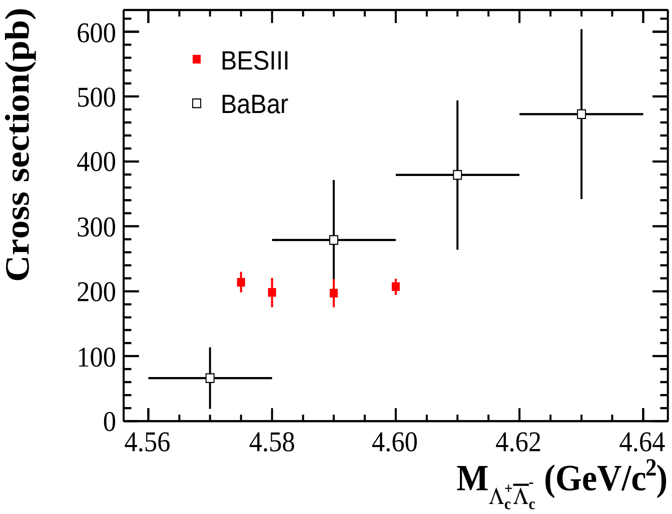

Figure A.9 The comparison of the cross section between this analysis and previous results

Bibliography

[1] A. Zupanc *et al.* (Belle Collaboration), Measurement of the Branching Fraction $\mathcal{B}(\Lambda_c^+ \to pK^-\pi^+)$. Phys. Rev. Lett. **113**, no. 4, 042002 (2014).

Appendix B

Preliminary Study of $e^{+}e^{-} \rightarrow n\bar{n}$

The proton (uud) and the neutron (udd) are the two lightest baryons. Measurement of the nucleon FFs will help explain the spatial differences due to their isospin difference. The electromagnetic FFs of the neutron in time-like region can be measured from $e^{+}e^{-} \rightarrow n\bar{n}$. Up to now, there are two experiments have measured the neutron FFs, *i)* from $n\bar{n}$ threshold up to q^2=6 GeV^2 with FENICE at Adone $e^{+}e^{-}$ collider [1], *ii)* from threshold to q^2=4 GeV^2 with SND detector at VEPP-2000 $e^{+}e^{-}$ collider [2]. The results of $e^{+}e^{-} \rightarrow n\bar{n}$ cross section is close to $e^{+}e^{-} \rightarrow p\bar{p}$, but the uncertainty of $e^{+}e^{-} \rightarrow n\bar{n}$ cross section is over 20%. At BESIII, a large data sample is collecting from $\sqrt{s}$=2.0 to 3.1 GeV. With the large data sets, we can measure $e^{+}e^{-} \rightarrow n\bar{n}$ in a wide c.m.energies with improved precisions. In this chapter, we provide a preparation study of $e^{+}e^{-} \rightarrow n\bar{n}$ with current data sets of $\sqrt{s}$=2.2324 and 2.40 GeV, where the luminosity are 2.63 pb^{-1} and 3.42 pb^{-1}, respectively. The signal process of $e^{+}e^{-} \rightarrow n\bar{n}$ is generated in PHSP.

B.1 Preliminary Event Selection

Neutral showers are required to have a minimum energy deposition of 25 MeV in the barrel ($|\cos\theta|$ <0.8) of the EMC and 50 MeV in the end caps (0.86< $|\cos\theta|$ <0.92) of the EMC. In one event, at least two showers are required. The most energetic shower is assigned as $\bar{n}$ candidate. The shower with position most opposite to that of the $\bar{n}$ candidate is assigned as n candidate.

To further distinguish signal process from beam-associated background and digamma process, Following criteria on $\bar{n}$ candidates are applied:

- the deposited energy of $\bar{n}$, E_{nbar}, should be larger than 500 MeV.
- total number of hits in EMC of $\bar{n}$ in its 40 degree cone, Hit_40d_{nbar}, should be larger than 40.
- the second Moment of $\bar{n}$ ($\Sigma_i^n E_i r_i^2 / \Sigma_i^n E_i$) should be larger than 20.

The comparisons of E_{nbar}, Hit_40d_{nbar}, second Moment and the lateral Moment, (defined as $\Sigma_{i=3}^n E_i r_i^2 / (E_1 r_0^2 + E_2 r_0^2 + \Sigma_{i=3}^n E_i r_i^2)$) between signal MC and background sources are shown in Fig. B.1, where the physical background processes are normalized according to the integral luminosity, the background from separated beam conditions is normalized according to the data taken time, and signal MC is randomly normalized.

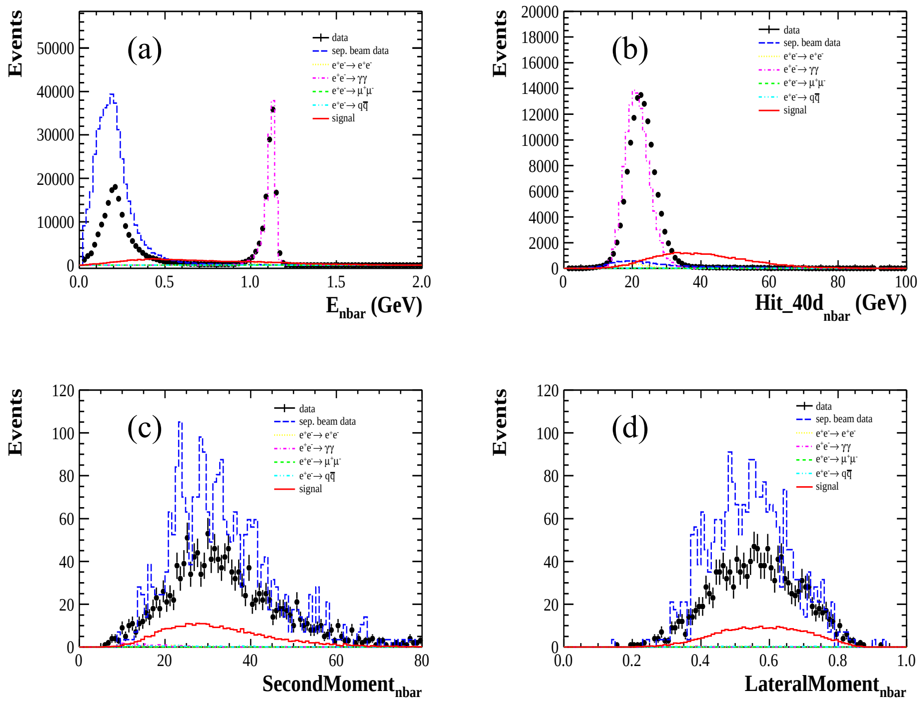

Figure B.1 Comparison of several distributions for $\bar{n}$ candidates.

After the selection on $\bar{n}$ candidates, the process of beam-associated background and digamma process are highly suppressed. However, the signal to noise ratio is still low due to the large background. Following criteria on n candidates are applied:

- the deposited energy of n, E_n, should be larger than 60 MeV and less than 500 MeV.
- the polar angle of n should require $|\cos\theta_n| < 0.8$.

The comparisons of E_n and $\cos\theta_n$ between signal MC and background sources are shown in Fig. B.1.

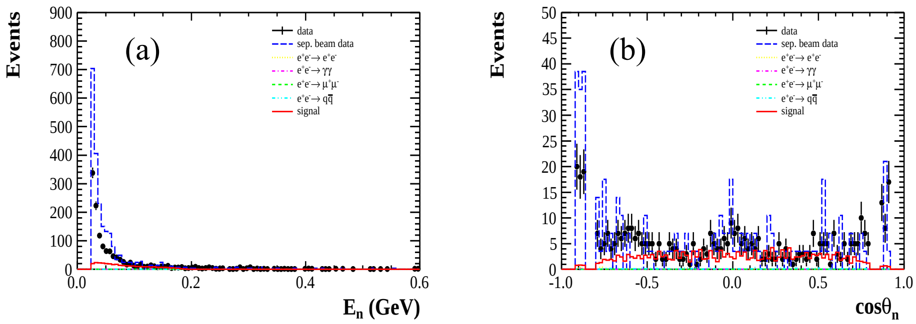

Figure B.2 Comparison of several distributions for n candidates.

In event selection level, the extra deposited energy, E_{extra}, defined as $E_{tot} - E_{nbar} - E_n$, where E_{tot} is the total deposited energy of good showers, should be less than 20 MeV. The number of charged tracks, N_{track}, should be equals to 0. Fig. B.3 shows the comparison of E_{extra} and N_{track} between signal MC and backgrounds.

After the selection, we listed the cut flow for each selection criteria for data, signal MC and background channels, as listed in Table B.1 and Table B.2 for data at $\sqrt{s}$ = 2.2324 GeV and 2.40 GeV, respectively. The scale factor is calculated by $\sigma \times Lumi./N_{total}$ for physics process and $T_{exp.}/T_{sep.}$. For the separated beam condition backgrounds, due to the short data taking time, the scale factor is larger than 1.

The angle distribution between n and $\bar{n}$ after selection is pictured in Fig. B.4, where the main background is beam-associated background. However, because the scale factor

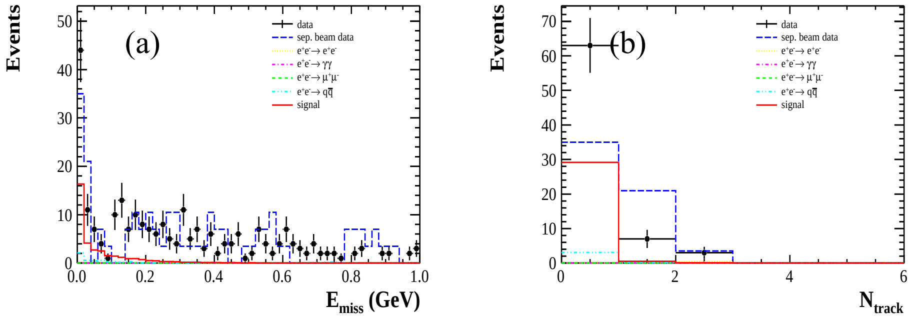

Figure B.3 Comparison of several distributions in event level.

Table B.1 Cut flow between data, MC and background at 2.2324 GeV.

Channel	Bhabha	Dimu	Digamma	$q\bar{q}$	Sep. beams	Exp. data	Signal MC
Tot. num.	9.6×10^6	7.0×10^5	1.9×10^6	2.0×10^6	2.3×10^7	5.7×10^7	2.0×10^5
N_{charge}=0	9.5×10^5	6115	1.8×10^6	1.2×10^5	2.2×10^7	5.2×10^7	2.0×10^5
$N_{shower} \geq 2$	1.7×10^4	358	1.3×10^6	1.0×10^5	1.0×10^7	2.9×10^7	1.5×10^5
$E_{nbar} > 0.5$ GeV	7732	10	1.2×10^6	1.7×10^4	4049	1.5×10^5	4.0×10^4
Secmom>20	1134	1	8.9×10^4	2296	2747	1.7×10^4	3.2×10^4
Hits_40d$_{nbar}$ >40	7	0	50	332	844	1448	1.6×10^4
$0.06 < E_n < 0.5$ GeV	2	0	1	240	193	448	1.0×10^4
$\lvert\cos\theta_n\rvert < 0.8$	2	0	1	240	145	353	9865
$E_{miss} < 0.02$ GeV	1	0	0	72	22	74	5959
E_{track}=0	0	0	0	67	10	64	5831
Scale factor	1/2.5	1/15.3	1/10.3	1/21.7	3.5		
N_{norm}	0	0	0	3.1	35		

Table B.2 Cut flow between data, MC and background at 2.40 GeV.

Channel	Bhabha	Dimu	Digamma	$q\bar{q}$	Sep. beams	Exp. data	Signal MC
Tot. num.	9.0×10^5	9.4×10^5	9.2×10^5	8.4×10^4	2.3×10^7	7.5×10^7	1.9×10^5
N_{charge}=0	8.9×10^4	8260	8.8×10^5	4.6×10^4	2.2×10^7	7.0×10^7	1.8×10^5
$N_{shower} \geq 2$	1590	513	6.5×10^5	3.9×10^4	1.0×10^7	3.8×10^7	1.4×10^5
$E_{nbar} > 0.5$ GeV	692	22	5.9×10^5	6641	4049	1.5×10^5	4.2×10^4
Secmom>20	110	5	4.2×10^4	927	2747	1.9×10^4	3.3×10^4
Hits_40d$_{nbar}$ >40	1	0	21	149	844	1819	1.8×10^4
$0.06 < E_n < 0.5$ GeV	0	0	1	118	193	553	1.3×10^4
$\lvert\cos\theta_n\rvert < 0.8$	0	0	1	110	145	451	1.3×10^4
$E_{miss} < 0.02$ GeV	0	0	0	34	22	81	7636
E_{track}=0	0	0	0	34	10	66	7488
Scale factor	4.7	1/18.3	1/4.4	1/8.1	4.4		
N_{norm}	0	0	0	4.2	44		

of this background source is larger than 1, the shape of the background is discrete and cannot describe data very well.

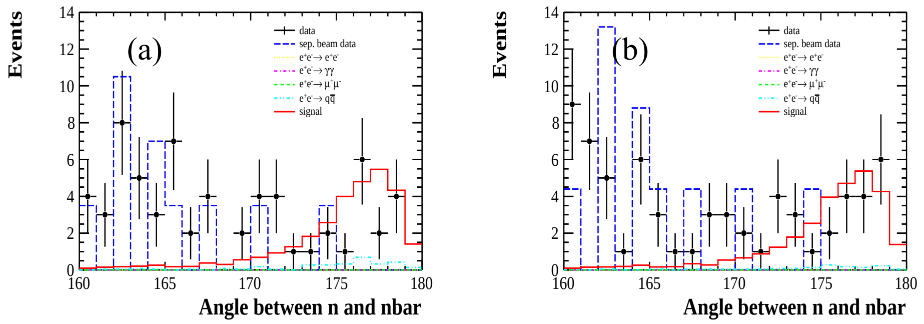

Figure B.4 Angle between n and $\bar{n}$ after selection for (a) 2.2324 GeV and (b) 2.40 GeV.

B.2 Discussion

The select efficiency from MC simulation is 2.9% and 4.1% for 2.2324 GeV and 2.40 GeV, respectively, which are relatively low. Since the only information we can use is the EMC information. The time-of-flight information for neutral shown is not reconstructed. However, in the process $e^+e^- \to n\bar{n}$, the neutron is monoenergetic, and its flight time will be peaked at a certain value. If we can use the information of time-of-flight, then fit the peak, the $n\bar{n}$ signal will be extracted with high efficiency. Here is some rough estimation, assuming the momentum of neutron is 600 MeV. The TOF detector, made of plastic scintillator BC408, is consist with hydrogen atom and carbon atom. The probability of the $\bar{n}$ interact with proton in hydrogen and carbon can be calculated by

$$P_{\bar{n}} = \sigma_{p\bar{n}} \times (\rho_H + 6\rho_c) \times L, \tag{B.1}$$

where $\sigma_{p\bar{n}}$ is te cross section of $p\bar{n}$, taken from PDG, to be 1.5×10^2 mb. ρ_H and ρ_c is the number of hydrogen and carbon atoms per cm^3, to be 5.23×10^{22} and 4.74×10^{22}, respectively. L is the length of two TOF layers, to be 10 cm. The calculated probability of $P_{\bar{n}}$ is 50.5%. Similarly, the interaction probability of n with proton is 13.5% by using the same equation and taking σ_{pn} to be 0.4×10^2 mb.

Bibliography

[1] A. Antonelli, R. Baldini, P. Benasi, M. Bertain, M. E. Biagini, V. Bidoli, C. Bini and T. Bressani *et al.*, The first measurement of the neutron electromagnetic form-factors in the timelike region. Nucl. Phys. B **517**, 3 (1998).

[2] M. N, Achasov, A. Y. Barnyakov, K. I. Beloborodov, A. V. Berdyugin, D. E. Berkaev, A. G. Bogdanchikov, A. A. Botov and T. V. Dimova *et al.*, Study of the process $e^+e^- \to n\bar{n}$ at the VEPP-2000 e^+e^- collider with the SND detector. Phys. Rev. D **90**, no. 11, 112007 (2014).

致　谢

时间如白驹过隙，这已经是我在科大的第九个年头，四年的本科生活，五年的研究生涯，使我从懵懂的少年逐渐成熟，美好的青春记忆都留在科大。

值此论文完成之际，首先要感谢我在科研路上的领路人，我的导师赵政国院士，赵老师知识渊博，目光长远，有丰富的人生经验，教会我很多治学的经验和做人的道理，他为我们创造了极好的科研环境和出国交流学习的机会。赵老师百忙之中坚持每周和我们聚餐，了解和关心我们近期的学习和生活，并向我们传递他的人生智慧，这是我非常珍惜的时刻。

感谢我的副导师黄光顺教授，黄老师治学严谨，平易近人，为我的论文提供了明确的课题和并指导我的论文工作。在我的工作和生活中都提供了很大的帮助。感谢鄢文标副教授，他是带领我接触高能物理的启蒙老师，我的第一份工作即在鄢老师的指导下完成。感谢彭海平教授，彭老师工作认真，思维敏捷，我常常能在和他的讨论中找到解决难题的办法，收获良多。

感谢高能所的沈肖艳，苑长征，平荣刚，朱凯等老师对我在北京生活的帮助，和在学术上的讨论及建议。感谢意大利 INFN 的 Rinaldo Baldini Ferroli 教授对我工作的关心和提供的宝贵建议，Rinaldo 幽默风趣，学术经验丰富，我非常庆幸有这样的良师益友。感谢 Wolfgang Gradl，Frank Mass 等帮助我修改论文。

感谢董娟老师，李雯老师对我生活上的帮助。感谢实验室的众多师兄师姐及师弟师妹们，严亮，刘明辉，王雅迪，李翠，耿聪，孙振田，姬长胜，许志蕊，吴硕星，赵宇翔，李冰，徐来林，王志宏，方馨，王驰，闫文成，高榛，张亚腾，潘越，夏磊，高鑫磊，曾哲，薛明萱，李佩莲，刘栋，王维平等，感谢他们对我工作的指导帮助和各种激烈的问题讨论，也感谢他们创造的融洽的实验室氛围，和组织的有益身心的活动。

感谢我亲爱的男朋友陈健，在这几年里，他的支持和鼓励是我前进的最大

慰藉。感谢我的姐姐和可爱的小外甥女。感谢我的爷爷，他一直希望我们能多读书，不断学习。最后，我把我的论文献给我最爱的父母，我深知你们的辛苦和不易，感谢你们多年来对我的支持和付出！

周小蓉

May 6, 2015

在读期间发表的学术论文与取得的研究成果

Publications in Journals：

1. M. Ablikim *et al.* (BESIII Collaboration), Observation of $J/\psi \to p\bar{p}a_0(980)$. Phys. Rev. D 90, 052009 (2014).

2. M. Ablikim *et al.* (BESIII Collaboration), Study of χ_{cJ} decaying into $\phi K^*(982)\bar{K}$. arXiv:1503.04699 [hep-ex], Submitted to PRD.

3. Xiaorong Zhou, Measurement of the proton form factor by studying $e^+e^- \to p\bar{p}$ at BESIII. arXiv:1504.02680 [hep-ex], Submitted to PRD.

Under review in BESIII Collaboration：

1. Xiaorong Zhou, Liang Yan, Cross section measurement of $e^+e^- \to \Lambda\overline{\Lambda}$ with BESIII at 2.2324, 2.40, 2.80 and 3.08 GeV. Internal review close to finish. Draft inpreparation.

2. Xin Fang, Liang Yan, Xiaorong Zhou, Cross section measurement of $e^+e^- \to \pi^+\pi^-\psi(3686)$ at BESIII and the observation of charged charmoniumlike states in $e^+e^- \to \pi^+\pi^-\psi(3686)$ at $\sqrt{s} = 4.26$ GeV and $\sqrt{s} = 4.42$ GeV. Under internal review.

3. Weiping Wang, Weiming Song, Xiaorong Zhou, Cross section measurement of $e^+e^- \to \Lambda_c^+\overline{\Lambda}_c^-$ near threshold at BESIII. Under internal review.

International Activities:

1. 2011/10/07-21 Third France-Asia Particle Physics School (FAPPS11), Les Houches, France.

2. 2013/10/07-12/07 Academic communication, in Istituto Nazionale Di Fisica Nucleare (INFN), Italy.

3. 2014/06/22-27 The 8th Joint Meeting of Chinese Physicists (OCPA8), Singapore. And gave two poster ”Observation of $J/\psi \to p\bar{p}a_0(980)$” and ”Measurement of the proton form factor by studying $e^+e^- \to p\bar{p}$ at BESIII”

4. 2015/05/25-28 The 10th International Workshop on the Physics of Excited Nucleons (NSTAR 2015), Japan. will give a talk ”Proton pair production cross sections at BESIII”